NEUTRON INTERACTIONS ON ^{136}Xe AND THEIR IMPACT ON NEUTRINOLESS DOUBLE BETA DECAY SEARCHES

Sean J. Daugherty

Submitted to the faculty of the University Graduate School

in partial fulfillment of the requirements for the degree

Doctor of Philosophy

in the Department of Physics,

Indiana University

June 2018

Accepted by the Graduate Faculty, Indiana University, in partial fulfillment of the requirements for the degree of Doctor of Philosophy.

Doctoral Committee

Mike Snow, Ph.D. (Chair)

Lisa Kaufman, Ph.D.

Mike Berger, Ph.D.

April 18, 2018

Rex Tayloe, Ph.D.

Acknowledgements

First, I would like to thank my parents, whose unending support made this work possible. Thank you to my family and friends who have helped all along the way.

I would like to thank the many colleagues that I have collaborated with during my time as a graduate student. The EXO-200 collaboration is a very welcoming and helpful group of people. In particular, I would like to thank Steve Herrin, Michelle Dolinski, Timothy Daniels, Caio Licciardi, Liang Yang, Brian Mong, Jon Davis, and Cindy Lin for their help with work on-site at WIPP and analysis-related work.

I would also like to thank my colleagues from my work with data from the DANCE and GEANIE detectors. This work would not have been possible without the input from John Ullmann, Aaron Couture, Matt Devlin, Nik Fotiades, and Milan Krtika.

Thank you to my dissertation committee, Mike Snow, Rex Tayloe, Mike Berger, and Lisa Kaufman, for their comments and help on this work.

Thank you to my research advisor, Lisa Kaufman, and the whole IU EXO research group, Josh Albert, Tessa Johnson, Thomasina O'Conner, and Jacob Zettlemoyer. Despite some bumps in analysis progress, Josh's enduring enthusiasm for understanding new physics helped push this work to completion. Thanks to Tessa for being a great friend and colleague. Finally, thanks to Lisa Kaufman for the many opportunities she provided to me to grow as a person and as a scientist throughout our work together.

Sean Daugherty

NEUTRON INTERACTIONS ON ^{136}Xe AND THEIR IMPACT ON NEUTRINOLESS DOUBLE BETA DECAY SEARCHES

The search for neutrinoless double beta decay ($0\nu\beta\beta$), a rare process which may reveal the Dirac/Majorana nature of the neutrino, requires a careful understanding of all backgrounds. A precise study of neutron interactions on ^{136}Xe, a common isotope in double beta decay experiments, is necessary for the background models in experiments such as EXO-200 and, in the future, nEXO. Neutron capture and neutron inelastic scattering on ^{136}Xe have been studied at the Detector for Advanced Capture Experiments (DANCE) and the GErmanium Array for Neutron Induced Excitations (GEANIE) at the Los Alamos Neutron Science Center. The relative neutron cross sections for neutron capture at thermal and first resonance energies have been measured. The gamma cascades for these captures have also been measured, and cascade models have been developed. Partial gamma ray cross sections of (n,xnγ) are being measured with data from GEANIE. These data will also be used to set limits on the number of events in the $0\nu\beta\beta$ ROI for ^{136}Xe. These studies will lead to improved sensitivity to neutrinoless double beta decay in the future.

Mike Snow, Ph.D. (Chair)

Lisa Kaufman, Ph.D.

Mike Berger, Ph.D.

Rex Tayloe, Ph.D.

Contents

Curriculum Vitae

List of Tables

List of Figures

Chapter 1

Double beta decay and backgrounds

Double beta decay is a second-order Standard Model process where two neutrons simultaneously decay inside a nucleus. When this process occurs with the emission of two neutrinos, it is called two neutrino double beta decay ($2\nu\beta\beta$). However, it is theoretically possible that this process can occur without the emission of neutrinos, which is known as neutrinoless double beta decay ($0\nu\beta\beta$).

$2\nu\beta\beta$ has been directly measured in ten nuclei, with very long half-lives from 7×10^{18} yr to 2×10^{21} yr depending on the isotope [1]. It is possible to measure $2\nu\beta\beta$ in these nuclei because single beta decay is energetically forbidden.

The theoretical process, $0\nu\beta\beta$, is interesting because its existence would help to elucidate properties of neutrinos. Measuring this process would show that neutrinos are Majorana particles, whether the mass hierarchy is normal or inverted, and inform the absolute mass scale of neutrinos.

Several experiments are making great strides in the race to set limits on and potentially measure $0\nu\beta\beta$. The most notable current and next generation experiments searching for this process are EXO-200 (Enriched Xenon Observatory) [2], nEXO (next EXO), KamLAND-Zen [3], GERDA (GERmanium Detector Array) [4], MAJORANA [5], and CUORE (Cryogenic Underground Detector for Rare Events) [6]. These measurements are using ^{136}Xe (EXO-200, nEXO, and KamLAND-Zen), ^{76}Ge (GERDA and MAJORANA), and ^{130}Te (CUORE) as their source of decaying nuclei.

This work will focus on EXO-200 and nEXO and its source of $0\nu\beta\beta$ decay events, ^{136}Xe, as well as measurements of neutron capture and neutron inelastic scattering on ^{136}Xe.

1.1 History of neutrino measurements

1.1.1 Discovery of neutrinos

Beta decay is the decay of a neutron into a proton, electron, and electron antineutrino,

$$n \rightarrow p + e^{-} + \overline{\nu}_e. \tag{1.1}$$

Measured electrons from beta decay show a continuous spectrum of energies due to the three-body nature of the kinematics, see Fig. 1.1. However, without the idea of the neutrino, this process seemed to violate long-held conservation laws of energy, momentum, and angular momentum.

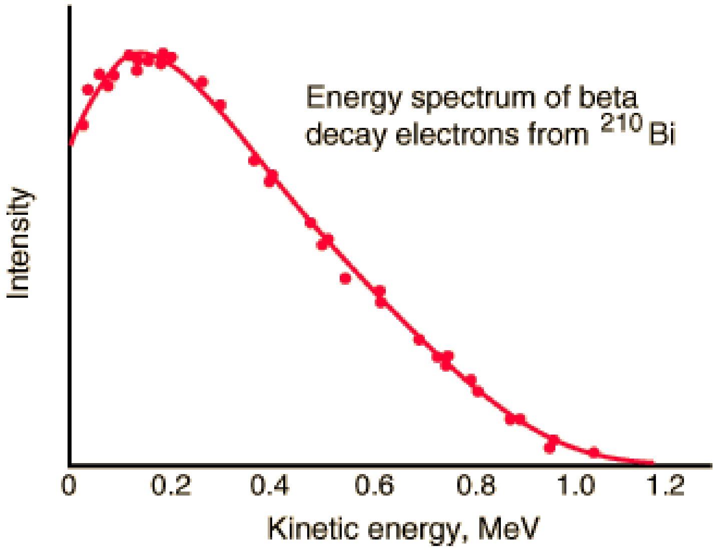

Figure 1.1: Experimental energy spectrum of beta decay from ^{210}Bi with data originally from [7].

As an answer to this mystery, the neutrino was proposed by Wolfgaing Pauli in 1930 as a carrier of the missing energy and momentum. Cowan and Reines observed the electron antineutrino in 1956 [8] with antineutrinos produced from a nuclear reactor. The reactor produced a very large flux of antineutrinos, which then interacted with protons in tanks of water with the inverse beta decay process,

$$\overline{\nu}_e + p \rightarrow n + e^+. \tag{1.2}$$

A coincidence of γ-rays from the positron annihilation and γ-rays from neutron capture showed that this interaction was in fact inverse beta decay, with a cross section of 6.3×10^{-44} cm^2.

1.2 Dirac or Majorana nature of neutrinos

Some properties of the neutrino have remained elusive to particle physicists for many years. One of these properties that is still unknown about neutrinos is whether they are Dirac or Majorana fermions. A fermion that is distinct from its anti-particle is a Dirac fermion, and its relativistic dynamics are determined by the Dirac equation:

$$(i\gamma^\mu \partial_\mu - m)\psi = 0 \tag{1.3}$$

In 1937, Majorana postulated a modification to this equation that allowed massive neutral fermions to be their own antiparticles [9]:

$$i\gamma^\mu \partial_\mu \psi - m\psi^c = 0 \tag{1.4}$$

Observation of $0\nu\beta\beta$ would violate lepton number conservation and prove that neutrinos are Majorana fermions.

1.3 Neutrino masses

In the Standard Model, neutrinos are masseless particles. However, measurements have shown that there are three distinct neutrino masses. These mass states do not correspond directly to the flavors of the neutrinos, but rather a mixing of all three flavors. The relative difference between two sets of these mass states is known, but the overall scale of these masses has yet to be determined, as shown in Fig. 1.2. The mass states are a mixture of the three neutrino flavors, electron, muon, and tau.

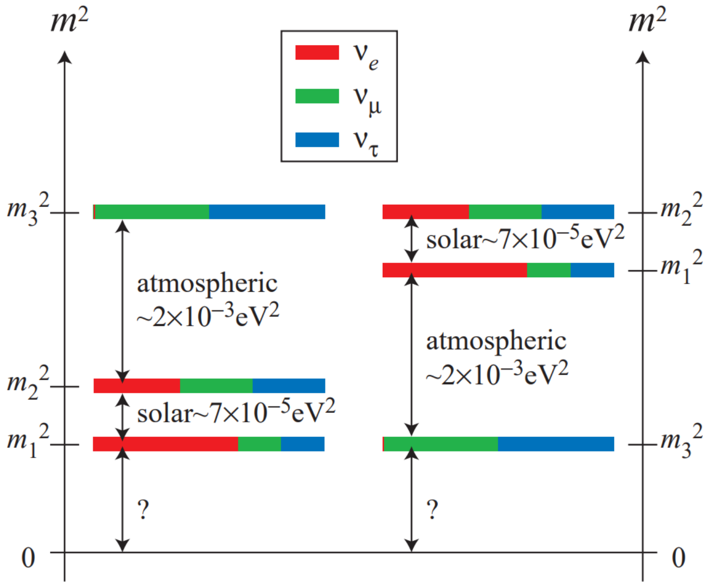

Figure 1.2: Diagram showing the two possible neutrino mass hierarchies. On the left is the normal hierarchy, with the mass states increasing in mass from m_1^2 to m_3^2. On the right is the inverted hierarchy, with the mass state m_3^2 below both m_1^2 and m_2^2. This figure is from [10].

1.4 Two Neutrino Double Beta Decay

Two neutrino double beta decay is a rare transition that can only occur in even-even nuclei, producing an emission of two electrons and two antineutrinos. This process follows the form:

$$(Z, A) \rightarrow (Z + 2, A) + e_1^- + e_2^- + \overline{\nu}_e^1 + \overline{\nu}_e^2, \tag{1.5}$$

where Z is the atomic number and A is the number of nucleons, and a diagram of the process is shown in Fig. 1.3.

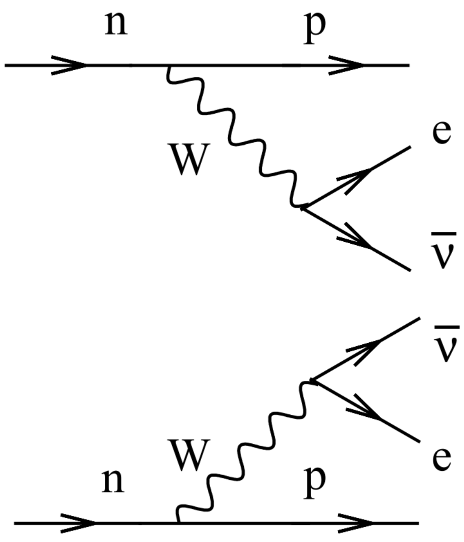

Figure 1.3: Standard model $2\nu\beta\beta$. This is the simulataneous decay of two neutrons into two protons, two electrons, and two electron antineutrinos. Figure from [11]

Some nuclei are stable against ordinary beta decay, but not stable against $2\nu\beta\beta$. This happens only in nuclei with an even number of protons and an even number of neutrons because spin-coupling stabilizes these nuclei. When single β decay is forbidden or heavily suppressed, double beta decay is possible to measure. Fig. 1.4 shows that single β decay from ^{136}Xe to ^{136}Cs is energetically forbidden, but $\beta\beta$ decay is possible to ^{136}Ba.

1.5 Neutrinoless Double Beta Decay

Observation of neutrinoless double-beta decay ($0\nu\beta\beta$),

$$(Z, A) \rightarrow (Z + 2, A) + e_1^- + e_2^- \tag{1.6}$$

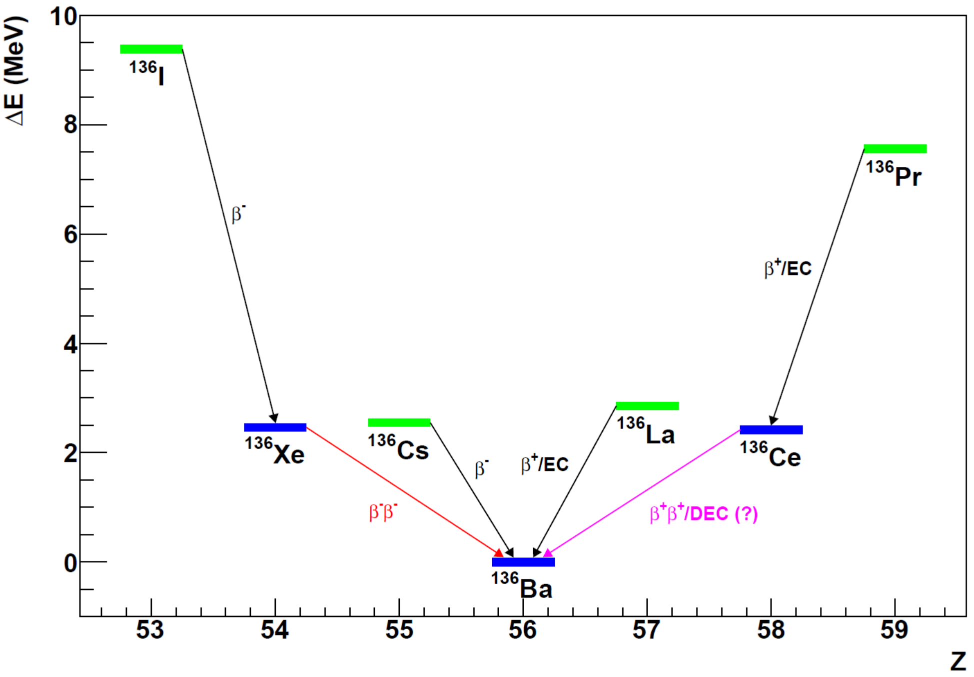

Figure 1.4: Ground state nucleus energies near ^{136}Xe for A = 136. The energy difference shown is relative to the binding energy of ^{136}Ba.

a hypothetical lepton-number-violating decay mode, would provide evidence for the Majorana nature of neutrinos, shown in Fig. 1.5. Current limits on the half lives for the $0\nu\beta\beta$ mode of ^{136}Xe and ^{76}Ge decay are $T^{0\nu}_{1/2} > 10^{25}$ year [12, 13].

This process can be measured by looking at the endpoint energy, Q, of the $2\nu\beta\beta$ spectrum. $0\nu\beta\beta$ would show up as a peak at the endpoint, with the size of the peak being proportional to the half-life of $0\nu\beta\beta$. Fig. 1.6 shows an illustration of these spectra for two different normalizations of the $0\nu\beta\beta$ signal.

1.6 Neutrinoless Double Beta Decay Backgrounds

In general, neutrinoless double beta decay experiments are looking for a very small signal hidden behind a myriad of possible backgrounds. This section will discuss many common backgrounds in double beta decay experiments.

There are two primary sources of background events: radionuclides and cosmic rays.

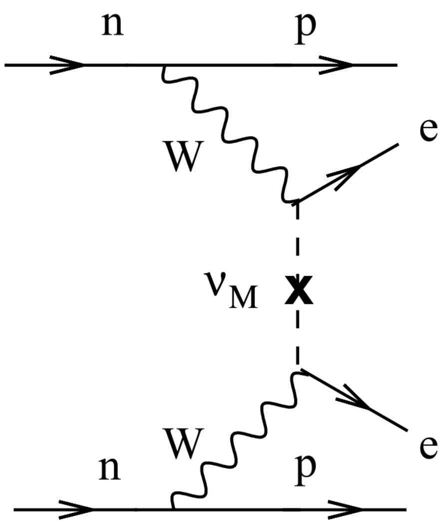

Figure 1.5: This is the theoretical diagram for $0\nu\beta\beta$, the simulataneous decay of two neutrons into two protons and two electrons. Figure from [11].

Radionuclides primarly produce problematic γ-rays that penetrate into the detector, potentially mimicking the $0\nu\beta\beta$ signal. Cosmic rays can produce fast neutrons, which in turn can cause hadronic showers, neutron capture, and neutron inelastic scattering in and around the detector.

1.6.1 Backgrounds Due to Gamma Rays

In EXO-200, every material was carefully selected in order to screen out active radionuclides. This material screening is a necessary step in producing a low-background environment for the EXO-200 detector to measure potential $0\nu\beta\beta$ candidates [15]. Despite this careful material selection, there are still backgrounds due to radioactive nuclides present in the detector materials. For EXO-200, these radionuclides are primarily ^{238}U, ^{232}Th, and ^{40}K, which produce a range of gamma backgrounds. ^{238}U and ^{232}Th both follow a long decay chain. In particular, radon from both ^{238}U and ^{232}Th decay chains is a significant background for EXO-200.

Along with material selection, providing a low-background environment also requires

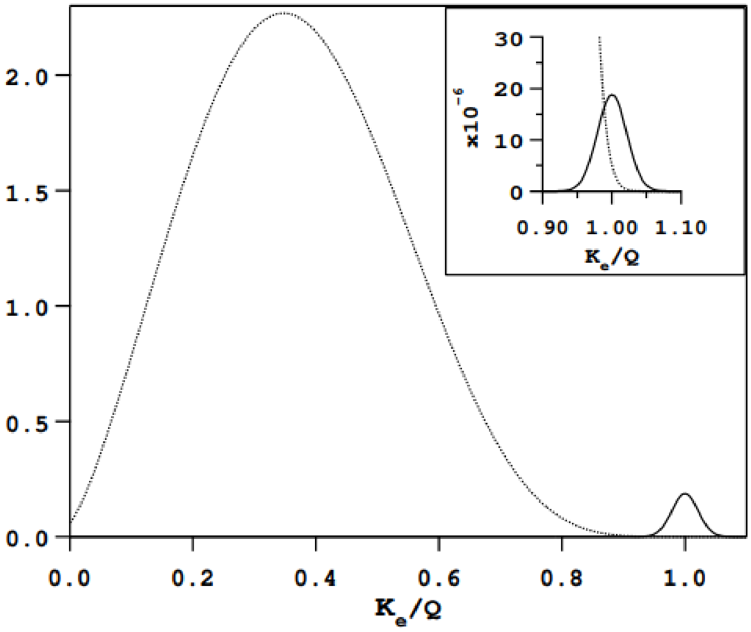

Figure 1.6: Illustration of the $2\nu\beta\beta$ spectrum with $0\nu\beta\beta$ present at the endpoint. K_e is the electron kinetic energy, and Q is the endpoint energy. The $2\nu\beta\beta$ spectra are normalized to 1.0 with a detector resolution of 5%. The primary plot has $0\nu\beta\beta$ normalized to 10^{-2}, and the inset shows $0\nu\beta\beta$ normalized to 10^{-6}. Figure from [14].

significant passive detector shielding in order to reduce γ-ray penetration. For example, EXO-200 uses lead block shielding, cryogenic fluid bath that acts as a shielding material, and fiducial volume of xenon in order to reduce the effects of gamma backgrounds inside the detector.

1.6.2 Backgrounds Due to Cosmic Rays and Neutrons

The other major source of background events are due to cosmic rays, which are dependent on the depth of the experiment. As cosmic rays pass through the earth, they produce ionization energy and hadronic showers from decaying pions. A larger overburden reduces these experimental backgrounds but in most cases are still non-negligible.

Backgrounds due to direct muons can be relatively easily mitigated by active shielding.

Muon panels surrounding the detector can identify muons passing through the detector area and veto the data from those time periods. Muons primarily produce short-lived events, allowing for effective vetoing. However, muons passing close to a detector, but not detected by muon panels, can cause fast neutrons that produce non-vetoed backgrounds.

In EXO-200, the backgrounds produced by cosmogenic-related events are primarily cosmogenic activation due to fast neutrons on copper and xenon. Cosmogenic activation of ^{136}Xe produces ^{137}Xe, causing both a prompt gamma background and a delayed ^{137}Xe β decay. This will be discussed further in Section 2.4.

Cosmogenic backgrounds are important to understand in both the detector materials and the source of $\beta\beta$ itself. Understanding backgrounds due to neutrons scattering from ^{136}Xe requires more work, as previous neutron scattering measurements on xenon have primarily been slow neutron measurements and often not isotope specific.

This work focuses on neutron capture on ^{136}Xe for thermal energies up to 100 keV neutron energy and neutron inelastic scattering from ^{136}Xe for neutron energies from 1 to 100 MeV.

1.7 Nuclear interactions

Neutron interactions are either direct or compound nuclear interactions. A direct nuclear reaction is one where the projectile does not excite any internal degrees of freedom in the nucleus and interacts with only one nucleon. An example of a direct process is elastic neutron scattering, where the neutron does not excite the nucleus into an excited state. A compound nuclear reaction happens when the projectile interacts with many nucleons. Direct nuclear reactions happen on a much shorter time scale, 10^{-22} s, than compound nuclear reactions, 10^{-14} s [16]. The relatively long time scale of a compound nuclear reaction allows the compound nucleus to come to thermodynamic equilibrium.

At lower neutron projectile energies, the neutron may be captured and form a compound nucleus. Following the capture of the neutron, the nucleus emits one or more γ-rays. This can be represented by the notation N(n,γ), where N is the nucleus, n is the incoming neutron, and

γ is the γ emission after the neutron capture. Neutron capture on ^{136}Xe, ^{136}Xe (n,γ)^{137}Xe, is discussed in Chapter 3.

Another example of a compound nucleus reaction is neutron inelastic scattering, denoted by (n,nγ). This reaction proceeds with the re-emission of a neutron, leaving the original nucleus in an excited state. Neutron inelastic scattering on ^{136}Xe, [^{136}Xe (n,nγ)^{136}Xe], is discussed in Chapter 4.

Chapter 2

EXO-200

2.1 The EXO-200 detector

The Enriched Xenon Observatory (EXO) is a program designed to search for neutrinoless double beta decay with the isotope ^{136}Xe. The present phase is a 100-kg scale experiment, called EXO-200, and a next-generation experiment, called nEXO, will be a ton-scale experiment. EXO-200 was the first 100 kg scale double beta decay experiment; it began taking data beginning in May 2011 and is still presently taking data.

The EXO-200 detector is a right cylinder composed of a time projection chamber (TPC) filled with enriched liquid xenon, approximately 40 cm diameter and 44 cm long. The xenon is enriched with the double-beta-decay isotope of choice, ^{136}Xe, such that the isotopic composition is 80.6% ^{136}Xe and 19.1% ^{134}Xe. The xenon acts as both the source and the detector medium of the double beta decays. ^{136}Xe has a Q-value of 2.458 MeV [17]. The area around this Q-value, a window of $2\sigma_E$, where σ_E is EXO-200's energy resolution, is called the region of interest (ROI).

The TPC is housed in a double-walled cryostat filled with HFE-7000[1], a cryogenic fluid, shown in Fig. 2.1. The cryostat is surrounded by lead shielding, which passively reduces background events in the detector. Finally, the clean room in which the detector is installed is surrounded by muon veto panels, which actively reduce backgrounds due to muons. The detector is installed at the Waste Isolation Pilot Plant (WIPP) near Carlsbad, NM, see

---

[1] HFE-7000 is a product by 3M™

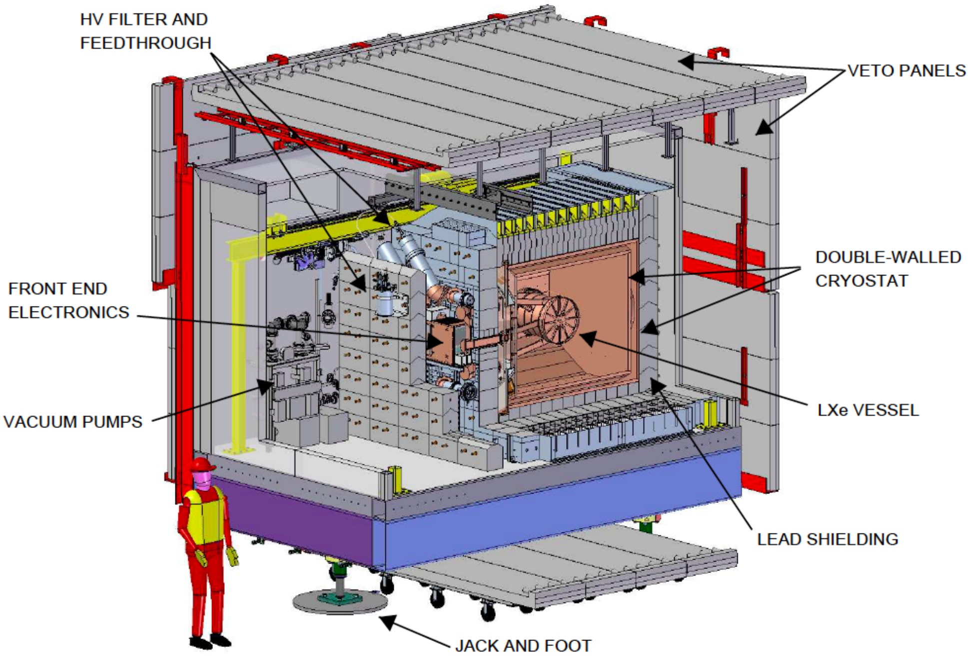

Figure 2.1: Detailed schematic of the infrastructure surrounding the EXO-200 detector. The copper time projection chamber (TPC) is surrounded by a double-walled cryostat and lead shielding. The electronics readouts are just outside of the first layer of lead shielding. Muon veto panels surround the outer areas of the clean room module.

Fig. 2.2.

2.1.1 Time Projection Chamber

EXO-200 uses a TPC to detect charge and scintillation light produced by particle interactions. Each TPC is constructed from two anode grids at 60° with respect to each other and a shared central cathode biased to -8 kV in Phase I. The electric field causes ionization electrons to drift toward the anodes and are collected on the U-wire plane as shown in Fig. 2.3.

The xenon volume in EXO-200 acts as both the source and detection medium. Interactions in the liquid xenon cause ionization, creating both charge and light. Gamma rays from scintillation events are collected on Large Area Avalanche Photo Diodes (LAAPDs) on either end of TPC [18]. These elements allow for measurement of the initial time and

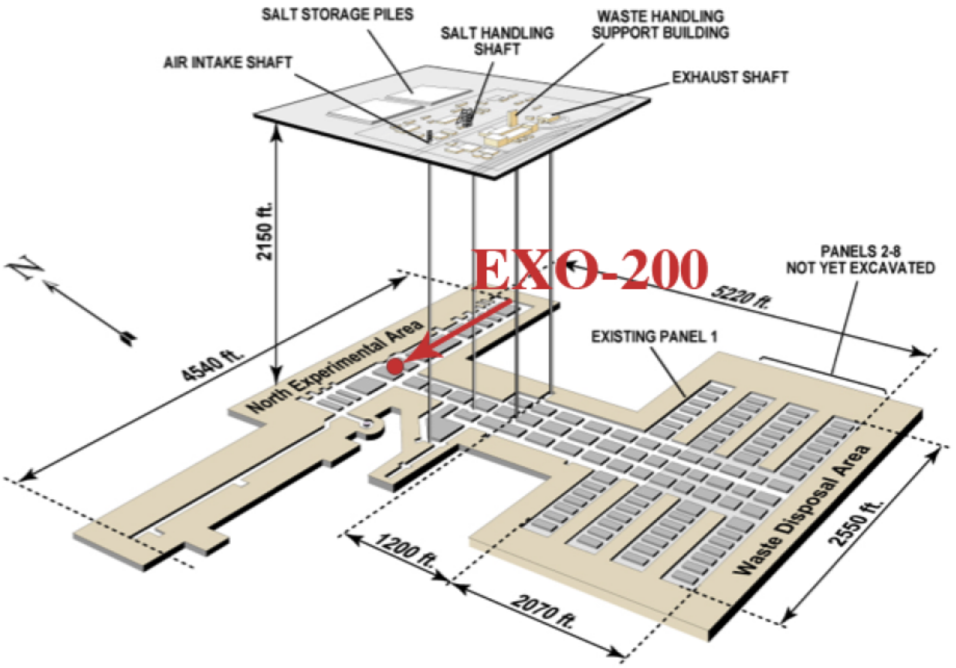

Figure 2.2: A diagram of the Waste Isolation Pilot Plant (WIPP) facility, with EXO-200 installed on the north side of the mine 655 m below the surface.

position of the interaction.

Charge is drifted in an electric field from the central cathode to each anode plane located in front of the APD plane. The time at which the light is collected by the APDs determines the initial time for the event with the drift time of the electrons allowing for the z-position determination. The electrons drift at a constant drift velocity of 1.705 mm/μs [19]. The charge collection at the anode tells us x and y position, and the z position is determined via

$$z = t_d v_d, \tag{2.1}$$

with t_d drift time and v_d drift velocity.

2.1.2 Detector Calibration

EXO-200 events are categorized as single-site (SS) or multi-site (MS) using information about event topology [20]. In general, gammas are more likely to be classified as multi-site

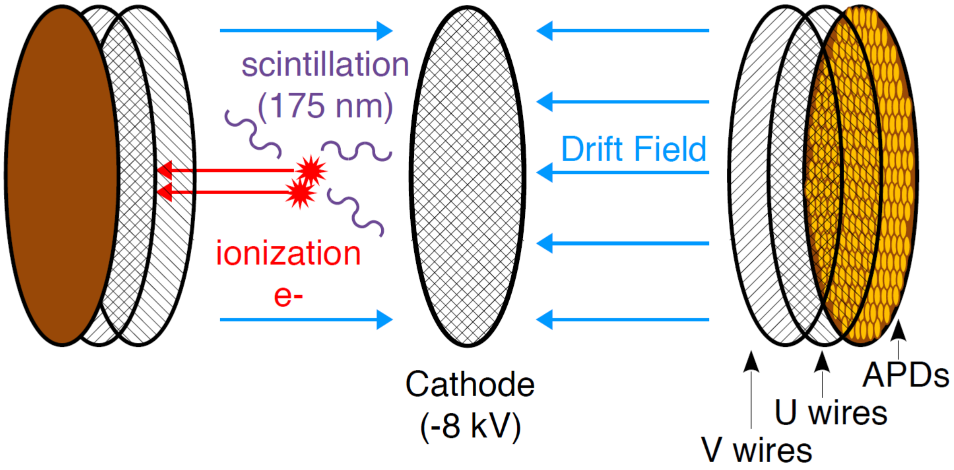

Figure 2.3: Basic design for the EXO-200 TPC. The central cathode splits the xenon volume in half with anodes on either end of the xenon volume. Two layers of wire planes called the U and V wire planes measure x and y position of the charge deposit in the TPC. The APD's on either end collect scintillation light from events in the xenon.

because of Compton scattering in the xenon. Electrons (specifically electrons from double beta decay) are primarily categorized single-site. From source calibration data, the single-site to multi-site ratio is known very well. This categorization of SS vs. MS allows for a significant reduction of background.

The EXO-200 detector is calibrated routinely with several radioactive γ sources. A calibration source tube wraps around the detector so that a source capsule may be placed at designated locations around the TPC, as shown in Fig. 2.4. The sources are mounted on a cable that is pushed along the tube into the desired location, and pulled out afterwards to return to low background data taking.

The calibration data are fit to a full absorption peak for the sources ^{228}Th, ^{60}Co, ^{137}Cs, and ^{226}Ra. Primarily, EXO-200 is calibrated with ^{228}Th because the daughter nucleus ^{208}Tl emits a 2.615 MeV gamma which is near the ^{136}Xe Q-value of 2.458 MeV. Decay gammas from these sources cover an energy range from 600 keV to 2.615 MeV.

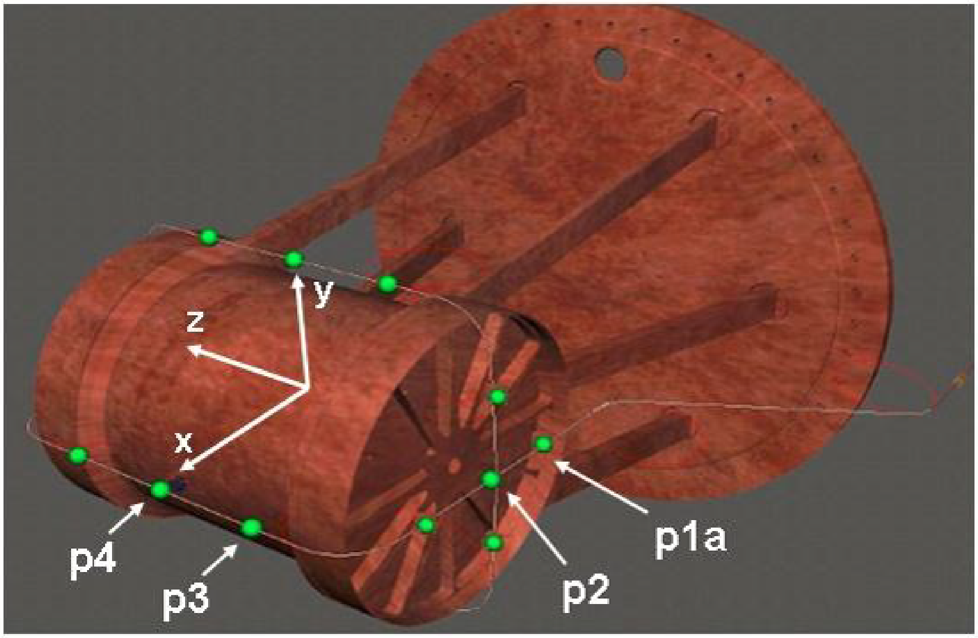

Figure 2.4: A calibration tube surrounds the xenon vessel, allowing for multiple raidoactive source calibration points. The most common calibration point is P4x, allowing for even illumination of both sides of the detector.

2.2 Electron Lifetime Measurement

As electrons drift through the TPC, electrons are captured on electronegative impurities such that the ionization peak energy is lowered. The measured energy from the ionization spectrum appears lower than the true gamma energy because not all of the electrons are collected; therefore, a correction must be applied to account for this effect. The initial population of electrons from an event decay exponentially as a function of drift time and electron lifetime according to

$$N_{e^-}(t) = N_0 \mathrm{exp}(-t/\tau_e), \tag{2.2}$$

where N_{e^-} is the population of electrons after drifting, N_0 is the initial population of electrons before drifting, t is the time that the electrons have drifted, and τ_e is the electron lifetime.

In order to measure the electron lifetime, the TPC is split into 30 bins along the electron drift direction. The energy of the ionization energy peak from a radioactive source is fit at each drift-time bin, with various methods described in the following sections. An exponential fit to the decay of the ionization energy as a function of drift-time bin allows for the extraction of the electron lifetime, τ_e.

As electron lifetime in the system increases, the exponential fit becomes more linear and the uncertainty in the fits increases. The average electron lifetime for low background data is around 3 ms. During periods where the xenon recirculation pump is not running, the electron lifetime drops rapidly as electronegative impurities outgas into the xenon without being removed. Periods with an electron lifetime below 2 ms are cut from the data, often due to its changing rapidly after recovering from a power outage.

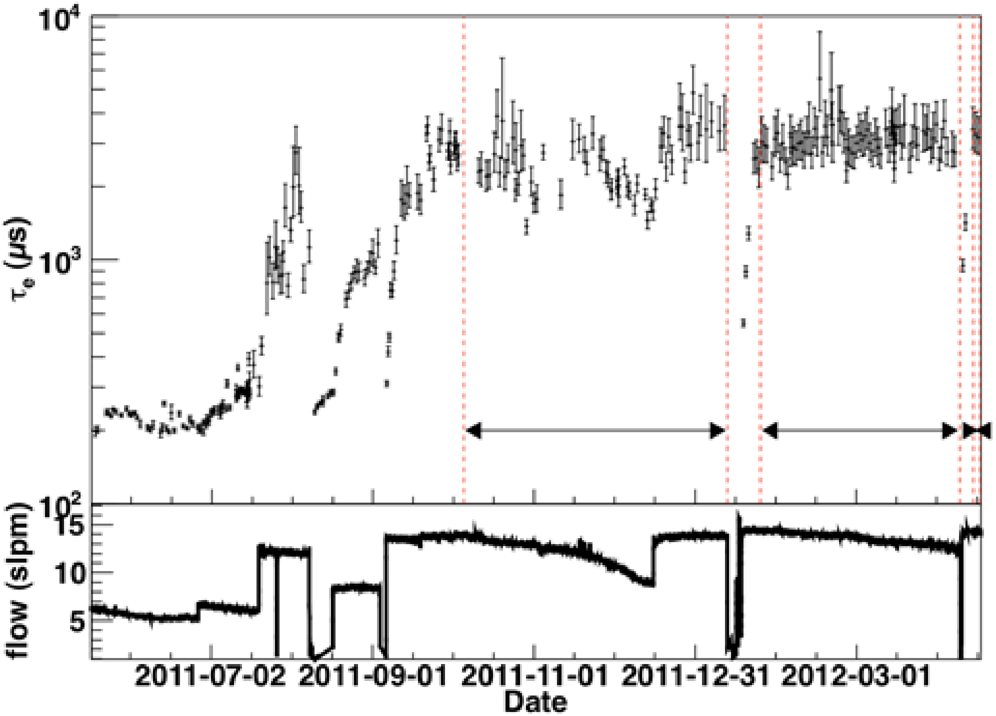

Figure 2.5: Plot of electron lifetime and xenon flow speed versus time. The electron lifetime is strongly, and nonlinearly, dependent on flow rate. As flow rate increases, more of the xenon is purified per unit time. During normal data periods, the flow rate is about 15 standard liters per minute, and the electron lifetime is around 3 ms.

2.2.1 Electron lifetime fitting

Multiple methods have been employed in the fitting of electron lifetime for EXO-200. There are three steps to determining the correction to the data based on the electron lifetime. First, a fit is made for each TPC drift-time bin in each calibration run to determine the photopeak position. Then, the electron lifetime during that run is determined by a fit to the peak position as a function of z, Fig. 2.7. Finally, the electron lifetimes are fit as a function of time to allow for a continuous correction applied to the data as seen in Fig. 2.8.

The electron lifetime determination for each run has been primarily measured in three methods over the course of the experiment. The first and simplest is fitting the ^{208}Tl photopeak with a Gaussian plus an error function for the Compton shelf as seen in Fig. 2.6. The photopeak position in each z-bin is recorded and plotted as a function of z. The other two methods use a Monte-Carlo-based fitting scheme, where MC results are used to fit the whole ionization spectrum for each source, described in detail in Section 2.2.2.

2.2.2 Monte-Carlo-based Fitting Methods

Instead of approximating the energy spectrum from source calibration runs as a Gaussian for the photopeak and an error function for the Compton edge, the data can be modeled with the shape of EXO-200-specific Monte Carlo simulations. Monte Carlo simulations were produced for each source used for radioactive source calibration. This allows for a spectrum shape unique to each source used in the analysis. The Monte-Carlo-based fit was done in two separate methods.

First, the TPC was split into drift-time bins as with the Gaussian-plus-error-function method, but the data within each bin were fit with the shape of the MC results. After the photopeak energy was determined for each drift-time bin, the photopeak energy was plotted as a function of z as with the Gaussian-plus-error-function method. An example of this type of fit is shown in Fig. 2.9.

Second, the two steps from the previous fitting methods were combined. Instead of fitting

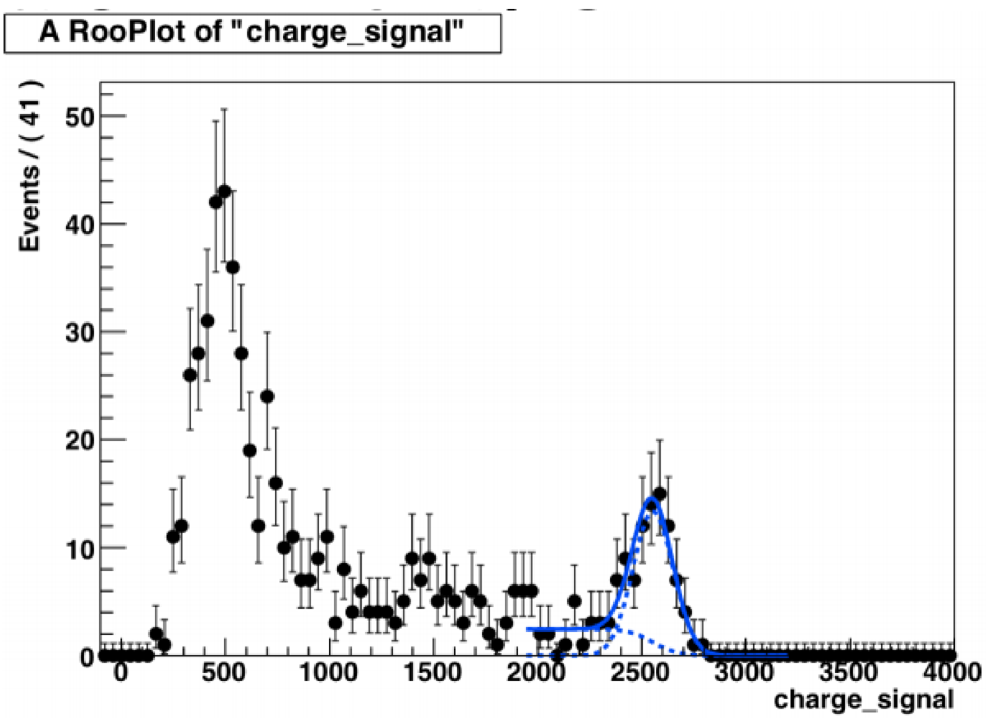

Figure 2.6: Shown is a simple fitting method for the ^{232}Th photopeak. The TPC is split into many z-bins along the direction of electron drift. Data is collected for each z-bin and fit as shown. Shown here is a Gaussian+error function fit to the peak and Compton shelf.

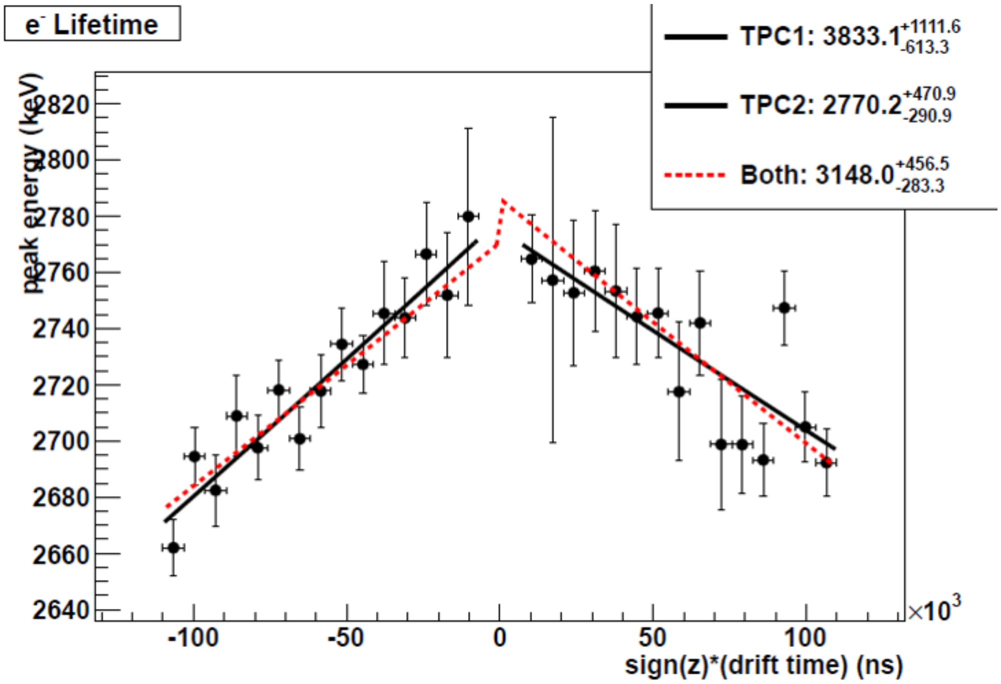

Figure 2.7: A fit to the collected ionization energy as a function of z allows the extraction of the electron lifetime. The low-background data are corrected for the electron lifetime such that events closer to the cathode will have a higher correction applied, due to the longer drift distance.

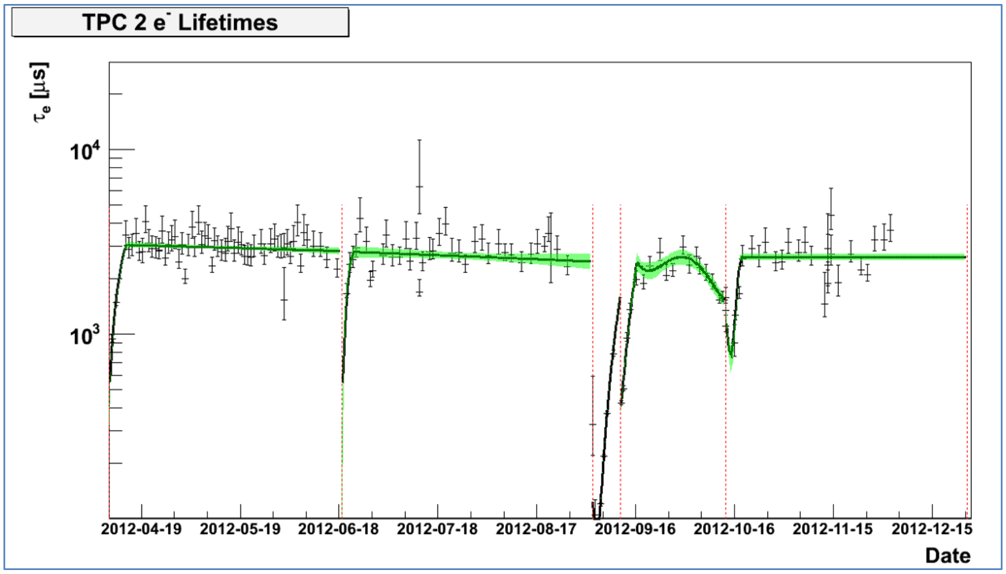

Figure 2.8: Calibration runs are taken routinely, allowing for routine electron lifetime measurements. These electron lifetime measurements are plotted as a function of time and fit with polynomials, allowing for a continuous electron lifetime correction to be applied to the data. In general, quadratic polynomials are fit to the periods from xenon pump outages, with constant or linear polynomials during stable periods.

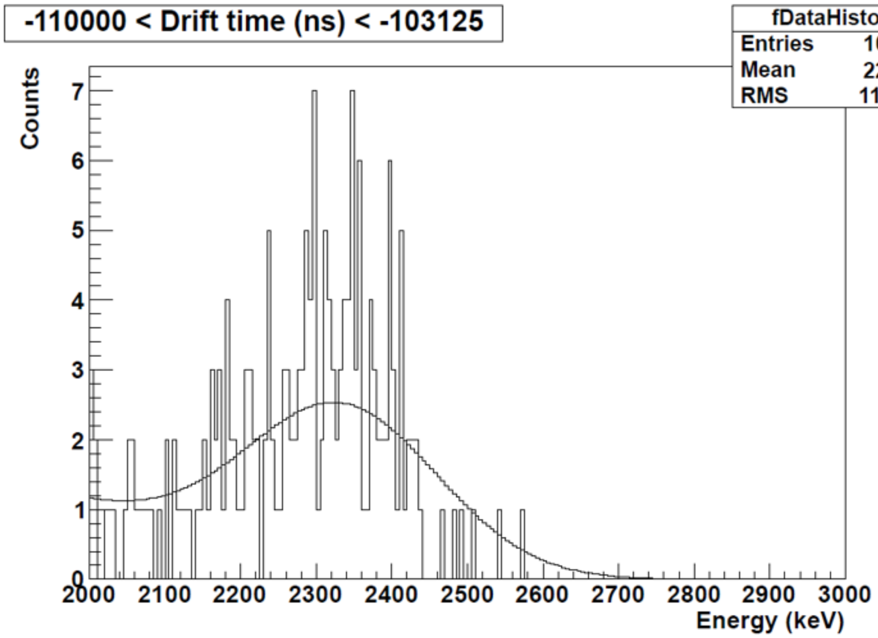

Figure 2.9: Monte-Carlo-based fit to a single drift-time bin (1/30th) of the TPC. Fit returns peak position and uncertainty, which are plotted as a function of z and fitted for electron lifetime.

photopeak energy and z separately, all the data were taken together for a simultaneous fit in both z and photopeak energy. The fitting function takes the form:

$$E_C = p0 + p1 E_{UC} exp(-t/\tau_e), \tag{2.3}$$

where E_C is the corrected charge energy, E_{UC} is the uncorrected or raw charge energy, t is drift time (linearly related to z), and τ_e, the electron lifetime. An example of the result of one of these fits for a relatively low electron lifetime run is shown in Fig. 2.10. τ_e is directly extracted as one of the fit parameters with this method. Fit results can be checked by looking at individual bins in the TPC, as with previous methods as shown in Fig. 2.11.

The MC2D fit is the current fitting method for EXO-200 electron lifetime analysis.

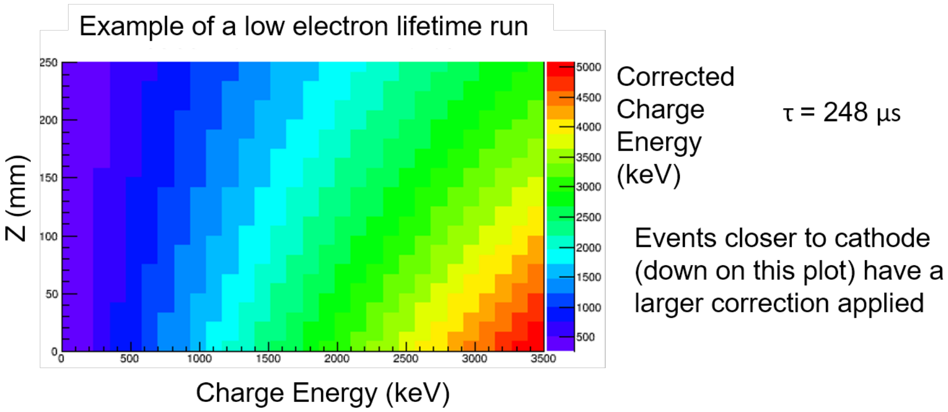

Corrected Charge Energy (keV)

τ = 248 μs

Events closer to cathode (down on this plot) have a larger correction applied

Figure 2.10: Example of the result from the Monte-Carlo-based 2D electron lifetime fit. The result is a calibration function with the electron lifetime as one of the parameters in the fit. This plot shows a low electron lifetime run. Hypothetically, a run with infinite electron lifetime would show straight veritcal lines on this plot.

2.3 Low background results

The final fit for Phase I of EXO-200 data is presented in [12]. Phase I amounted to 477.6 days of data and an exposure of 123.7 kg-yr.

The best fit for $0\nu\beta\beta$ counts, shown in Fig. 2.12, is 9.9 events, which is consistent with zero at 1.2σ. This leads to a lower limit on the $0\nu\beta\beta$ half-life in ^{136}Xe of 1.1×10^{25} yr at a 90% confidence level.

The $2\sigma_E$ ROI region in EXO-200 fit to three dominant backgrounds: 8.1 counts from ^{238}U-chain related events, 16.0 ^{232}Th-chain related events, and 7.0 ^{137}Xe decay events.

2.4 Neutron Backgrounds in EXO-200

There are two significant types of backgrounds to $0\nu\beta\beta$ experiements: long-lived radionuclides and cosmic-ray-related backgrounds. Backgrounds due to radionuclides can be reduced by passive shielding and reduction of radionuclide material near the detector. On the other hand, backgrounds due to cosmic rays can be mitigated via both passive and active shielding,

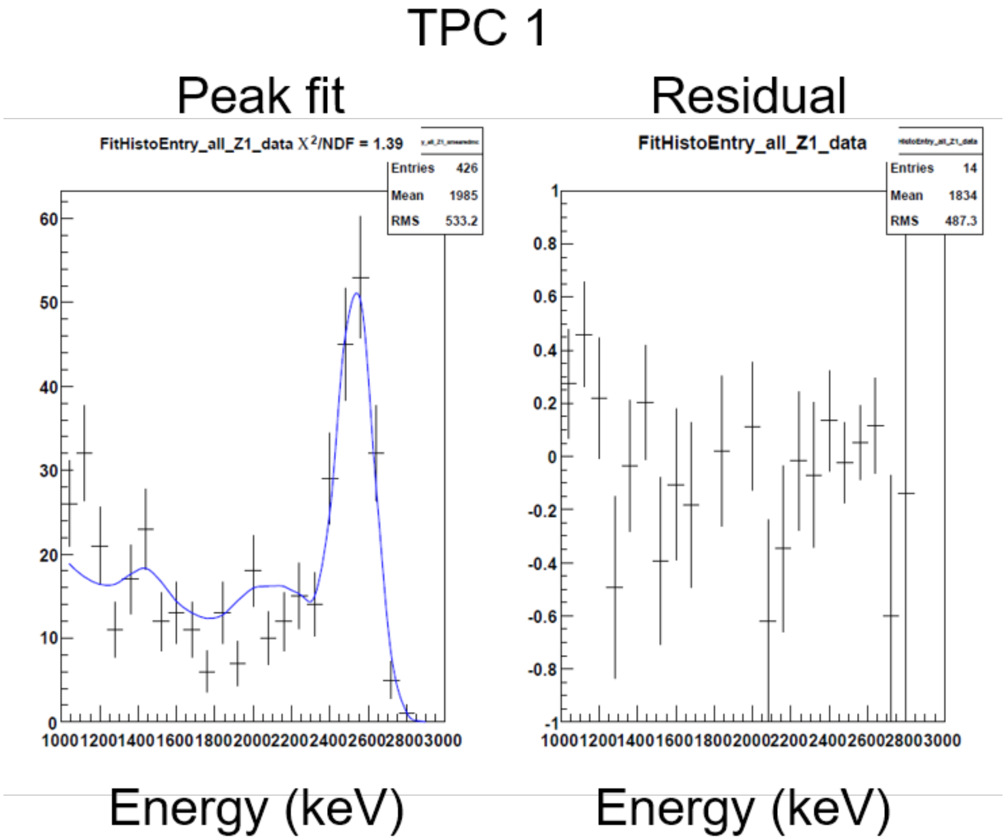

Figure 2.11: To check the results of this 2D fit, one must look at the drift-time bin fits as with the previous electron lifetime methods. One drift-time bin of the full TPC fit is shown here.

including deep underground detector placement.

Despite reduction techniques, EXO-200 has backgrounds from both radionuclides and cosmic-ray-related events. This section will focus on backgrounds related to cosmic-ray-induced neutrons.

2.4.1 Muon-induced neutrons in EXO-200

Muons created by cosmic rays can pass near the TPC and create fast neutrons through spallation. Those neutrons produce a gamma background which potentially mimics the double-beta decay signal. One of the main backgrounds from neutrons is due to neutron

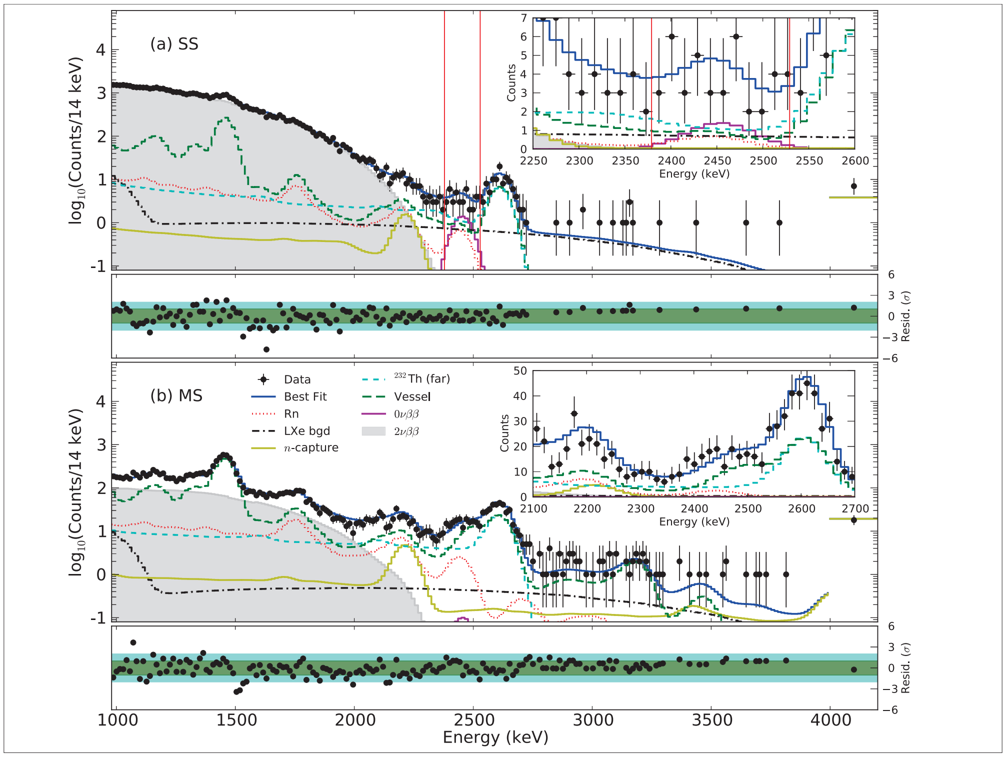

Figure 2.12: EXO-200 $0\nu\beta\beta$ fit using Phase I data. The top panel shows SS (single-site) events, and the bottom panel shows MS (multi-site) events. The red lines in the top panel indicate the $\pm 2\sigma_E$ ROI. This figure is from [12].

capture on ^{136}Xe, which produces ^{137}Xe and decays into ^{137}Cs with a Q-value of 4.17 MeV and half-life of 3.8 min. Capture gammas can potentially mimic the double beta decay signal, but the primary background from ^{137}Xe production is beta decay.

Properly fitting these backgrounds is necessary for understanding the EXO-200 double beta decay spectrum. As experiments move to greater sensitivity (nEXO), understanding and mitigating backgrounds becomes even more important.

^{137}Xe decays contributed to 7.0 out of $31.1 \pm 1.8(stat.) \pm 3.3(sys.)$ counts in the single-site ROI [12]. This contribution to background counts was consistent with activation estimates from another study [21].

The cosmogenic background study with EXO-200 data focused on data coincident with muon veto panel triggers, which yields a neutron-enriched dataset. Subsequently, this dataset

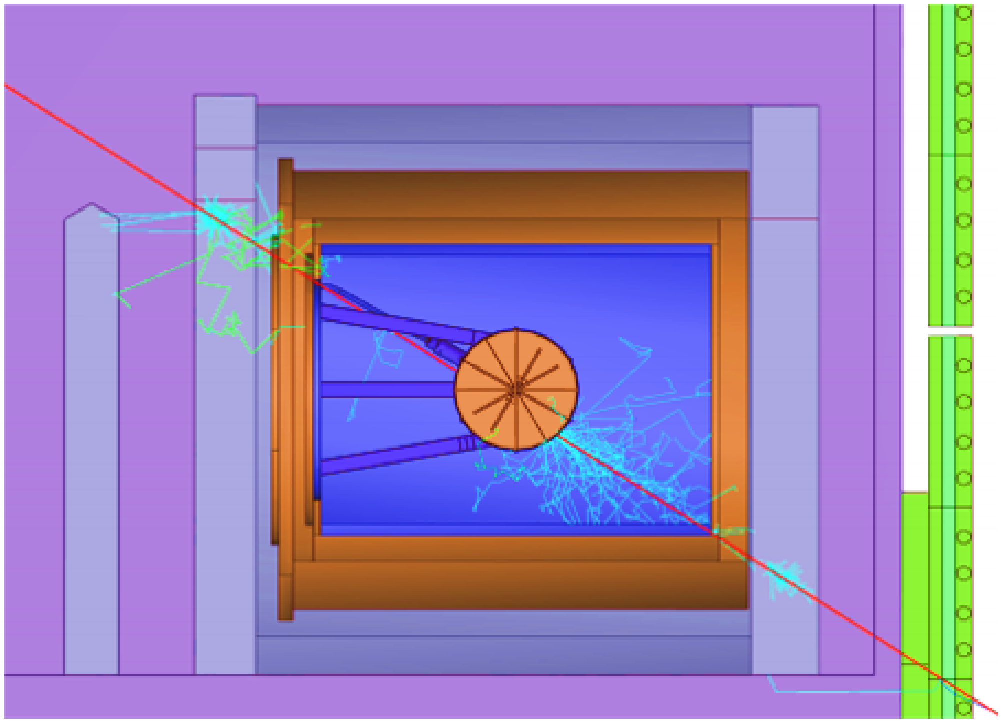

Figure 2.13: Rendering of muon passing through EXO-200. Muon track shown in red.

was used to measure cosmogenic neutron capture rates on various detector components, including ^{136}Xe itself, shown in Fig. 2.14. The ^{136}Xe neutron capture rate for EXO-200 was measured to be 338^{+132}_{-93} counts per year.

Background due to ^{137}Xe decays can be reduced by identifying the neutron capture gammas from ^{136}Xe (n,g)^{137}Xe. This technique is discussed further in Chapter 4.

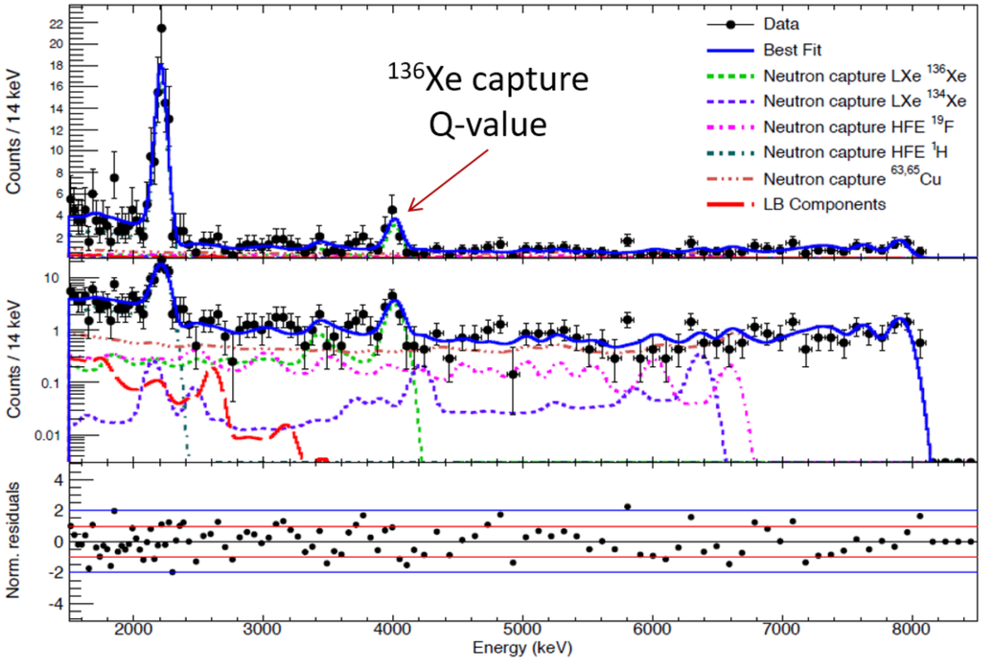

Figure 2.14: EXO-200 veto-coincident data and MS spectrum fit. Original figure from [21].

Chapter 3

Neutron capture on ^{136}Xe at the Detector for Advanced Neutron Capture Experiments

3.1 Introduction

Due to the rarity of $0\nu\beta\beta$ decays, a successful search requires extremely low radioactivity in detector materials to minimize backgrounds. As a noble gas, ^{136}Xe can be highly purified, and detectors can be constructed with extremely radiopure materials. Techniques such as event multiplicity discrimination [20] can be used to further reduce backgrounds due to γ-rays from radioactive decays. One background which cannot be reduced through these techniques is the β decay of ^{137}Xe. In a recent $0\nu\beta\beta$ search by the EXO-200 collaboration [12], ^{137}Xe β decay was estimated to be responsible for 20% of backgrounds in the $0\nu\beta\beta$ signal region of interest.

A separate study by the EXO-200 collaboration [21] found that ^{137}Xe in the detector was overwhelmingly produced by $^{136}\text{Xe}(n,\gamma)^{137}\text{Xe}$ interactions with neutrons produced from cosmic-ray muon interactions underground. It is possible to reject a significant fraction of this background by identifying the production of ^{137}Xe and implementing a veto to remove the subsequent decays (3.8 minute half-life [22]) from the dataset.

To better understand backgrounds and to facilitate the development of such a veto, we have studied the $^{136}\text{Xe}(n,\gamma)^{137}\text{Xe}$ interaction using the Detector for Advanced Neutron Capture Experiments (DANCE). The relative neutron capture cross sections for neutrons at thermal energies and the first ^{136}Xe resonance at 2.154 keV were measured, as well as the energies and multiplicities of cascade γs for thermal and resonant captures. This work was published in Ref. [23], with some further details discussed below. This information may be used by EXO-200 and other collaborations to improve the sensitivity of their $0\nu\beta\beta$ searches, and may also provide insight into the nuclear structure of ^{137}Xe.

3.2 Experimental Method

3.2.1 DANCE

DANCE is located on Flight Path 14 at the Manuel Lujan Jr. Neutron Scattering Center at the Los Alamos Neutron Science Center. This flight path is exposed to neutrons that pass through a room-temperature water moderator. The target sample, centered within the detector, is 20.25 m downstream of the moderator. Prompt γ-rays are measured from neutron capture using 160 BaF_2 crystals arranged spherically around the target, shown in Fig. 3.1, covering a solid angle of $\sim$3.5π steradians. Each crystal is 15 cm long, has a volume of 734 cm^3, and is monitored by a photomultiplier tube (PMT). BaF_2 crystals have fast timing resolution, which allows for precise neutron time-of-flight measurement, and the segmentation is ideal for measurement of γ-cascade multiplicity. The space between the evacuated beam pipe and the inner surfaces of the crystals (at 16.5 cm radius [24]) is filled with a ^{6}LiH shell to reduce the rate of scattered neutrons capturing on the BaF_2 crystals. Further information on the detector can be found in Ref. [25].

3.2.2 Data Acquisition

Neutrons were incident on a 3 cm thick sample of 99.9% isotopically pure, gaseous ^{136}Xe pressurized to an average of 26 psi absolute pressure. The xenon gas was contained in an aluminum cell with 2.9 cm diameter, 0.003 inch thick kapton windows allowing the neutron beam to pass through, shown in Fig. 3.2. Fig. 3.3 shows the xenon pressure during the data acquisition. The xenon pressure was recorded several times per day. A slow and steady leak of xenon was present during the data-taking, and the xenon target was refilled once. Despite

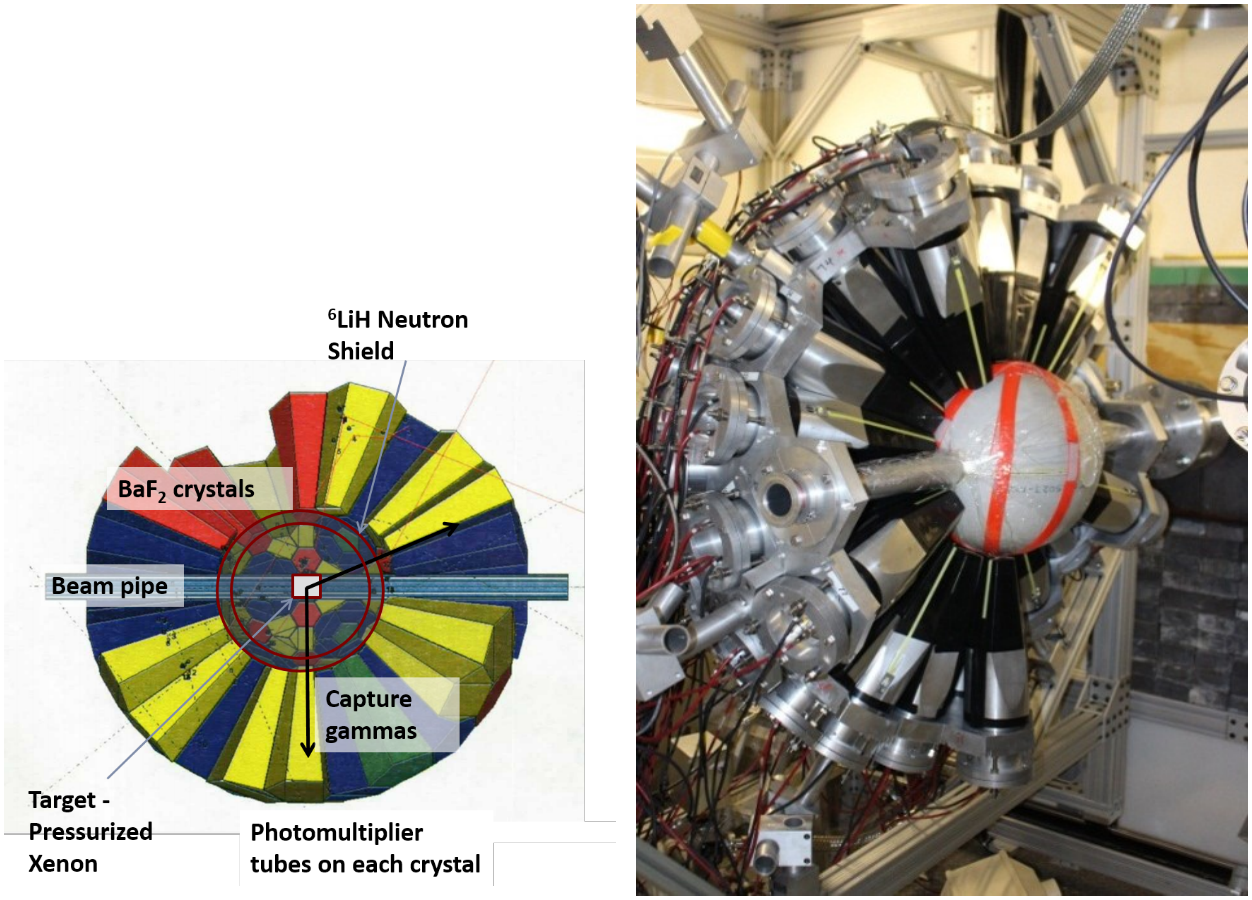

Figure 3.1: DANCE schematic and picture. Picture on the right shows the two halves of the array separated, with the ^6LiH neutron shield exposed.

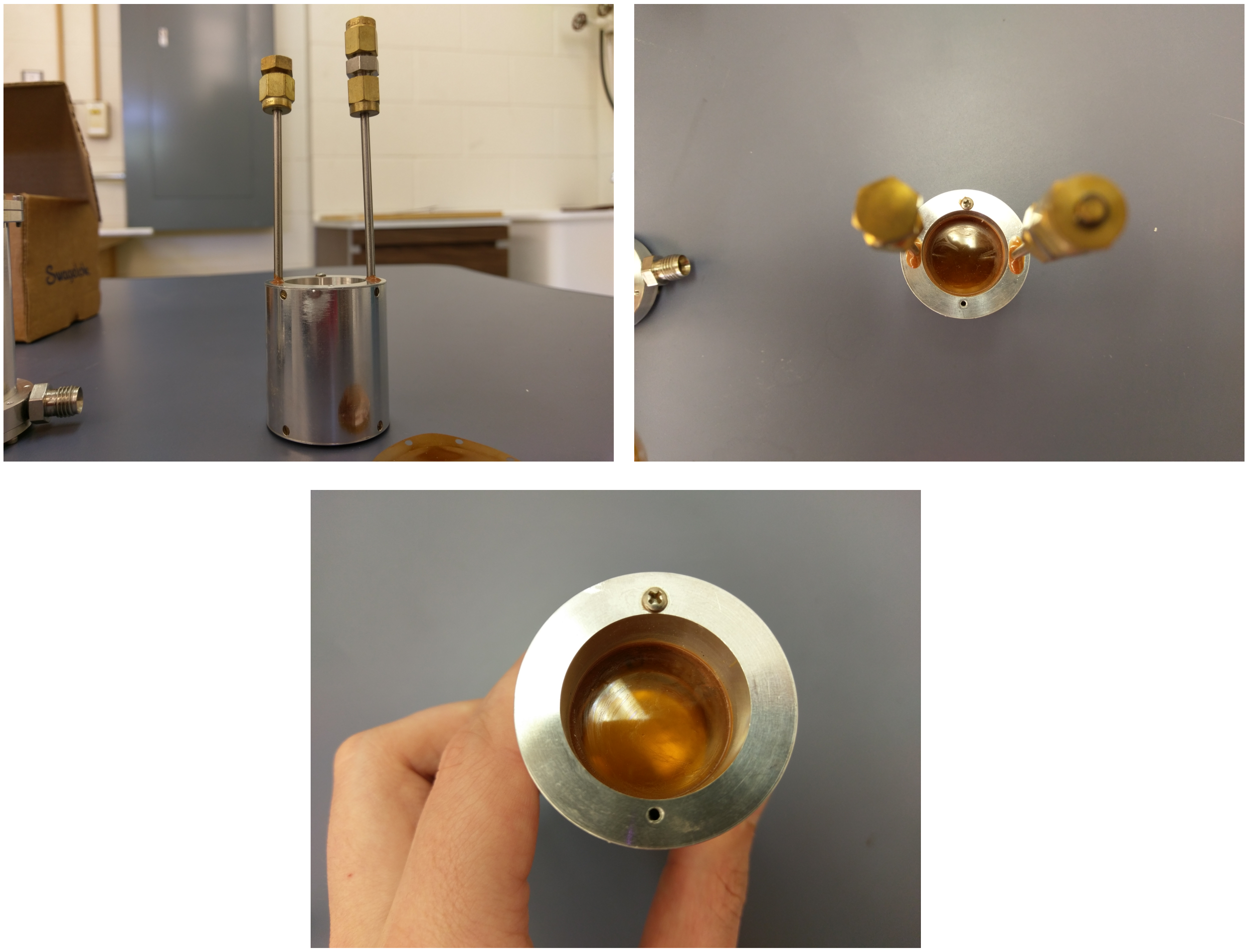

Figure 3.2: Gas target used in the ^{136}Xe DANCE experiment. The body is aluminum, with two endcaps sealed with butyl o-rings. Two 1/16" lines attach to the top of the target allowing for input and output gas flow. The windows are 3 mil kapton sealed with epoxy.

this steady leak, a linear fit to the pressure gives an accurate xenon pressure throughout the experiment. Data were also taken with the same cell evacuated, allowing for determination of the beam and target-related backgrounds. As the beam diameter was smaller than 2 cm at the target, the full flux of neutrons was incident upon xenon.

The data was collected by two digitizers each recording a 256 μs long window. These time windows were set to a delay relative to the initial neutron beam trigger to select specific neutron energies based on time of flight. The first time window was set to look at the high neutron energy events, including the 2.154 keV ^{136}Xe capture resonance, while the second

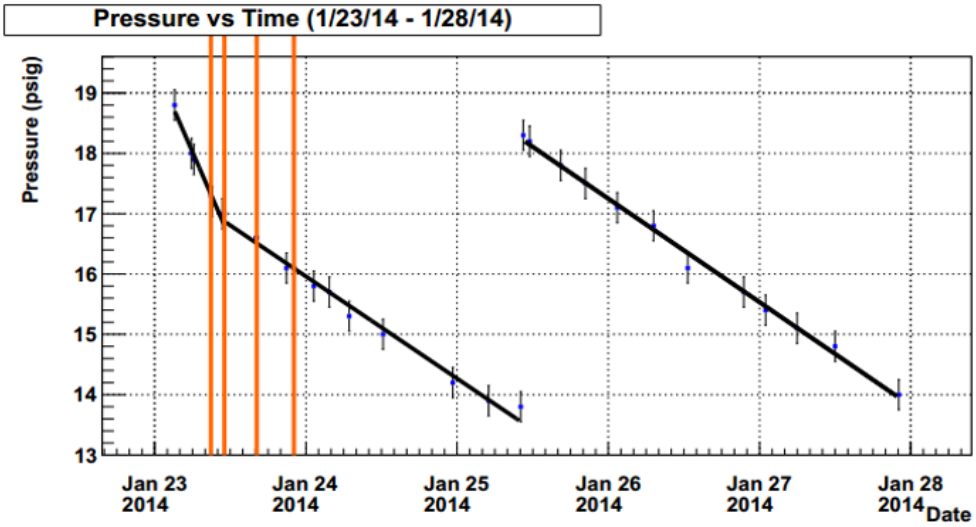

Figure 3.3: Pressure vs. time plot for the second data run at DANCE. The orange lines show adjustments being made to the gas manifold. The second orange line shows an improvement to the apparent leak in the target and manifold assembly. Fits were made to the pressure measurements for a very good determination of the pressure, despite the leak.

was delayed by 9.15 ms to look at the thermal neutron energy range of 0.0243 to 0.0256 eV. Within each of these time windows, all signals from the PMTs mounted to the crystals were recorded. The energy windows used in analysis are shown in Fig. 3.4.

3.2.3 Neutron Flux Determination

Located downstream of the sample location are three neutron monitors that are used to measure the neutron flux as a function of energy. These monitors use the $^{6}\mathrm{Li}(n, \alpha t)$ reaction, the $^{235}\mathrm{U}(n, f)$ reaction, and the $^{3}\mathrm{He}(n, p)$ reaction. As the beam diameter is smaller than both the xenon target and the beam monitor, we measure the total neutron rate per beam spill as a function of time of flight (which is converted to neutron energy). The $^{6}\mathrm{Li}(n, \alpha t)$ monitor has good performance at both thermal and resonant energies, so it was used for this measurement. The $^{3}\mathrm{He}(n, p)$ and $^{235}\mathrm{U}(n, f)$ monitors were used for cross-checks, and showed good agreement for the measured flux shape.

The neutron rate was determined by using a surface barrier Si detector to count $^{6}\mathrm{Li}(n, \alpha t)$

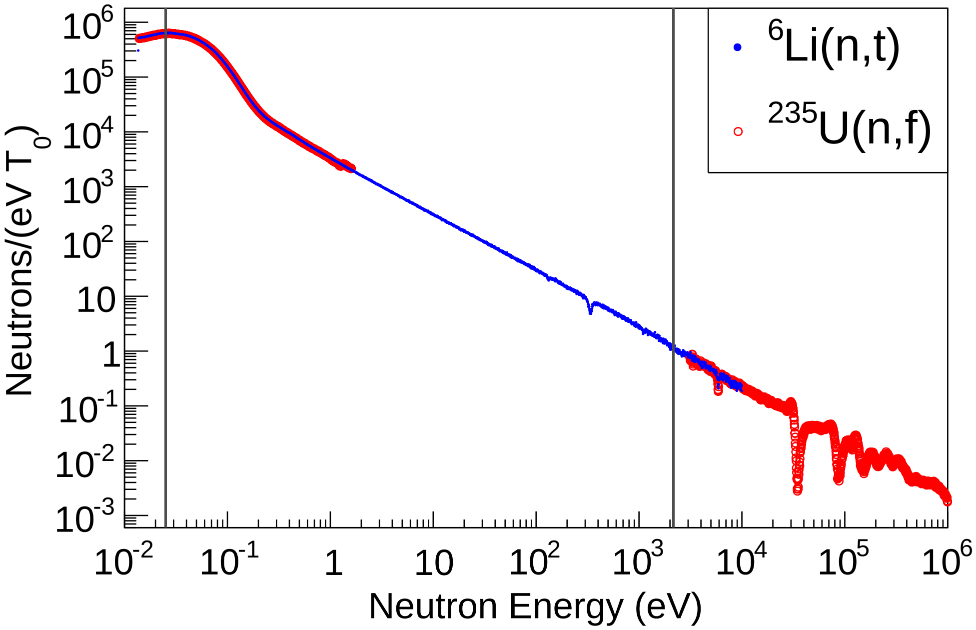

Figure 3.4: Neutron flux measured by the ^{6}Li and ^{235}U neutron monitors. The flux is integrated over the regions indicated by the dark grey bars for calculation of our thermal and resonance cross sections. The gap in flux measurement using the ^{235}U monitor is due to an energy region with resonances that make the flux difficult to evaluate.

interactions in a ^{6}LiF layer deposited on a thin kapton film. The number of interactions were converted to a flux measurement using knowledge of the beam and detector geometry and the known cross section [26] for this interaction. The measured flux as a function of incident neutron energy is shown in Fig. 3.4. As only the ratio of fluxes at different energies is necessary for this analysis, uncertainties due to the absolute calibration of the neutron monitors are negligible.

3.2.4 Radioactive Source Analysis

In order to confirm understanding of DANCE's response to γ-rays, source data was taken with a number of different sources. Those of particular interest are ^{22}Na, ^{60}Co, ^{88}Y, and ^{137}Cs γ sources. These sources span the range 0.511 to 1.82 MeV in gamma energy. Primarily, only gamma decay products are detected by DANCE. Secondary effects, such as positron annihilation in the ^{22}Na emitting two 511 keV gammas are also detected.

The data from these sources were used to show agreement between the DANCE simulation and data at different event multiplicities. Each of these sources were simulated in Geant4 [27, 28] using the DANCE Geant geometry. A quarter inch thick by 1 inch diameter polyethylene disk was added to the simulation model in order to model the source capsule, with the decaying isotopes placed at the very center of the disk. The beampipe in these simulations was filled with air as it was during the data runs. These additions did not produce a significant change in the simulation results.

Two simulations were done for each source. One simulation was done for each of the two digitizer cards. It was found that the data taken on each of two digitizer cards had a different resolution. Fits to gamma cluster peaks were performed for ^{22}Na, ^{137}Cs, and ^{88}Y. Finally, a fit to these results yielded resolution as a function of gamma energy for each digitizer card. The 3.4 MeV gamma from our xenon data was added to constrain higher energy resolutions.

Multiplicity 1 source simulations for all sources varied significantly from data, but these differences can be attributed to noisy data events. Only multiplicities 2 and above were used for the cross section analysis.

See the appendix for more details about the source runs and agreement.

3.3 Data Analysis

3.3.1 Event Reconstruction

After a applying a timing calibration, all PMT signals occurring within a 20 ns window are grouped together as a single event. Only crystals with measured energy above the threshold of 250 keV are counted. We determined, based on measured event rates and Poisson statistics, that the probability for two or more neutron-induced events to overlap within a single 20 ns coincidence window is less than 1% at the capture resonance energy, and less than 0.1% at thermal neutron energies, so pile-up effects are negligible. This coincidence window is wide enough that uncertainties in relative timings for each PMT do not significantly affect

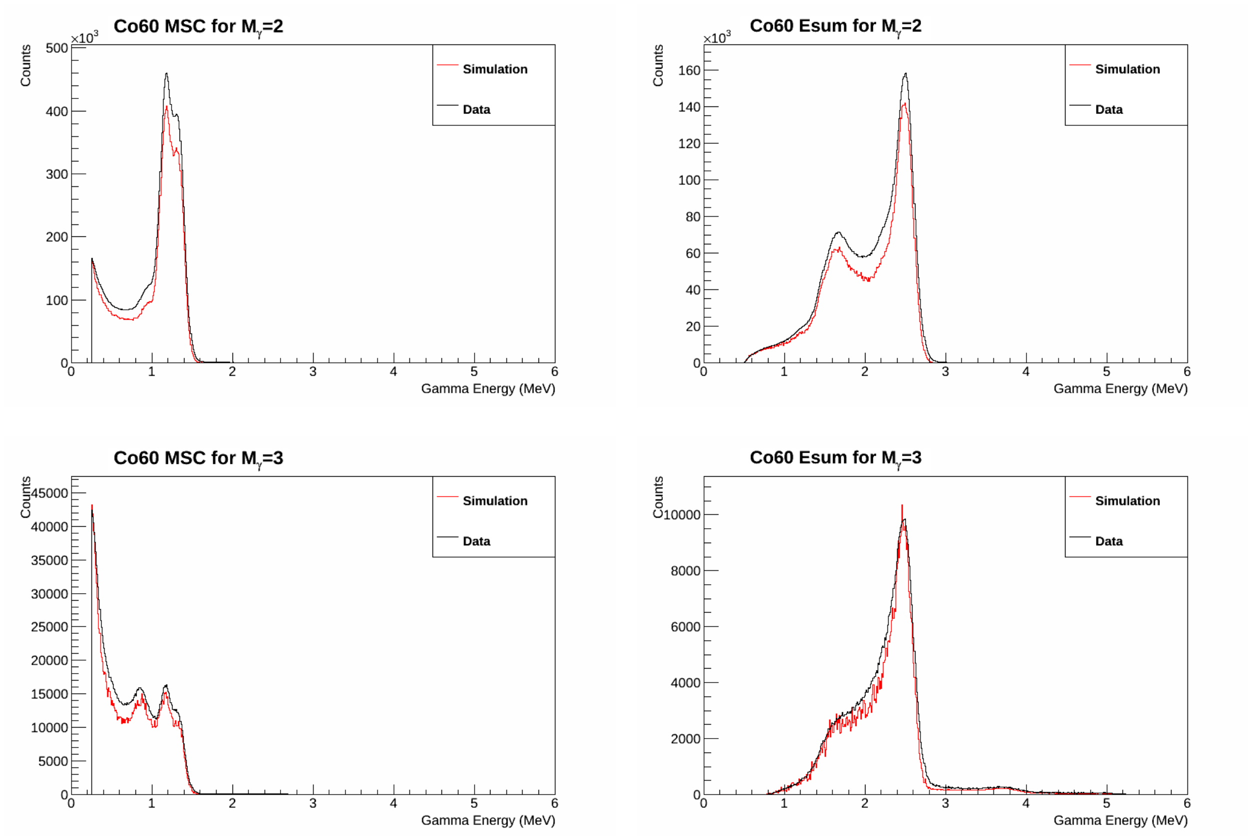

Figure 3.5: Source agreement between data and MC for E_{Σ} and E_{cl} multiplicities 2 and 3 with the ^{60}Co source, taken with digitizer card 0.

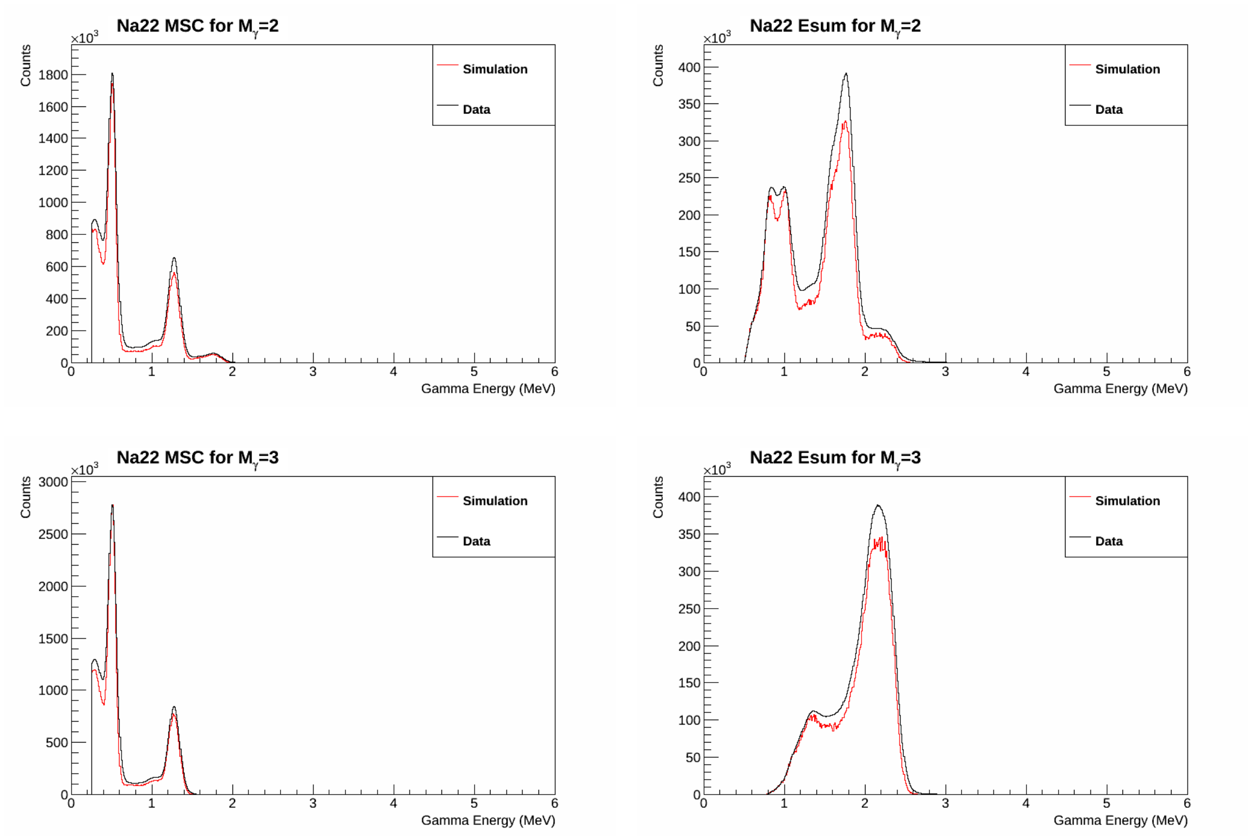

Figure 3.6: Source agreement between data and MC for E_{Σ} and E_{cl} multiplicities 2 and 3 with the ^{22}Na source, taken with digitizer card 0.

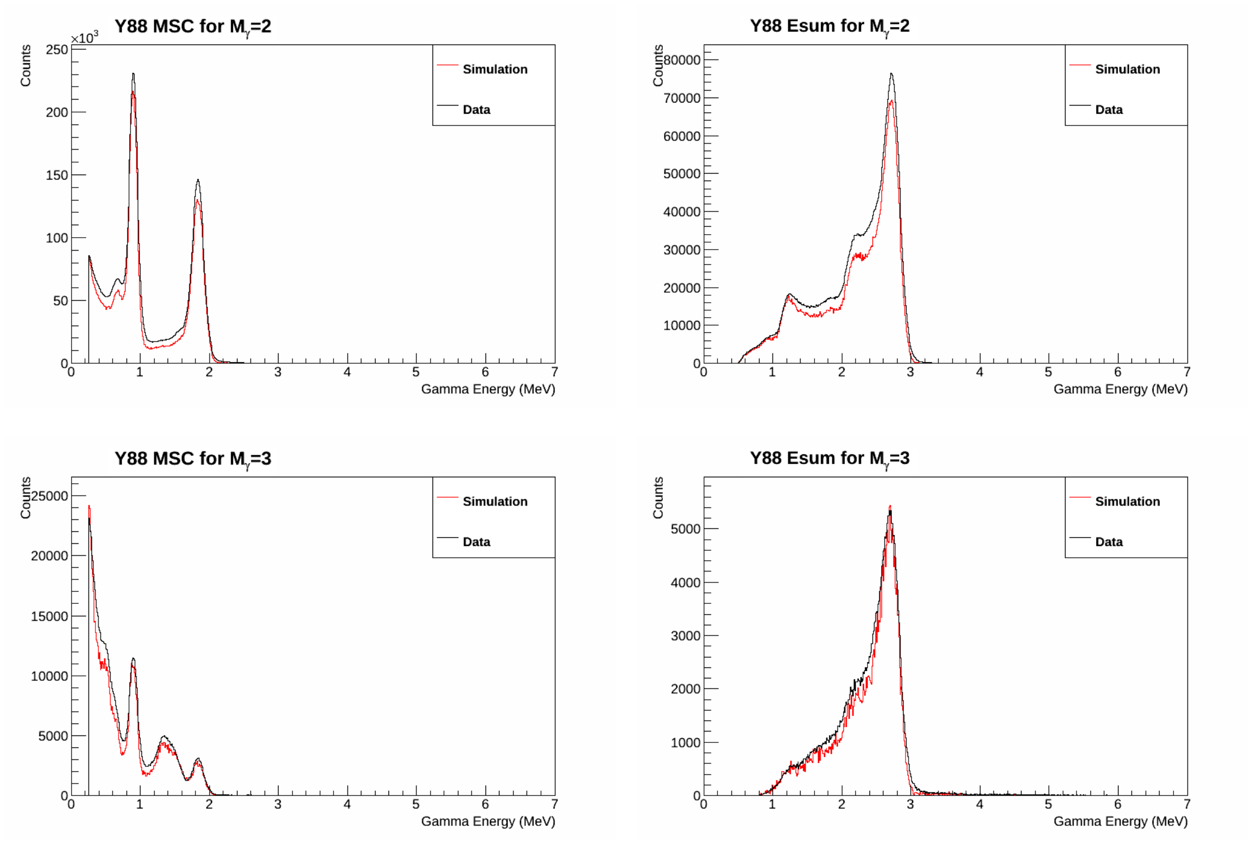

Figure 3.7: Source agreement between data and MC for E_Σ and E_{cl} multiplicities 2 and 3 with the ^{88}Y source, taken with digitizer card 0.

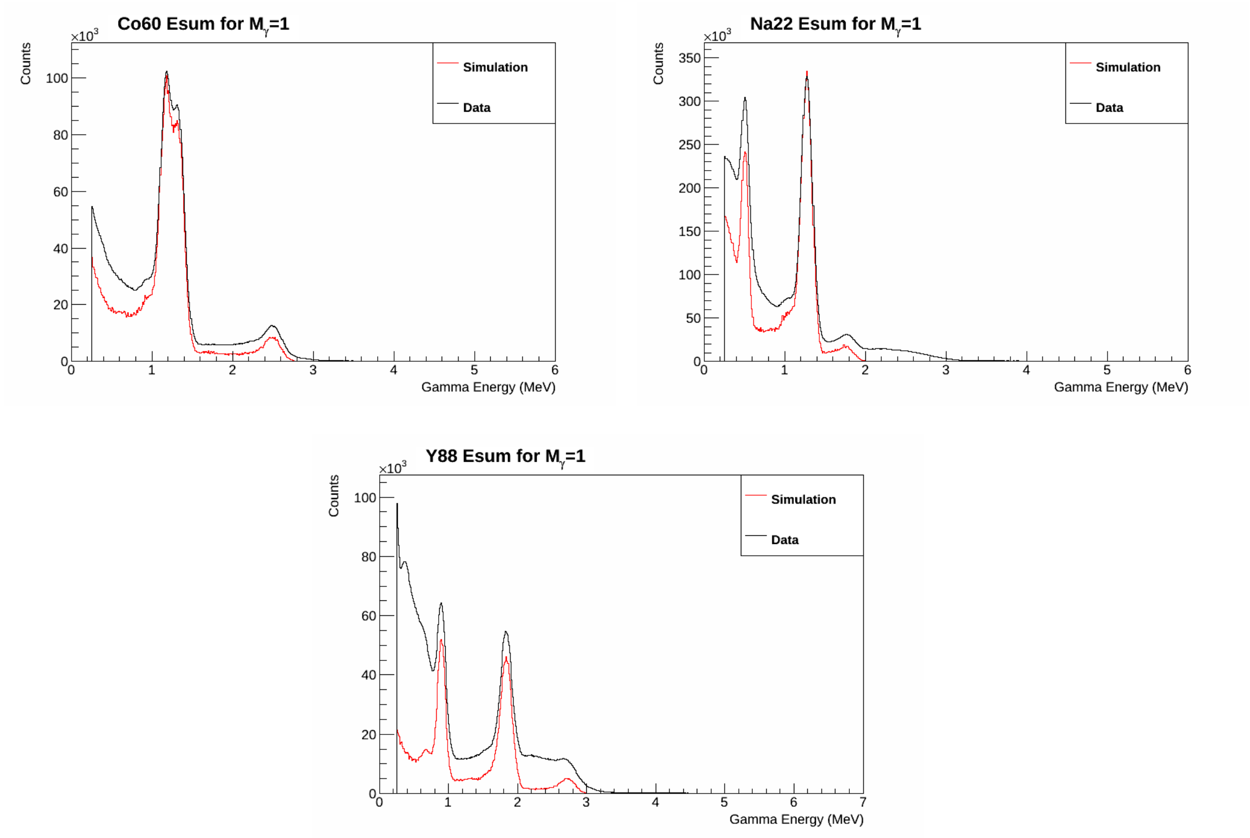

Figure 3.8: Source agreement between data and MC for E_Σ for single multiplicity events with the^{22}Na, ^{60}Co, and ^{88}Y sources, taken with digitizer card 0.

efficiency.

Scintillation light in the BaF_2 crystals has a fast ($\sim$0.6 ns) and slow ($\sim$0.6 μs) component. The ratio of fast to slow scintillation light can be used to discriminate between α-induced signals and those from β decay or γ-rays. This discrimination allows for a near perfect suppression of α-backgrounds to neutron capture signals. The α decay signals were collected and used for the energy calibration of the BaF_2 crystals.

The remaining events with γ-like fast/slow ratios were analyzed for neutron capture studies. Often, γ-rays from neutron captures will Compton scatter and deposit energy in multiple adjacent crystals. Thus, to reconstruct the γ-ray multiplicity and the full energy of each γ-ray, a clustering algorithm was implemented. Adjacent crystals recording signals in a single 20 ns coincidence window are grouped together as a cluster, and it has been found that these clusters correspond well with individual γ-rays. The reconstructed number of clusters (M_{cl}), individual cluster energies (E_{cl}), sum of all cluster energies (E_{Σ}), and neutron energy (E_n, measured from time of flight) are used in this analysis.

3.3.2 Background Subtraction

Because radioactive ^{226}Ra is a chemical homologue to barium, the crystals have some radioactive contamination. The decay chain from ^{226}Ra includes several α decays, as well as some decays with βs and γs (^{214}Pb and ^{214}Bi in particular). The α decays are easily rejected with the technique described in Sec. 3.3.1, but the β decays in the crystals (and from outside the detector) produce a constant-in-time (CIT) background to neutron capture. This CIT background dominates single-cluster data, and some CIT events have $M_{\text{cl}} \geq 2$ due to beta decays which are accompanied by γ-rays, producing a multi-cluster event.

Another background comes from beam neutrons which may scatter off the xenon and capture on aluminum in the target vessel or beam pipe, or on barium in the crystals. Captures from scattered neutrons dominate the data for $E_{\Sigma} > 3$ MeV.

To appropriately subtract these backgrounds, three separate datasets were used: pres-

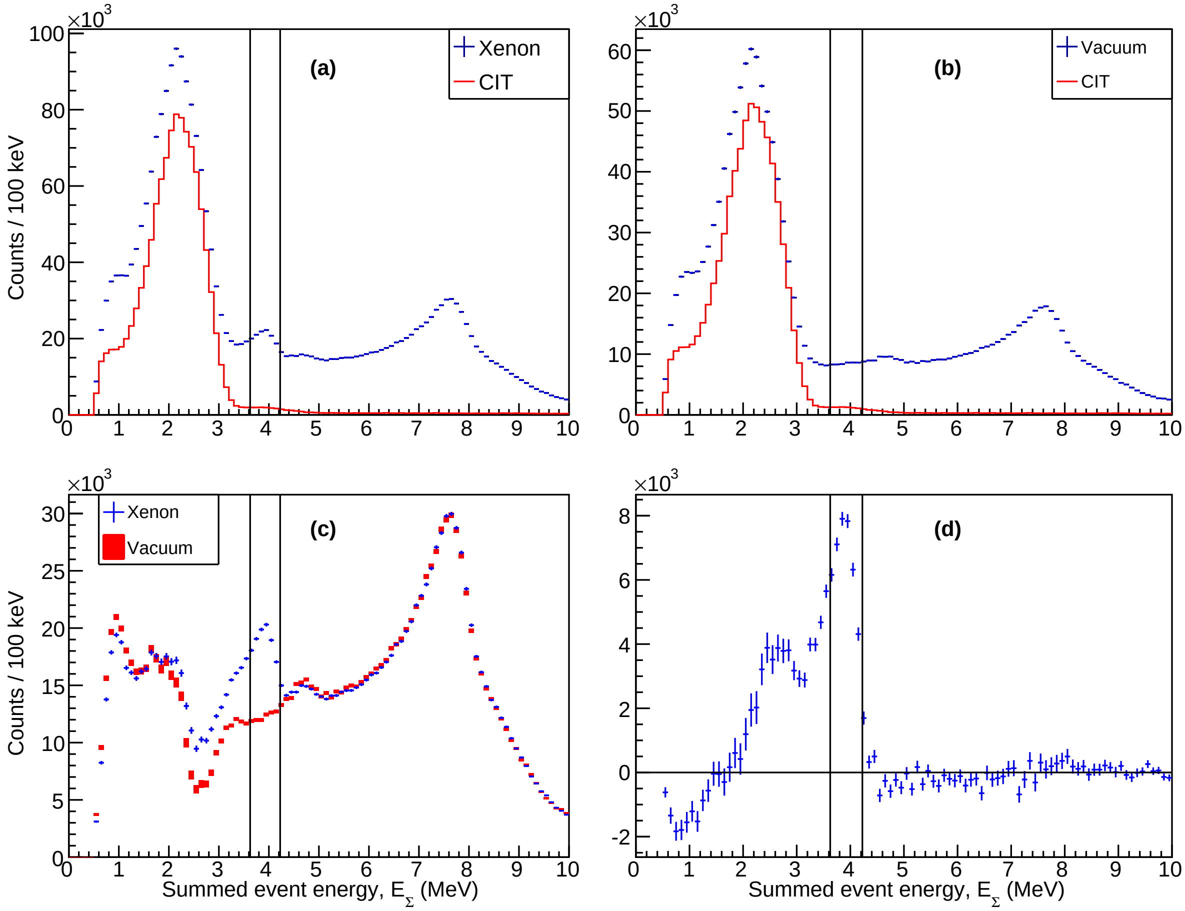

Figure 3.9: (a) Summed event energy for pressurized xenon data at the 25 meV neutron energy window and for beam-off data (also called constant in time, CIT), including cluster multiplicities 2 through 5. The beam-off data have been scaled by livetime. (b) Same as (a), but with evacuated target data rather than pressurized xenon data. (c) Summed event energy for pressurized xenon data and evacuated target data both at the 25 meV neutron energy window after the CIT backgrounds have been subtracted. The evacuated target spectrum has been scaled so that the counts in the 6 to 9 MeV region match the pressurized xenon data. (d) Summed event energy spectrum after the evacuated target data has been subtracted from the pressurized xenon data. For all panels, the Q-gate used in this analysis is indicated by black vertical lines.

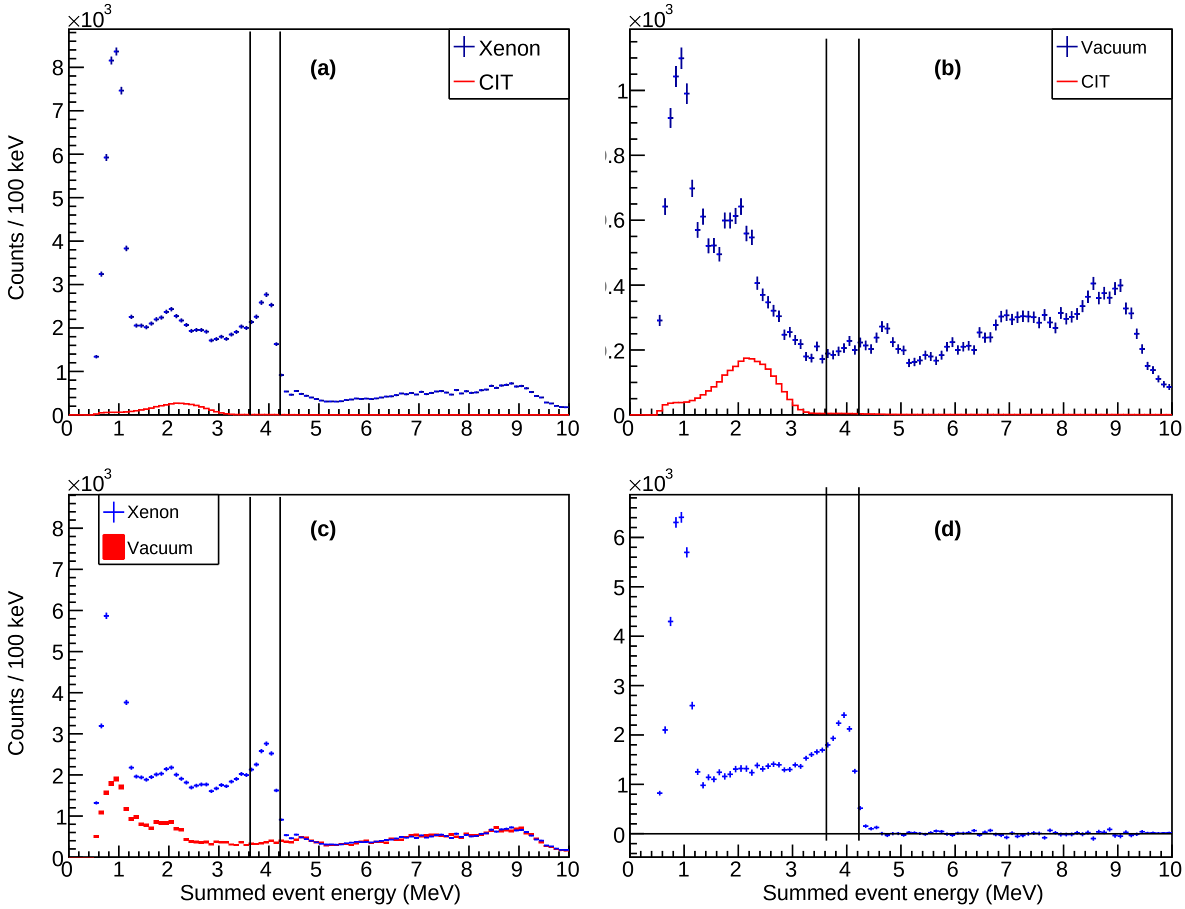

Figure 3.10: Same analysis as Fig. 3.9, but in the resonance region. (a) Summed event energy for pressurized xenon data at the 2.154 keV neutron energy window and for beam-off data, including cluster multiplicities 2 through 5. The beam-off data have been scaled by livetime. (b) Same as (a), but with evacuated target data rather than pressurized xenon data. (c) Summed event energy for pressurized xenon data and evacuated target data both at the 2.154 keV neutron energy window after the CIT backgrounds have been subtracted. The evacuated target spectrum has been scaled so that the counts in the 6 to 9 MeV region match the pressurized xenon data. (d) Summed event energy spectrum after the evacuated target data has been subtracted from the pressurized xenon data. For all panels, the Q-gate used in this analysis is indicated by black vertical lines.

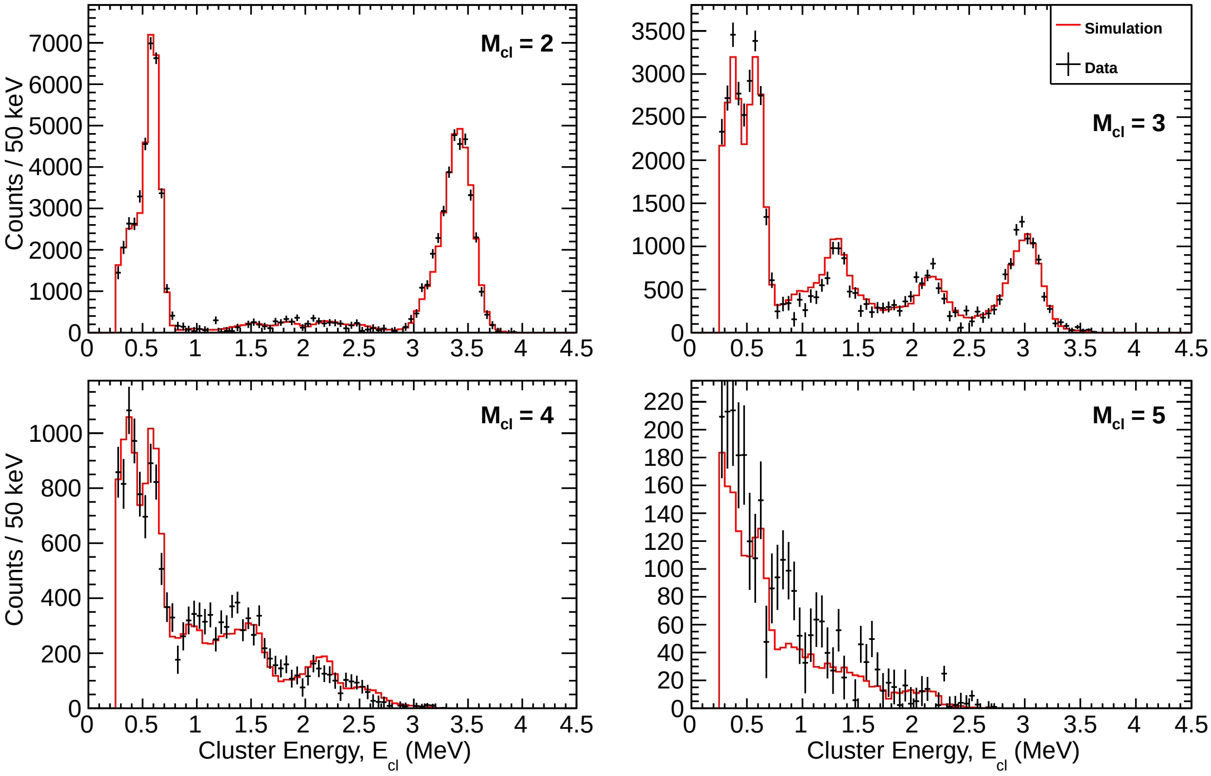

Figure 3.11: Measured and simulated MSC spectra from the ^{136}Xe capture cascade in the 25 meV neutron energy window for cluster multiplicities 2 through 5. The simulated spectra, shown in red, represent the DICEBOX realization best matching the experimental data.

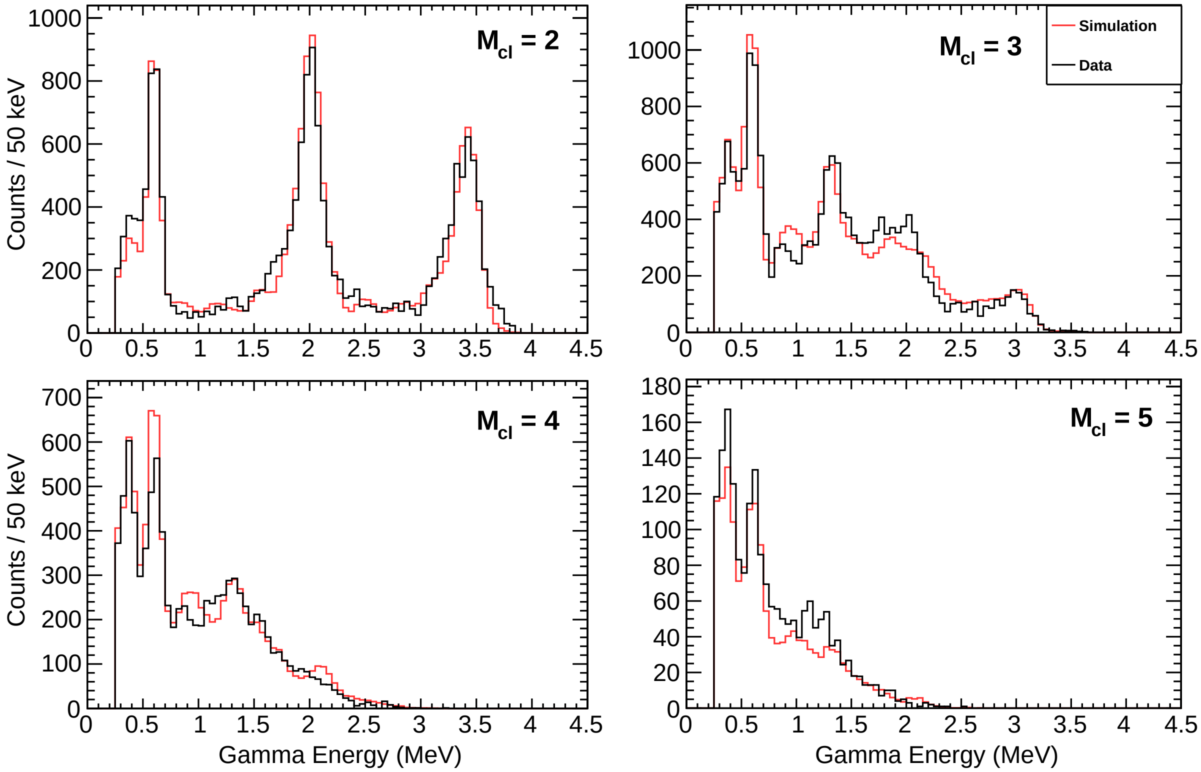

Figure 3.12: Measured and simulated MSC spectra from the ^{136}Xe capture cascade at the 2.154 keV neutron energy resonance for cluster multiplicities 2 through 5. The simulated spectra, shown in red, represent the DICEBOX realization best matching the experimental data.

surized xenon target with incident beam (pressurized xenon data), evacuated target with incident beam (evacuated target data), and no target with no neutron beam (beam-off data). The evacuated target data measure backgrounds due to scattered neutron capture (as neutrons may still scatter off the kapton windows), and beam-off data measure the CIT backgrounds. While the scattered neutron capture backgrounds seen at different times of flight scale with the number of scattered neutrons, CIT backgrounds scale only with livetime, so these must be treated separately.

First, the CIT data were scaled to match the livetimes of both the pressurized xenon and evacuated target data, and the CIT spectra were subtracted from the pressurized xenon and evacuated target spectra at each multiplicity. Panels (a) and (b) in Fig. 3.9 show the CIT background scaled to the pressurized xenon and evacuated target data in the thermal neutron energy window. Only a very small fraction of the CIT background has $E_\Sigma > 3.5$ MeV. The background subtractions are shown for two different neutron energies: thermal neutron energies in Fig. 3.9 and 2.154 keV neutrons in Fig. 3.10

Panel (c) of Fig. 3.9 shows the resultant spectra for the pressurized xenon and evacuated targets after the CIT background subtraction. The evacuated target spectrum was scaled to match the number of counts in the pressurized xenon spectrum in the 6 to 9 MeV E_Σ range. This is well above the 4.025 MeV ^{136}Xe neutron capture Q-value, so the events in this range are only due to scattered neutrons. In this way, CIT backgrounds and scattered neutron capture backgrounds are appropriately subtracted, as seen in panel (d) of Figure 3.9, leaving a large peak at the ^{136}Xe(n,γ) Q-value, and an excess at lower energies due to Xe capture events where some fraction of the γ cascade energy is lost. While Fig. 3.9 illustrates the subtraction process with E_Σ spectra, the same procedure, with the same scale factors, is applied to all relevant spectra, including those of individual cluster energies.

A valley in both the signal and background is apparent between 2.2 and 3.2 MeV in panel (c) of Fig. 3.9. This may be due to a small energy mis-calibration with the beam-off data, or imperfect background subtraction. This valley is most apparent where the slope of the beam-off spectrum is steepest. The beam-off spectrum is small relative to ^{136}Xe capture and relatively flat in the region near the ^{136}Xe Q-value, so any possible energy mis-calibration would have a negligible effect on the analysis. The beam-on pressurized xenon and evacuated target data share the same energy calibration.

As both the CIT and scattered neutron backgrounds largely come from γ or β emission inside a single crystal, the data for $M_{\mathrm{cl}} = 1$ are dominated by backgrounds. Hence, this analysis largely uses only $M_{\mathrm{cl}} > 1$ spectra. There were almost no events with $M_{\mathrm{cl}} > 5$. To minimize errors due to imperfect background subtraction, we further restricted the analysis to events with 3.625 MeV $< E_{\Sigma} \leq$ 4.225 MeV. This "Q-gate" optimizes the signal to background ratio and avoids most of the CIT backgrounds while still leaving good statistics. One exception, where $M_{\mathrm{cl}} = 1$ data was used, is discussed in Sec. 3.3.3.

One additional background source comes from γ-rays (mainly 2.2 MeV from capture on hydrogen in the neutron moderator) that may travel down the beam pipe and pair-produce in the xenon, yielding a pair of 0.511 MeV γs due to positron annihilation. These signals are mainly found at short time of flight, and have a total energy far below the Q-gate. No subtraction of these beam backgrounds was necessary, as they could not affect the analysis.

3.3.3 Cascade Modeling

To optimize identification of the ^{136}Xe (n,γ) reaction in $0\nu\beta\beta$ searches such as EXO-200, the cascade from the capture to the ground state of ^{137}Xe must be known as precisely as possible. We use multi-step cascade (MSC) spectra to evaluate cascade models. We define MSC spectra as the spectra of E_{cl} at each cluster multiplicity ($M_{\mathrm{cl}} = 2-5$). We compare the MSC spectra measured with the DANCE detector to predictions derived from simulations and candidate cascade models. We use a Geant4 simulation which features the DANCE geometry and detector response [29] for cascades produced with the DICEBOX code [30] in a way similar to that in Ref. [31]. For this analysis, we added the geometry of the aluminum target and pressurized xenon into the Geant4 simulations and assumed that the captures occur uniformly in the Xe target.

The DICEBOX code uses existing information on levels below a certain critical energy ($E_c = 2.65$ MeV in this analysis), including intensities of primary transition to these levels and subsequent transitions. Individual levels above E_c and γ transitions from these levels are generated "randomly" based on statistical models of nuclear level density and photon strength functions. Each set of levels and transitions is called a "nuclear realization" [30]. Assuming the data for levels below E_c is accurate and complete, and given enough realizations, a model closely matching the cascade found in nature should be achievable. After the information on levels below E_c was finalized, 100 nuclear realizations were simulated for thermal capture, and 200 for resonant capture, each with 10^5 cascades. The nuclear realization best describing the spectra was chosen based on the global χ^2 agreement for all bins in MSC spectra for $M_{\text{cl}} = 2 - 5$. The chosen realizations were re-produced with 10^6 cascades, for better statistics. Fig. 3.11 shows the agreement of MSC spectra for the chosen nuclear realization with the experiment for the thermal neutron energy window. There is only one common normalization factor for all multiplicities, so the good agreement indicates an accurate multiplicity distribution.

The information on the decay scheme below E_c was taken from ENSDF [32], largely based on the thermal neutron capture work by Prussin *et al.* [33]. Transition intensities were slightly adjusted to improve the agreement between data and simulations. The changes to the thermal capture cascade, from that described in Prussin's measurement, were relatively minor. On the other hand, no information on cascade transitions was available for decay of the 2.154 keV resonance. The primary transitions from this resonance were initially based on the thermal cascade model, but significant adjustments were made manually to reproduce the resonance MSC spectra.

The neutron capture cascades for the thermal neutron window and 2.154 keV resonance window show significant differences, as seen in Fig. 3.11 and Fig. 3.12. This is not surprising as the initial states are different – the 2.154 keV resonance is a p-wave $3/2^-$ state, while thermal neutrons (s-wave) produce a $1/2^+$ state.

The most visible difference is a strong two-step cascade seen in the middle of the $M_{\mathrm{cl}} = 2$ MSC spectrum for the resonance. Its presence indicates the existence of a $J = 5/2$ state at $E \simeq 2$ MeV – this is the only spin which allows dipole transitions to connect the neutron capturing state (presumed to be $J^\pi = 3/2^-$ [34]) with the ground state ($J^\pi = 7/2^-$). A level with this spin cannot be strongly populated in thermal neutron capture as it cannot be accessed via a dipole primary transition from the thermal capture state ($J^\pi = 1/2^+$). Several levels near 2 MeV excitation energy have been reported from studies of β decay of the $7/2^+$ ^{137}I ground state [32].

Direct transition from the thermal capture state to the ground state would require an octopole transition (extremely suppressed), and has not been observed in previous experiments [33]. However, for capture at the 2.154 keV resonance, a direct transition to the ground state could be achieved with an electric quadrupole transition, and would show up in the $M_{\mathrm{cl}} = 1$ data as a peak at $E_{\mathrm{cl}} = 4027$ keV. As the $M_{\mathrm{cl}} = 1$ data is background-dominated and contains important features missed with the usual Q-gate selection on E_Σ, a separate study was performed to measure the possible intensity of this primary transition. After background subtraction (as described in Sec. 3.3.2), the expected peaks at $E_{\mathrm{cl}} = E_\Sigma = 4027$ keV and 3424 keV were observed in the $M_{\mathrm{cl}} = 1$ spectrum. Peaks at lower energies were unusable due to large unsubtracted backgrounds. Simulations of the known capture cascade were performed with varying intensities of the direct transition to the ground state until the two peaks were well reproduced, although a relatively flat background spectrum of unknown origin remained. Based on this, we determined that resonant captures will transition directly to the ground state $2.3 \pm 1.0\%$ of the time. This contribution to the decay was added to the resonant cascade model for DICEBOX. Because the $M_{\mathrm{cl}} = 2 - 5$ data is not sensitive to this transition, and because the $M_{\mathrm{cl}} = 1$ backgrounds are not fully understood, a separate systematic uncertainty was included to account for this transition.

The decay scheme, represented as the relative intensities of emission as a function of

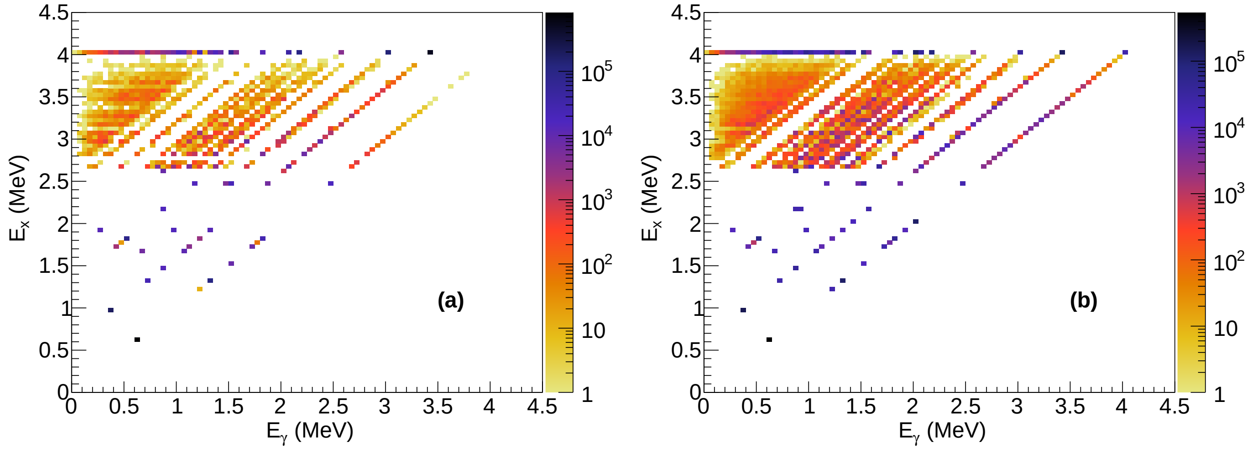

Figure 3.13: Capture cascade γ-ray emission intensities from the DICEBOX realizations that best match the data as a function of excitation energy and γ-ray energy. These correspond to the red lines on the MSC plots in Fig. 3.11 and Fig. 3.12. (a) Cascade model for thermal neutron capture (b) Cascade model for 2.154 keV ^{136}Xe neutron capture resonance. Intensities (color scale) are expressed as transitions per 10^6 captures.

initial energy and γ-ray energy are, for both thermal and $E_n = 2.154$ keV capture, shown in Fig. 3.13. The intensities are given in 50-keV wide bins. Decay cascades corresponding to these schemes are included in the publication [23].

As evident from Fig. 3.11 and Fig. 3.12, simulations do not describe the spectra exactly, especially at higher multiplicity. However, the discrepancies there are small compared to the entire intensity, accounting for only a few percent of all transitions. It should be noted that the number of counts from a cascade is given by M_{cl}, so discrepancies in the MSC histograms for higher multiplicities are exaggerated.

3.3.4 Relative Cross Section

Using the optimal nuclear realizations, we calculated the efficiency for detecting an event within $M_{\mathrm{cl}} = 2 - 5$ and $E_\Sigma = 3.625 - 4.225$ MeV. The efficiency for detecting a thermal (2.154 keV resonance) neutron capture within the selected Q-gate and multiplicity gate was

28.9% (24.9%).

In general, the cross sections can be calculated as

$$\sigma(E_n) = \alpha \frac{N(E_n)}{\epsilon(E_n)\Phi(E_n)}, \tag{3.1}$$

where N is the number of captures passing selection cuts after background subtraction, ϵ is the efficiency for a capture to pass those selections, Φ is the neutron flux, and α is a term containing the xenon gas density and other parameters which are independent of neutron energy. At thermal energy (25 meV) the cross section is near constant (to ±1%) within the measurement energy window. At resonance energy, the cross section varies rapidly with E_n, so the integral of the cross section over the resonance is the preferred way of reporting results. Thus, the cross section ratio between resonance and thermal captures is reported in units of inverse energy. Reporting a ratio, rather than absolute cross sections, allows for considerable reduction of systematic uncertainties, and avoids complications associated with calibrating the absolute flux and efficiency.

The ratio of the cross section in the thermal window to the 2.154 keV resonance integral was found to be 4.10 ± 0.10 (stat.) ± 0.24 (sys.) meV^{-1}. The thermal neutron energy window was centered at 25 meV with a width of 1.3 meV and the resonance neutron energy window was chosen to be from 2094 to 2203 eV, which encompasses the entire resonance within the neutron energy resolution of DANCE.

The systematic uncertainty on the ratio comes from the quadrature sum of the flux ratio uncertainty (1.7%), efficiency ratio uncertainty (3.3%), 4027 keV direct transition uncertainty (0.5%) and an additional uncertainty (4.4%) which accounts for uncertainties in background subtraction. The background subtraction uncertainty was largely determined through tests of the robustness of the measurement with different Q-gates. The efficiency ratio uncertainty was computed by examining efficiency changes due to possible energy mis-calibration, differences in efficiency between DAQ cards, crystal timing calibration, and simulation inaccuracy. The statistical uncertainty, comprised of uncertainty in thermal, resonance, and background counts, is 2.5%.

3.4 Discussion and Absolute Cross Section

The ratio between thermal and resonance cross sections from the ENDF/B-VII.1 evaluation [35] is 6.95 meV^{-1}, considerably different than our measured ratio of 4.10 ± 0.10 (stat.) ± 0.24 (sys.) meV One absolute cross section measurement of the ^{136}Xe 2.154 keV resonance has been reported by Macklin [36]. Converting the resonance kernel value of 30.1 ± 1.5 meV [36] to a resonance integral yields 58.0 ± 2.9 b eV. Combining the relative cross section ratio from our analysis with this resonance integral gives us a value of 0.238 ± 0.019 b for the thermal cross section.

Past measurements of the thermal cross section have considerable differences, and evaluated cross sections vary similarly. A summary of thermal cross section measurements and evaluations is shown in Fig. 3.14. Our result favors the Bresesti *et al.* [37] measurement (0.281 ± 0.028 b) over the Kondaiah *et al.* [38] measurement (0.130 ± 0.015 b). Most recent evaluations [39] give the thermal cross section as 0.26 b, consistent with our result, though JENDL-4.0 [40] is an exception, favoring the Kondaiah measurement and giving 0.13 b, quite inconsistent with our result and the Macklin measurement of the resonance integral.

The complete decay pattern from radiative neutron capture can only be obtained for light nuclei using detectors with very good energy resolution (typically Ge). More complex nuclei, such as ^{137}Xe have too many levels to obtain a perfect cascade model. Detectors with worse energy resolution but high granularity, such as DANCE, can still provide valuable information about the cascades when simulations are used to model the detector response and experimental spectra are compared with predicted models.

Fortunately, for purposes of modeling the cascades for use in neutrinoless double beta decay experiments such as EXO-200, it is not necessary to know the decay scheme with extremely high precision, and the approximation presented here is sufficient. The Prussin *et al.* measurement of thermal neutron capture already produced a capture cascade model with precisely measured energy levels. The measurement presented here features coincidence data

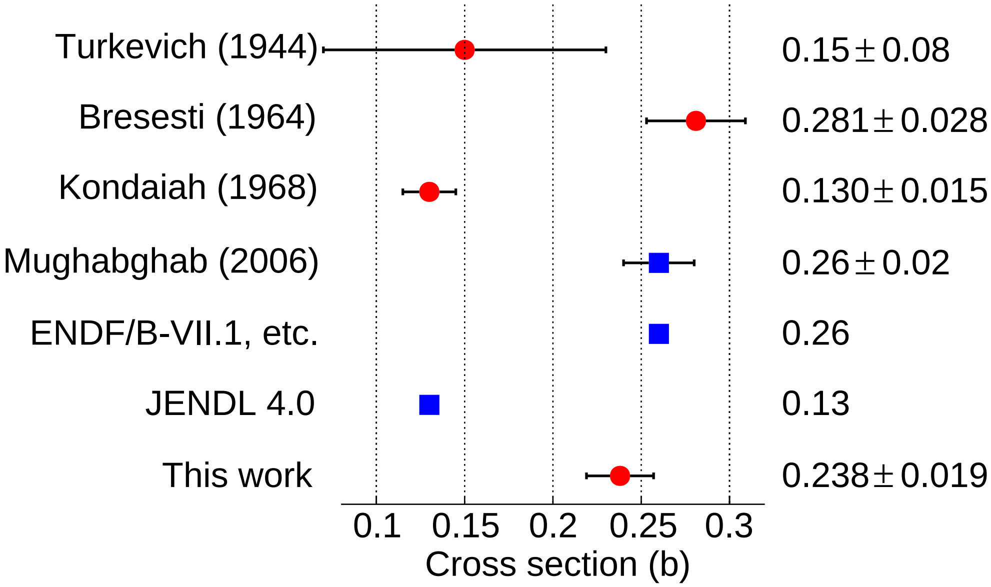

Figure 3.14: Comparison of various measurements and evaluations of the ^{136}Xe (n, γ) cross section for thermal neutrons. Each row corresponds to a measurement (red circle) or evaluation (blue square), and includes the cross section in both plot and text. All cross sections are in barns. Measurements by Macnamara et al. (1950) [41] and Eastwood et al. (1963) [42] are less precise and are not included here. Most modern evaluations, such as TENDL-2014 [43, 44] and JEFF-3.2 [45] have the same thermal neutron cross section as ENDF/B-VII.1 [35], so we do not list them separately. JENDL-4.0 [40] is an exception to this. Information on the Turkevich et al. measurement comes from Ref. [37, 46]. Other results listed come from Ref. [34, 37, 38].

not available in the previous measurement, and is used in conjunction with the old results to produce a more refined capture cascade model. The resonant capture model presented here is new.

This information can help guide future evaluations for cross sections on ^{136}Xe, which can allow for improved simulations of neutron transport in $0\nu\beta\beta$ experiments. Additionally, the updated capture cascade models can assist with mitigation of the ^{137}Xe beta decay background in $0\nu\beta\beta$ experiments, discussed more in Sec. 5.1.

Chapter 4

Inelastic neutron scattering γ-ray production in ^{136}Xe

4.1 Introduction

Neutron inelastic scattering events are a possible background for neutrinoless double beta decay. Measurement of $(n, xn\gamma)$ interactions on the isotope of interest can help identify potential backgrounds. Also, there is interest in using $(n, n\gamma)$ on ^{136}Xe as a potential calibration technique, discussed further in Sec. 5.3.

This chapter describes the inelastic scattering measurements taken at the GErmanium Array for Neutron Induced Excitations (GEANIE) at the Los Alamos Neutron Science Center on the WNR 60R flight path [47].

4.2 GEANIE

The GEANIE detector is comprised of 20 HPGe (High Purity Germanium) detectors arranged spherically around a central target point [48]. Fig. 4.1 shows the GEANIE array along with the GEANIE beamline from the spallation target. It is designed to measure $(n, xn\gamma)$ partial cross sections using neutron-induced γ rays. The Ge detectors have bismuth germanate (BGO) escape suppression shields. Both planar and coaxial geometries of Ge detector are used in the array, which have gains set to measure a maximum γ detection energy of 1 and 4 MeV respectively.

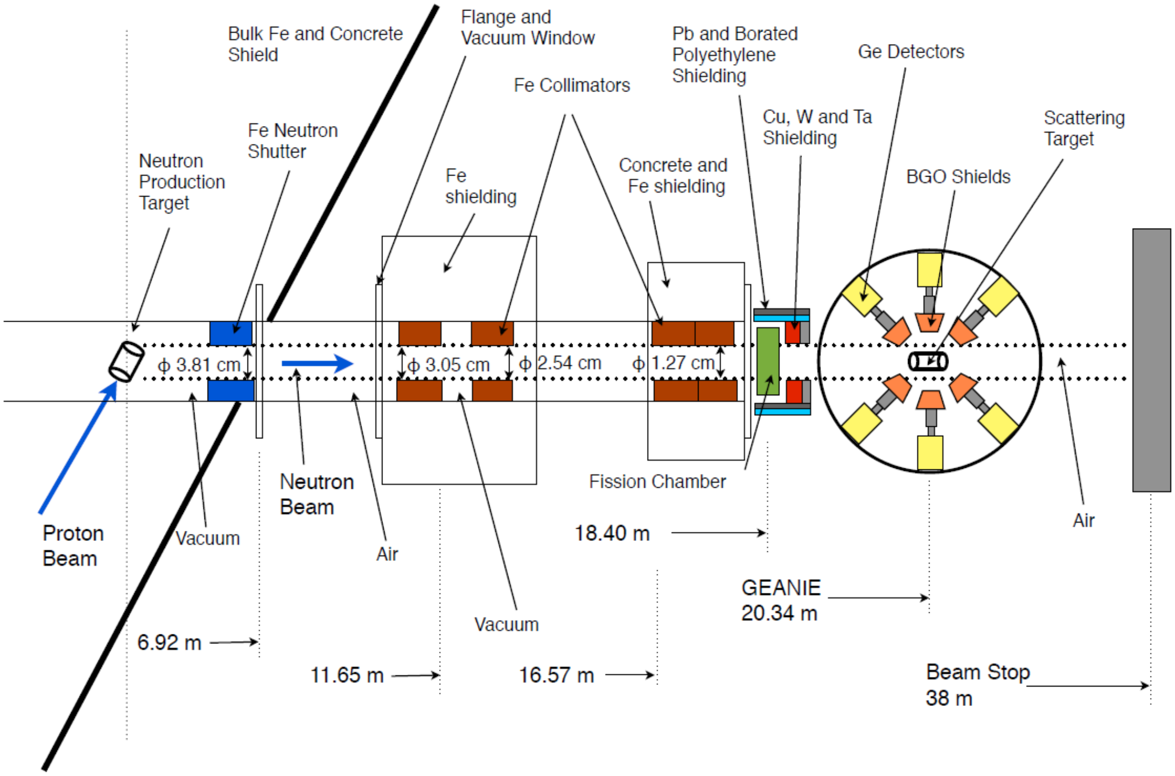

Figure 4.1: Schematic of the neutron beam line at GEANIE (not to scale). Figure from [49].

4.2.1 Neutron Beam

The neutron beam was produced by a pulsed 800 MeV proton beam on a tungsten spallation target. The resultant neutron beam had a broad spectrum of energies from about 0.2 - 800 MeV. The beam timing structure was composed of a series of small pulses (micropulses) within a 625 μs window, shown in Fig. 4.2. Each micropulse was less than 1 ns long and spaced 1.8 μs apart. This group of micropulses repeats every 16.7 ms and is collectively called a macropulse. The repetition rate of macropulses was 100 Hz during data taking for this measurement.

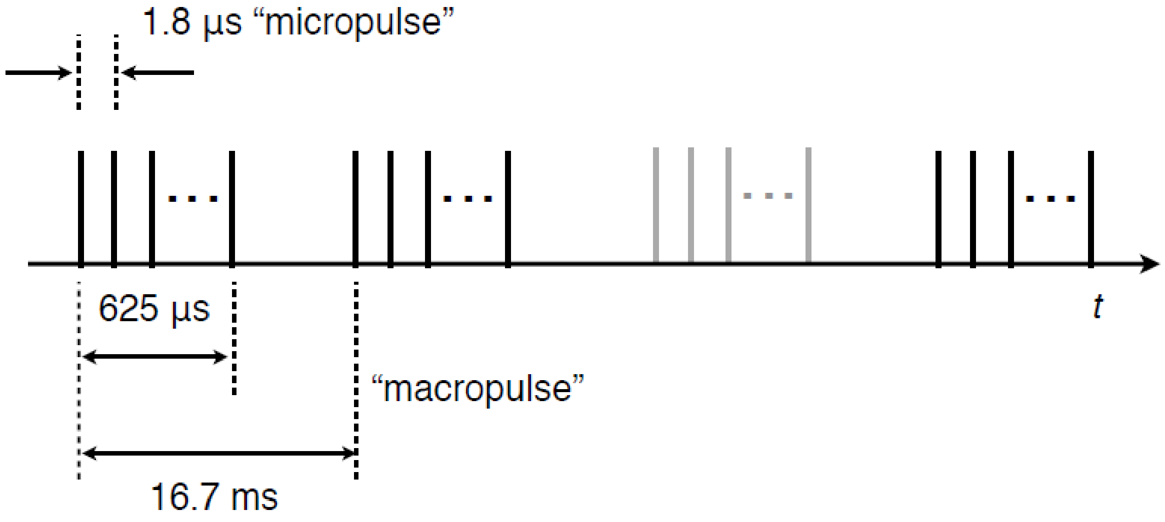

Figure 4.2: Beam structure at GEANIE. During data taking, one out of every 6 macropulses was sent to another beamline. Figure from [49].

4.2.2 Detector Array

The center of the GEANIE detector array is 20.34 m downstream from the spallation target, as illustrated in Fig. 4.1. The 20 detectors are located radially around the center of the array alternating between one in plane detector and two detectors 29°out of the plane, as in Fig. 4.3 and Fig. 4.8.

4.2.3 Fission Monitors

Upstream from the Ge detector array, a fission ionization chamber measures the neutron flux of the beam. Two thin foils made of ^{235}U and ^{238}U are housed in an ionization chamber 18.495 m downstream from the spallation target and intersect with the neutron beam. These foils are kept at high voltage during the running of the experiment. There is a small probability for each beam neutron to induce a fission event in the foil, wherein the charged fission fragments from ^{235}U(n,f) and ^{238}U(n,f) cause a signal on the foil that can be read out. Further details of this instrument can be found in Ref. [50].

An example output spectrum from the ^{235}U foil is shown in Fig. 4.4. The low energy

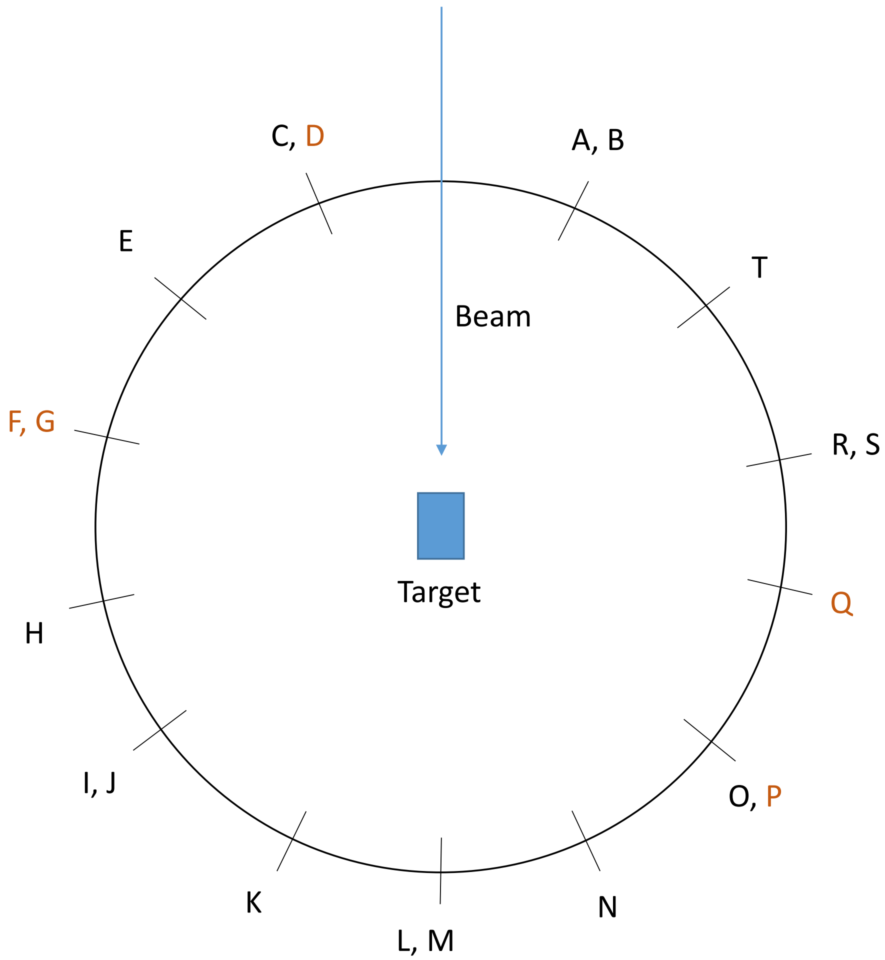

Figure 4.3: Schematic of the detector placements around the GEANIE array (not to scale). Every other radial position (about 30 degrees apart) switches between two detectors (both out of plane by 29°) and one detector in plane. The 5 detectors used for this analysis are D, F, G, P, and Q, shown in orange text on the diagram. See Sec. 4.6.1 for details of the detector selection.

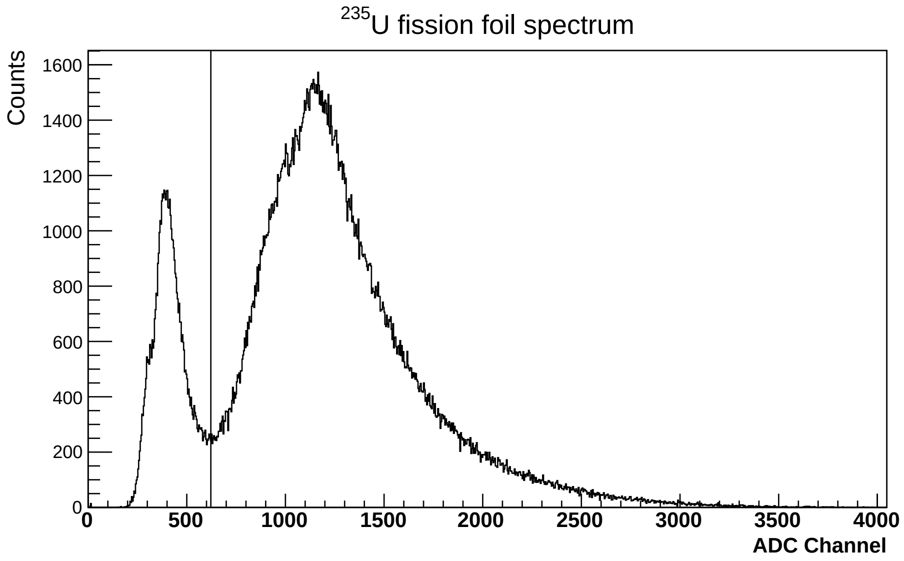

Figure 4.4: ADC counts from the ^{235}U detector. The low energy peak in the spectrum is caused by alpha events in the fission chamber. The counts from this peak are removed with a cut at the minimum in the valley between the peaks. The uncertainty in the placement of this cut has a negligible effect on the resultant neutron flux.

peak is due to α events in the fission chamber, while the high energy peak is due to fission fragments. A cut is placed on the flux spectra at the minimum between the alpha peak and the fission fragment peak to remove α events . The pulse-height of the fission fragment peak is proportional to the ionization energy deposited in the foil.

The fission cross sections are known well up to E_n of 200 MeV, as shown in Fig. 4.5, and are used to calculate the neutron flux of the beam. The resultant flux for both ^{235}U and ^{238}U foils is shown in Fig. 4.6. The fluxes for the two foils agree within uncertainties from about 1 MeV to 100 MeV. The fission cross section of ^{238}U below 1 MeV makes it difficult to get an accurate measurement. As such, the flux from ^{235}U is used below 4 MeV to determine the neutron flux, and the flux from ^{238}U is used up to 100 MeV. The flux data are processed with the same neutron energy binning as the Ge detector data for easy comparison.

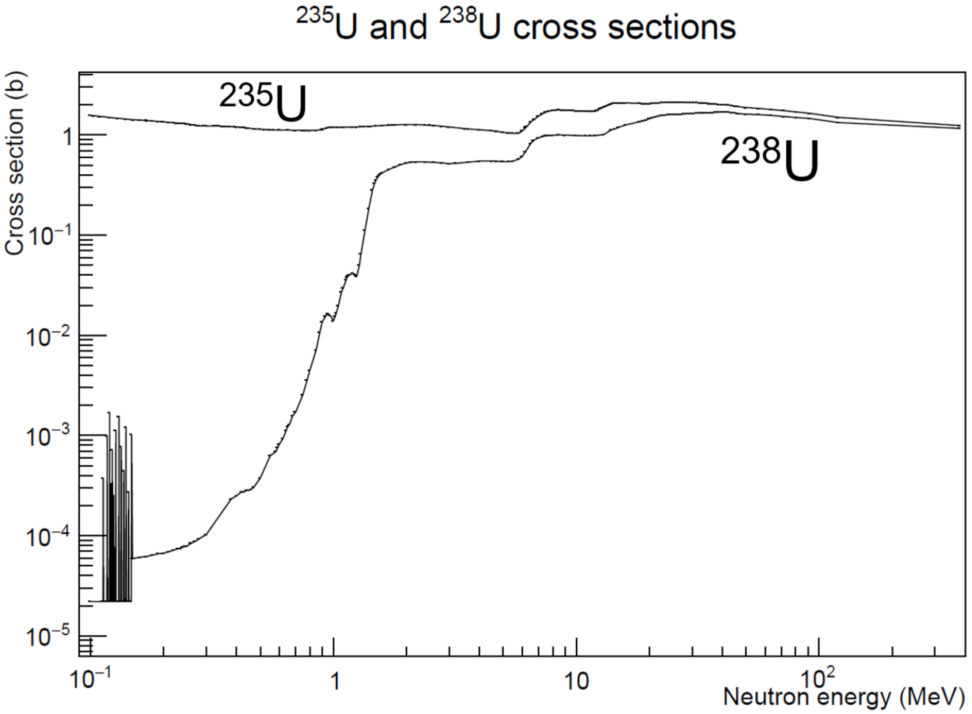

Figure 4.5: Fission cross sections for ^{235}U and ^{238}U. ^{235}U cross section is relatively constant across neutron energy, whereas the ^{238}U cross section drastically increases between 0.1 and 2 MeV. As such, ^{238}U monitor will not see extra events due to wrap-around (especially slow) neutrons.

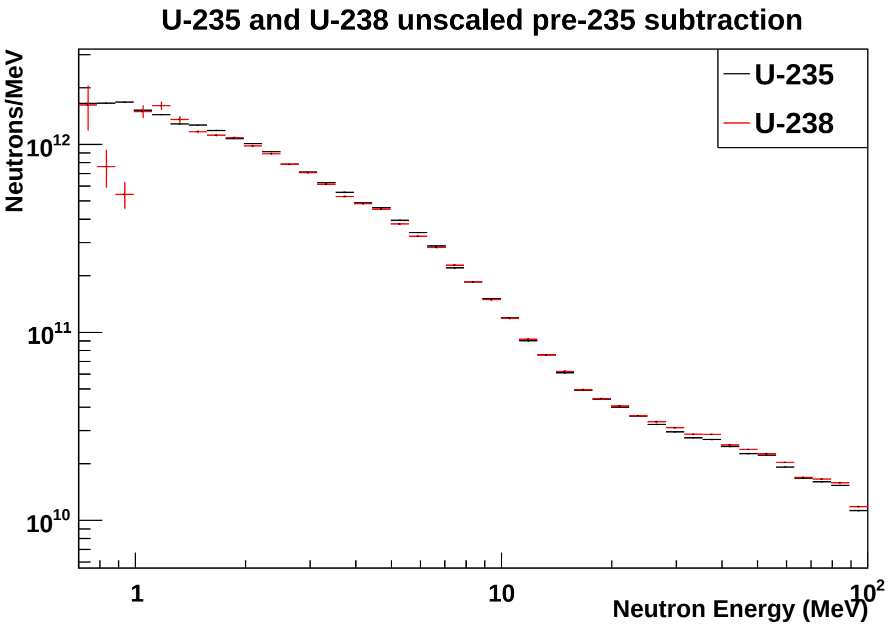

Figure 4.6: Flux measurement for entirety of the ^{136}Xe data run at GEANIE. The U-235 and U-238 spectra agree quite well, except for a low neutron energy points on the U-238 spectra.

4.3 Data Taking Overview

An aluminum target with kapton windows, pictured in Fig. 4.7, was placed at the center of GEANIE. Data were taken with the target evacuated, the target pressurized with xenon, the target pressurized with nitrogen, iron foils placed on each end of the target, and radioactive sources placed at the center of the detector. The datasets with the evacuated target and target pressurized with nitrogen served as a way to identify backgrounds. The xenon dataset was used for cross section analysis. Finally, the iron dataset was used in order to normalize absolute xenon cross sections using the primary 847 keV transition in ^{56}Fe.

4.3.1 Pressure of the ^{136}Xe Vessel

The xenon vessel was pressurized to approximately 2750 torr absolute with greater than 99.9% pure ^{136}Xe. Pressure measurements were made continuously using an MKS Baratron Type 627D pressure gauge and recorded electronically. There was a small, but consistent

Figure 4.7: Gas target vessel used during the ^{136}Xe run at GEANIE. The target was composed of an Al body, with two Al screw down end caps and kapton windows. The connection to the target manifold is an NPT to Swagelok connector with a viton o-ring on the NPT side.

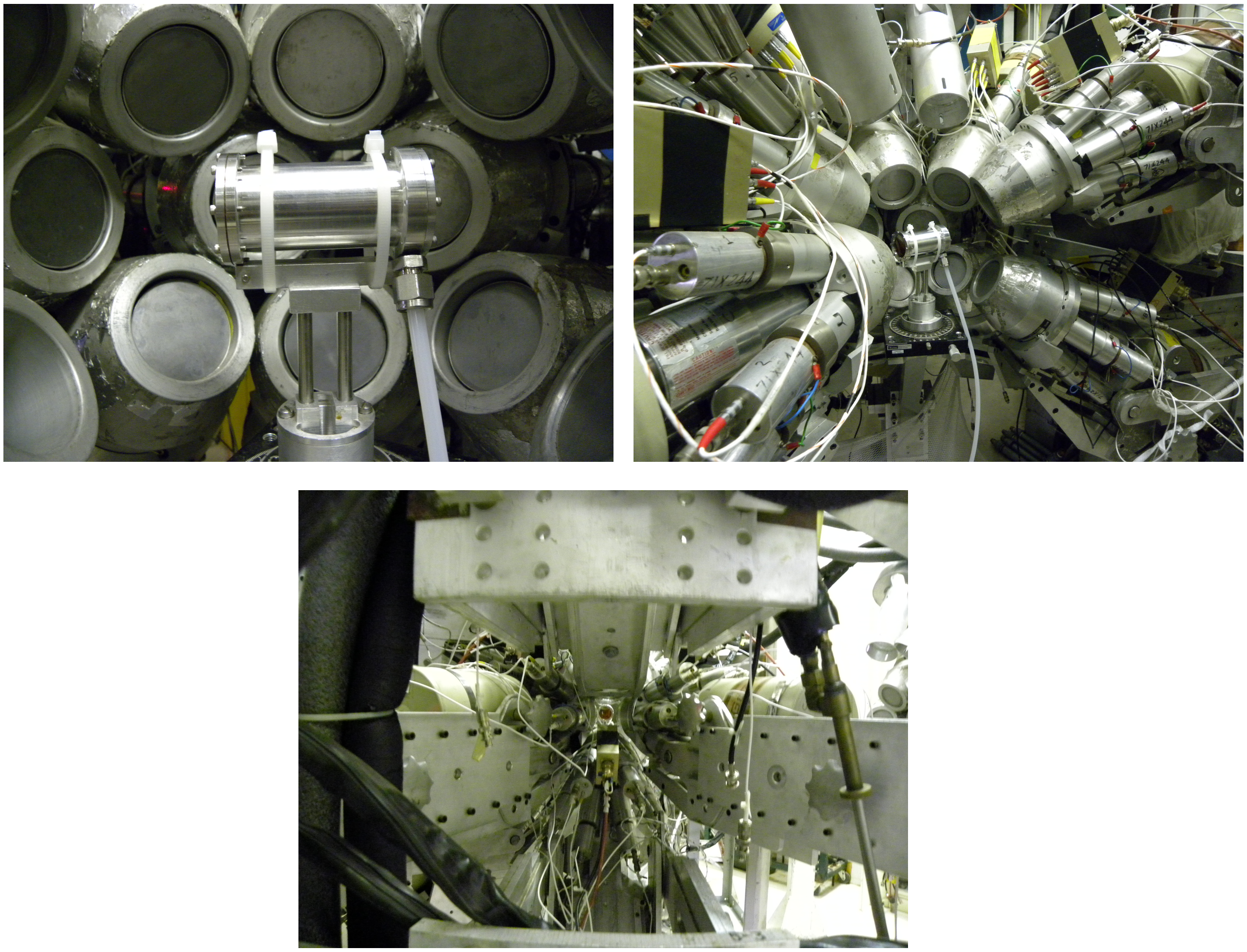

Figure 4.8: The aluminum gas target cell installed at GEANIE. The top two photos show the GEANIE array with half of the detectors pulled away in order to access the target. The bottom photo shows a view down the beamline toward the target. The upper left photo shows the pattern of detector placement discussed in Sec. 4.2.2.

leak in the target for the duration of the data period. The exact location of the leak was not found, so it is not clear how the design could be improved. Fig. 4.9 shows the measured pressure of the xenon. Three periods are marked with a green line on Fig. 4.9: xenon only, xenon+iron, and another xenon only dataset.

Linear fits were made to each dataset separately. There are two periods of missing baratron data. The first is an overnight period from 12/10/2014 to 12/11/2014, where a software update shut down the data taking computer. The second is at the end of the xenon period during 12/15. It is not known why this period is missing baratron data.

4.4 Germanium Detector Energy Calibration

In order to calibrate energy and measure efficiency, data were taken with several radioactive sources (^{60}Co, ^{57}Co, ^{54}Mn, ^{137}Cs, ^{152}Eu, ^{22}Na, ^{133}Ba, and ^{109}Cd) placed at the center of the array. The ^{152}Eu source was used for the efficiency measurement, and the lines used spanned the energy range of 245 keV to 1299 keV. The ADC spectra for each of these source runs are used to determine the corresponding γ energy for each detector.

The known peak energies of each radioactive source are fit with a Gaussian plus a linear background function as shown in Fig. 4.10. The center of that Gaussian function is plotted on a γ energy vs. ADC channel plot for each source and each detector. Fig. 4.11 shows the result for a single detector. The γ energy vs. ADC channel plot is fit with a quadratic function in order to determine a smooth calibration function for that detector.

For a more accurate calibration at high γ energy, two lines from ^{136}Xe, 2290 keV and 2415 keV, are also used for calibration. Despite the fact that these lines are not high activity radioactive sources, these were sufficient for calibrating the detectors above 2 MeV.

4.5 Time-of-Flight Analysis

Alongside calibrating the γ energy of the Ge detectors, the neutron energy of events is calculated with a time-of-flight method. By measuring the time that the neutrons take to

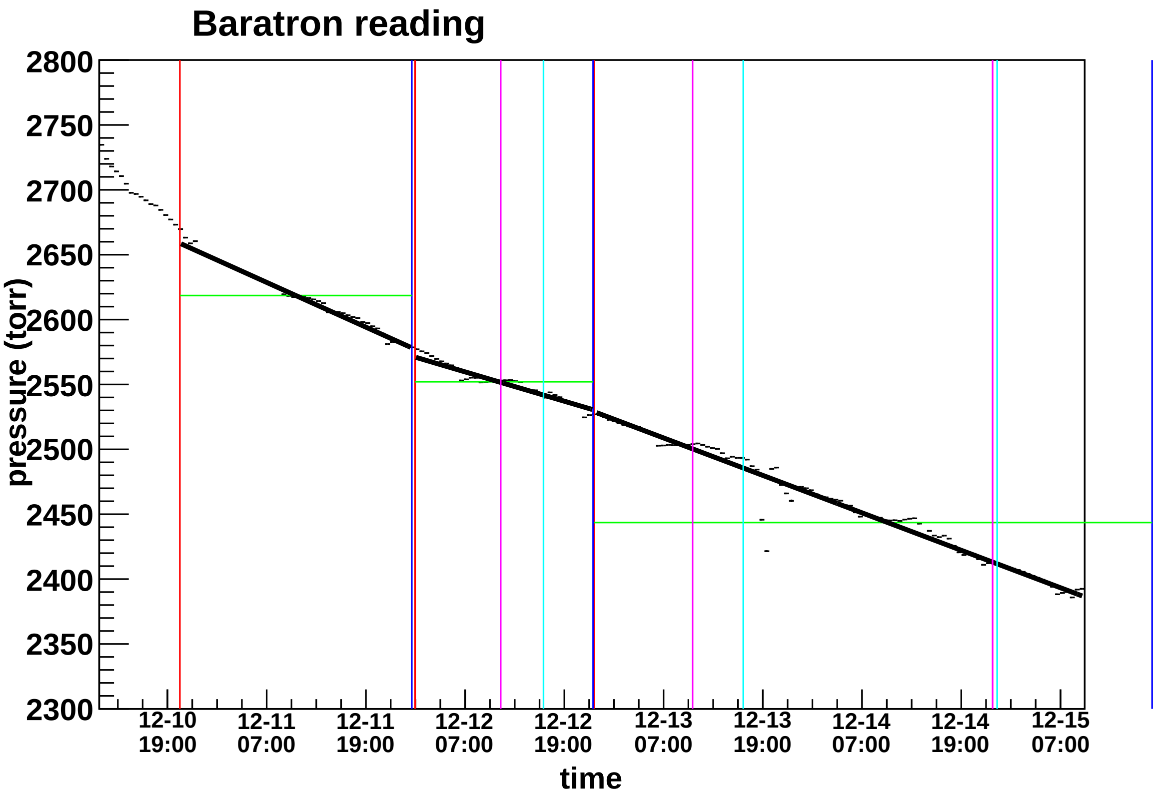

Figure 4.9: ^{136}Xe absolute pressure during data taking. The data is split up into three separate time periods (denoted by red start line and blue end line). These time periods are the first xenon only period, the xenon+iron period, and the second xenon only period. The magenta and teal lines are periods that are cut because of a lack of data during those time periods (beam was down, DAQ problems). The green lines are the average pressure during those periods after cuts. There are two periods of missing data which are assumed to follow the trend of nearby data. Over the course of data taking, the pressure dropped from approximately 2650 to 2350 Torr, due to a small leak in the target.

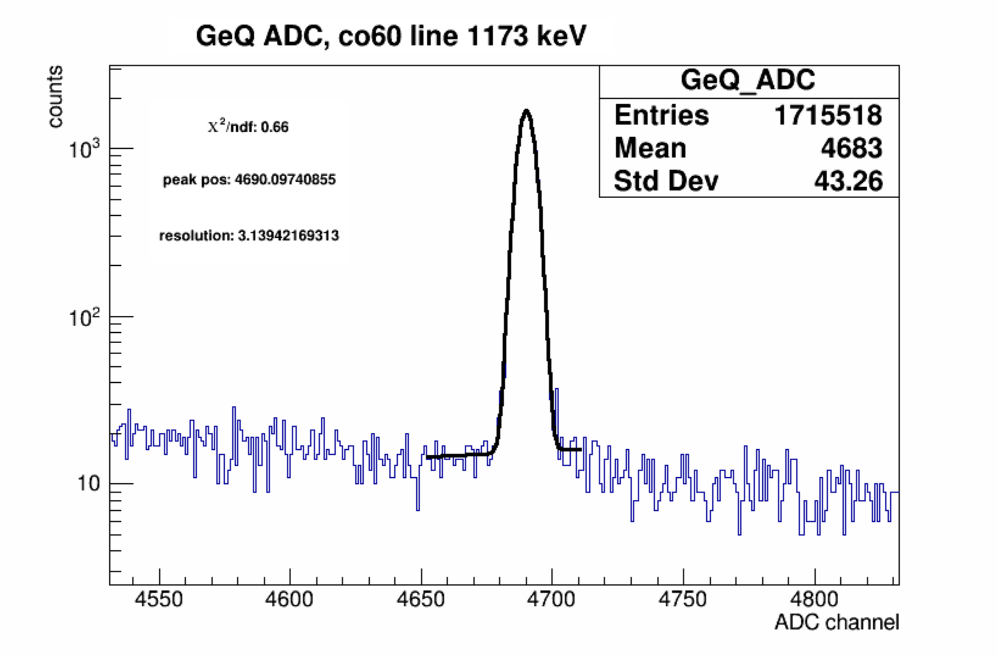

Figure 4.10: Fit to Co-60 1173 keV line. The fit is performed with a Gaussian+line to match the peak and background. This fit is just one example of the radioactive source fits used to calibrate the Ge detectors.

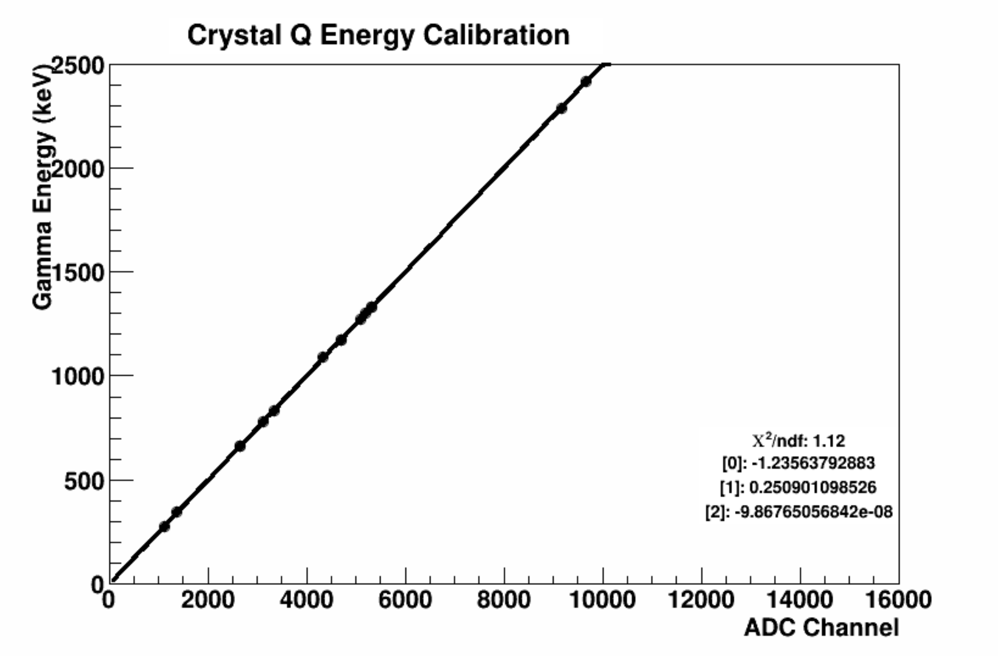

Figure 4.11: Calibration fit shown for detector Q. A separate fit is performed for each detector in the array using lines from ^{60}Co, ^{57}Co, ^{54}Mn, ^{137}Cs, ^{152}Eu, ^{22}Na, ^{133}Ba, and ^{109}Cd. Two high energy lines above 2 MeV from ^{136}Xe are also used to correct the calibration at higher energies. The error bars on the data points are too small to see on this scale.

reach the center of the GEANIE array, the kinetic energy of the neutrons can be determined.

Timing spectra were measured using FTDC (fast time-to-digital converters) and STDC (slow time-to-digital converters) signals. In general, there can be multiple FTDC signals per event, with the STDC signal used to determine which FTDC signal corresponds with the ADC signal read out. However, STDC signals were not used in this analysis; they would allow for including multiple events per micropulse. Instead, only events with a single FTDC read out per event were used for this analysis.

A typical FTDC spectrum is shown in Fig. 4.12. A larger FTDC channel number corresponds to an earlier time with respect to the beam structure. These spectra are composed of an initial self-triggered micropulse and several micropulses after the inital one. Data is taken for several micropulses after the initial trigger.

Each micropulse has an initial gamma flash due to bremsstrahlung in the spallation target. The initial gamma flash on the self-triggered micropulse is fit with a Gaussian to determine the FTDC channel of the gamma flash. The timing difference between the initial gamma flash FTDC channel and the FTDC channel corresponding to an ADC count is used to calculate the neutron energy for that event. The spacing between micropulses, 1.788 μs, is known precisely, as this spacing is created by the initial pulsing of the proton beam.

The FTDC spectra for each micropulse were stacked via gamma-flash timing to create Fig. 4.13. In this case, the center of the initial gamma flash peak is split between the left and right sides of the plot. There are some structures on this plot, such as the peak around channel 800, which are not understood. However, these do not affect the time-of-flight calculation.

A neutron energy is calculated for each event using:

$$\delta t = \frac{d}{c}\left[\sqrt{\frac{m_n}{2E_n}} - 1\right] \tag{4.1}$$

where δt is the time since initial gamma flash, d is the distance, 20.34 m, to the center of the

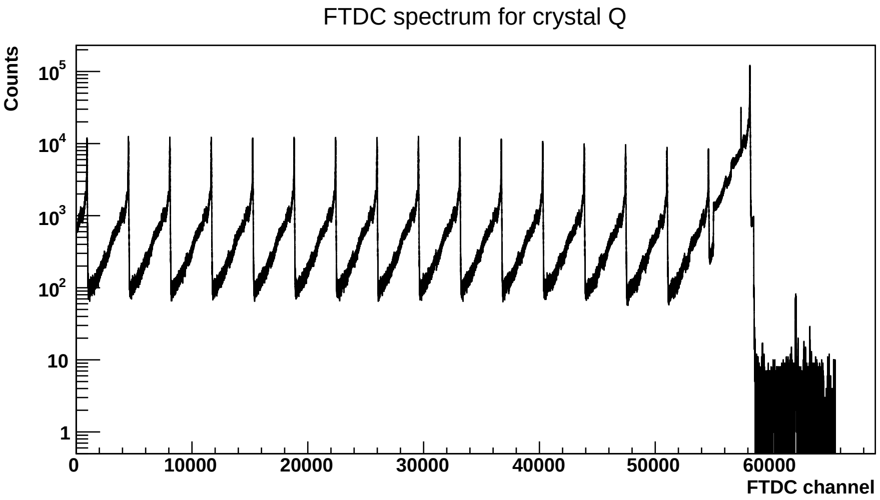

Figure 4.12: FTDC spectrum for detector Q. The series of peaks show micropulses, spaced 1.788 μs apart. The peaks are due to gamma flashes in the beam, which are used to signal the initial time for the neutron time-of-flight calculation. A higher channel number equates to earlier time due to readout of the channels.

GEANIE array, m_n is the mass of the neutron, and E_n is the neutron energy. On Fig. 4.13, 1 MeV neutrons correspond to FTDC channel 2812 and 100 MeV neutrons correspond to FTDC channel 158.

The FTDC timing information were calculated for each detector separately. After calculating both the γ energy calibration function and the FTDC timing for each detector, the data are reprocessed in order to determine the γ energy and neutron energy for each event.

4.6 Gamma ray production cross sections

The measurement of $(n, xn\gamma)$ cross sections for each neutron energy was calculated using:

$$\sigma_{\gamma,\mathrm{Xe}}(E_n) = \sum_i \left[N_i \beta_i \frac{I_{\gamma,i}(E_n)}{I_\Phi(E_n)} \frac{T_\Phi}{T_{\gamma,i}} \frac{1}{t_{\mathrm{Xe}} \epsilon_{\gamma,i,\mathrm{Xe}} A_i} \right] \tag{4.2}$$

with the sum over each detector i used in the analysis, N_i is the iron normalization factor (Sec. 4.6.7), β_i is the angular effect minimization factor (Sec. 4.6.6), $I_{\gamma,i}(E_n)$ is the γ-ray

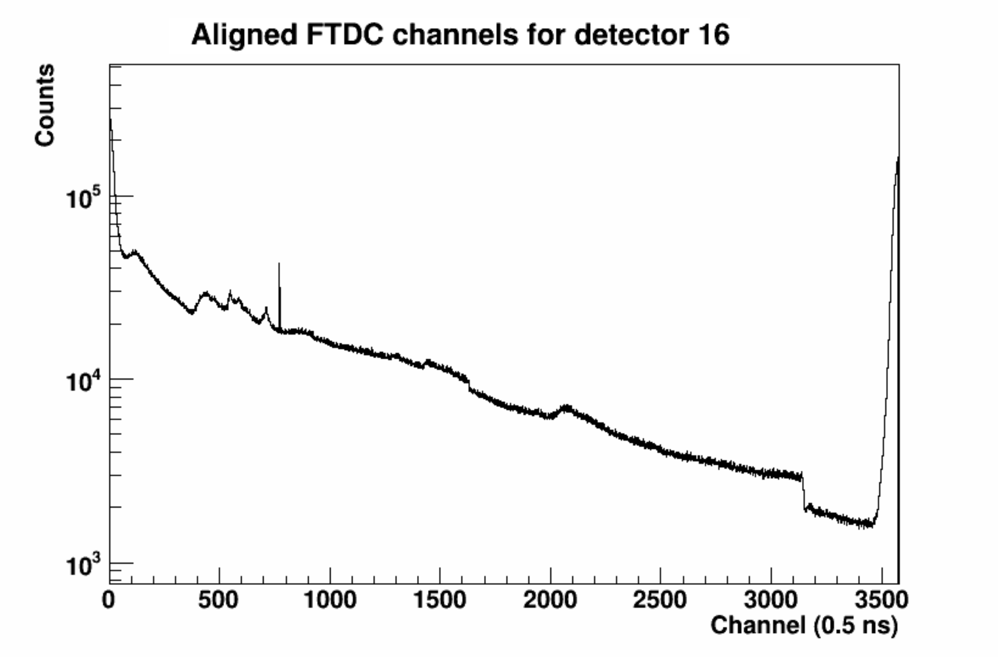

Figure 4.13: After aligning the gamma flashes in the FTDC and adding the micropulses, the time of flight spectrum is calculated for each detector. Shown here is detector Q, which is used in the final cross section analysis. The centroid of the gamma flash is used as the t = 0 for the time of flight calculation.

yield per MeV from the Ge detectors (Sec. 4.6.4), $I_\Phi(E_n)$ is the number of neutrons per MeV (Sec. 4.2.3), $T_{\gamma,i}$ and T_Φ are the Ge detector and the fission chamber livetimes respectively (Sec. 4.6.2), t_{Xe} is the areal density of ^{136}Xe (Sec. 4.3.1), $\epsilon_{\gamma,i,\text{Xe}}$ is the Ge detector efficiency (Sec. 4.6.5), and A_i is the attenuation factor (Sec. 4.6.3).

Fig. 4.14 shows the level diagram for ^{136}Xe. The lines measured in this analysis are shown in black.

4.6.1 Detector Selection

Before any cross section measurements were calculated, an effort was made to determine the characteristics of individual detectors. It was clear that the data from some detectors were unusable because they lack timing or ADC information. Other detectors were cut due to problems with timing and the gamma spectral shape, or finally because of an inability to

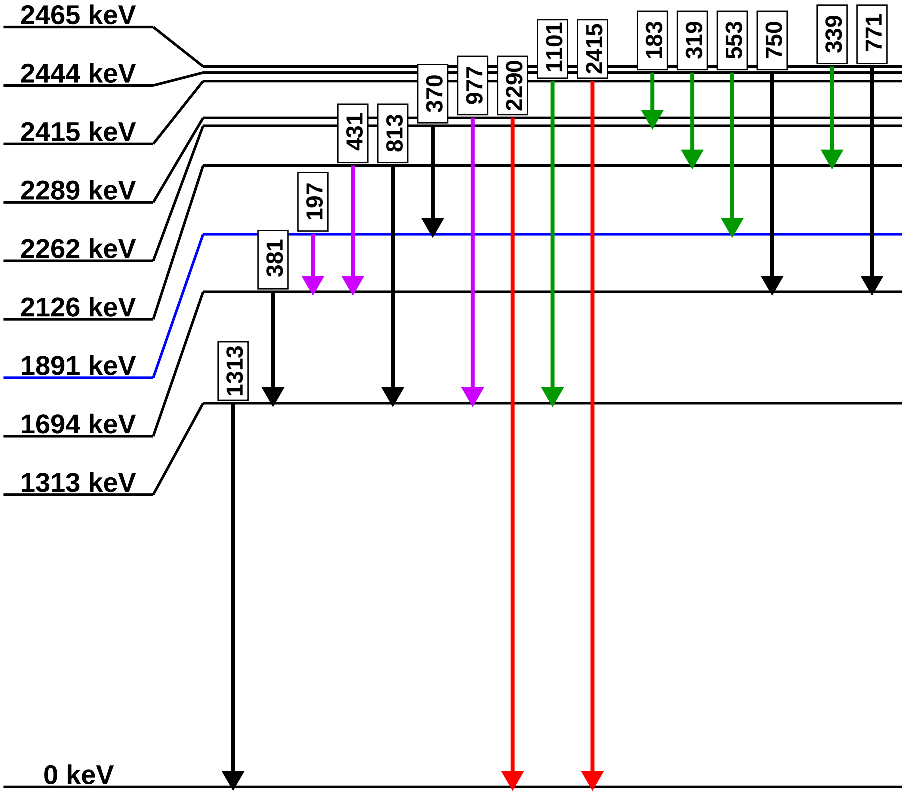

Figure 4.14: Level diagram for ^{136}Xe. The black lines are measured in this analysis. The green lines are too rare to show up in the data. Purple lines are seen in the data, but unable to be measured with significance. Red lines are measured, but with significant uncertainties due to efficiency and angular effects.

get a good efficiency fit using source data. The resultant five detectors after all these cuts were D, F, G, P, and Q (see Fig. 4.3).

4.6.2 Detector Livetimes

The detector livetime is a measurement of how often the DAQ is able to record signals from the detector over some period of time. Deadtime is caused by the conversion of ADC signals to digital signals and other losses in the electronics. Scaler signals which have effectively no deadtime record how many total signals are sent from the detector to the DAQ. Comparing the number of total signals to the DAQ with the number of recorded ADC's for any given detector and dataset shows the percentage of signals unable to be recorded.

A file with histograms and scaler information is written out by the data aqcuisition (DAQ) computer for each run. The scalers written out included accumulated values for the whole run, along with rates as a function of run time. For the livetime calculation, the first set of suppressed Ge scalers, corresponding to beam-on data, in the accumulated hard scalers histogram were used in conjunction with the ADC beam-on histograms written in the same file. The ratio of the integrated ADC counts to the accumulated scalers, the livetime for that detector, were recorded for each detector and run. Livetimes are shown in Fig. 4.15.

4.6.3 Attenuation correction factor

An attenuation correction factor, A_i, was calculated using MCNP [51]. This attenuation factor accounts for γ-rays passing through materials like aluminum from the target and the xenon itself. In general, A_i is a function of γ energy, and was calculated as such in this simulation. This correction is less than 3% for all detectors and γ lines measured in this analysis.

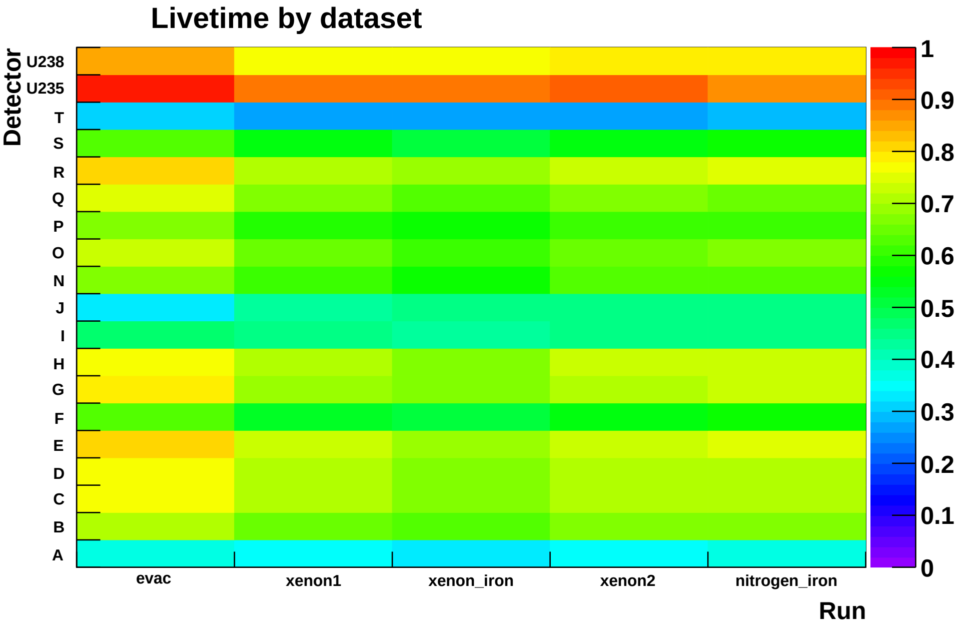

Figure 4.15: This histogram shows average livetime as a function of detector and dataset. The livetime of the fission monitors was quite a bit higher than the Ge detectors. As the rate of ADC signals increases, livetime decreases. The Xenon+iron dataset shows the lowest livetime, due to the higher interaction rate at the target and higher production of γ-rays.

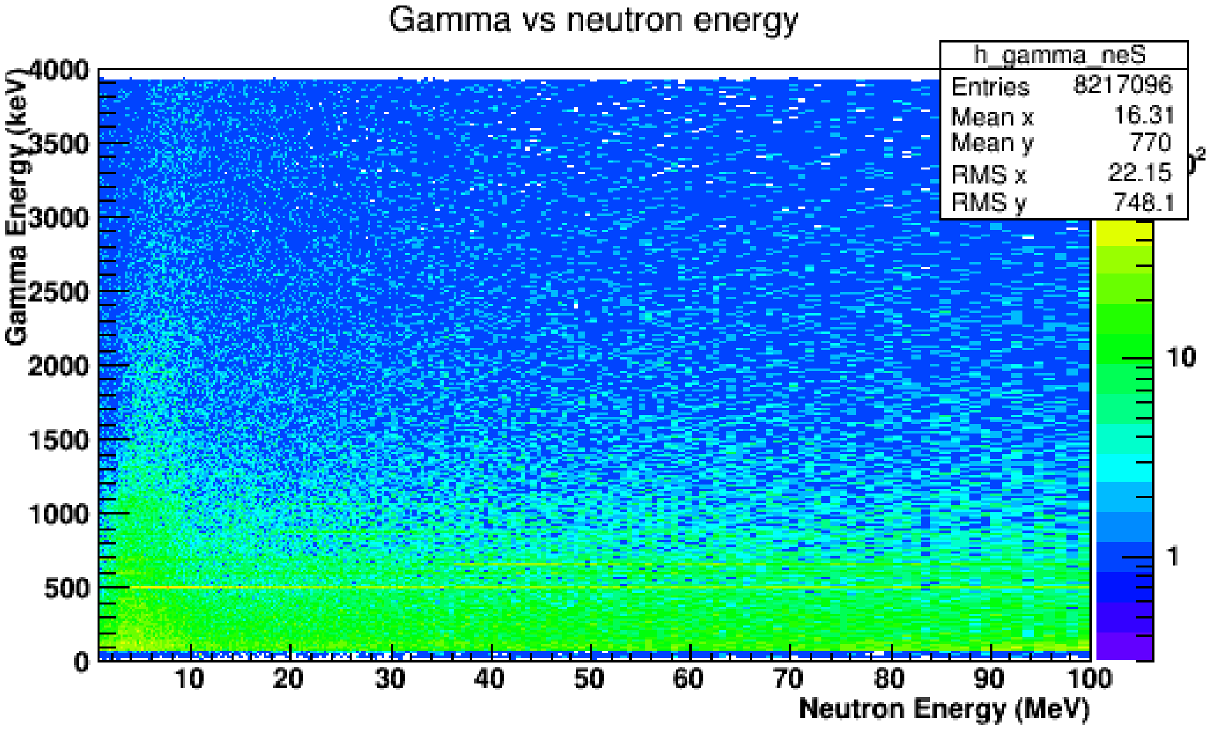

Figure 4.16: Using calibration and time of flight information for each detector, a 2-dimensional histogram of gamma vs. neutron energy is filled for each event in the dataset. This histogram is a useful construct, as it allows cutting on interesting gamma energies and plotting as a function of neutron energy.

4.6.4 Gamma Yield Method

The γ yield, $I_{\gamma,i}(E_n)$, is the measured number of gammas for a given transition. After the data have been calibrated in both neutron energy and γ energy, they are plotted as a 2-dimensional histogram, an example of which is shown in Fig. 4.16. This is a useful histogram because the data can be projected to either axis for further analysis. The gamma energy binning is 1 bin per keV, while the neutron energy binning is equal logarithmic bins.

An example of the gamma spectra in multiple neutron energy windows is shown in Fig. 4.17.

In order to measure the γ yield, each neutron energy bin is projected to the γ-energy axis. An example of one of these projections is shown in Fig. 4.18. This example is for

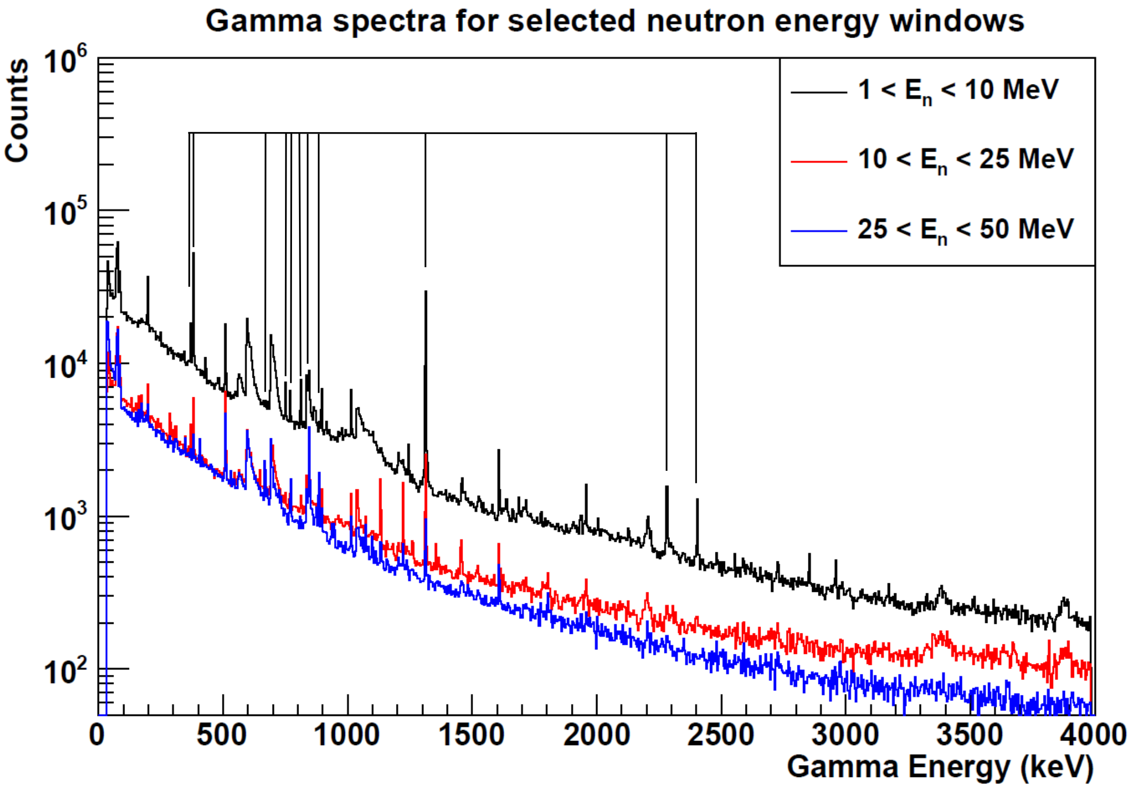

Figure 4.17: ^{136}Xe spectrum for detector Q at various neutron energy windows. The lines that are measured in this analysis are marked on the plot.

the 847 keV transition in ^{56}Fe, discussed more in Sec. 4.6.7. A simple fit of a Gaussian for the peak and a line for the background is done for each neutron energy bin. The linear background was fit in a 30 keV range centered on the peak. Then, the γ yield is calculated by integrating bins around the peak and subtracting the linear background evaluated at the center of each of those bins. The range of integration is chosen based on the resolution of the peak, intended to encompass the majority of the counts in the peak. The chosen integration range was 3.5 σ on each side of the peak. These fits are done for each neutron energy bin, detector, and gamma line measured in this analysis. Despite the wide array of γ intensities and background counts in the data, this simple fitting method proved very robust. In the few cases where this method did fail, fits were automatically thrown out based on unphysical resolutions or unreasonable χ^2 values.

4.6.5 Efficiency Determination

The efficiency of the Ge detectors is the ratio of the number of counts recorded by the detector to the number of γ-rays emitted by the source. After an initial low energy γ-energy threshold, efficiency in Ge detectors falls off as γ energy increases.

The ^{152}Eu source was used to determine the efficiency for each detector. ^{152}Eu has many lines that are useful for giving an overall shape to the efficiency curve. While lines from many sources could have been used in this measurement,these sources would have introduced uncertainties because of the relative source activities. The ^{152}Eu source had enough lines to adequately cover the shape of the efficiency curve, up to 1.4 MeV. Efficiency points were fit with the high energy portion (above 100 keV) functional form from a package called RadWare [52].

Understanding the shape of the efficiency curve is all that matters for this particular analysis, as the absolute scale of the efficiency is unimportant due to the iron normalization being applied, Sec. 4.6.7. Despite the absolute scale being unimportant for the cross section measurement, the activity of the ^{152}Eu source was used in the efficiency measurement.

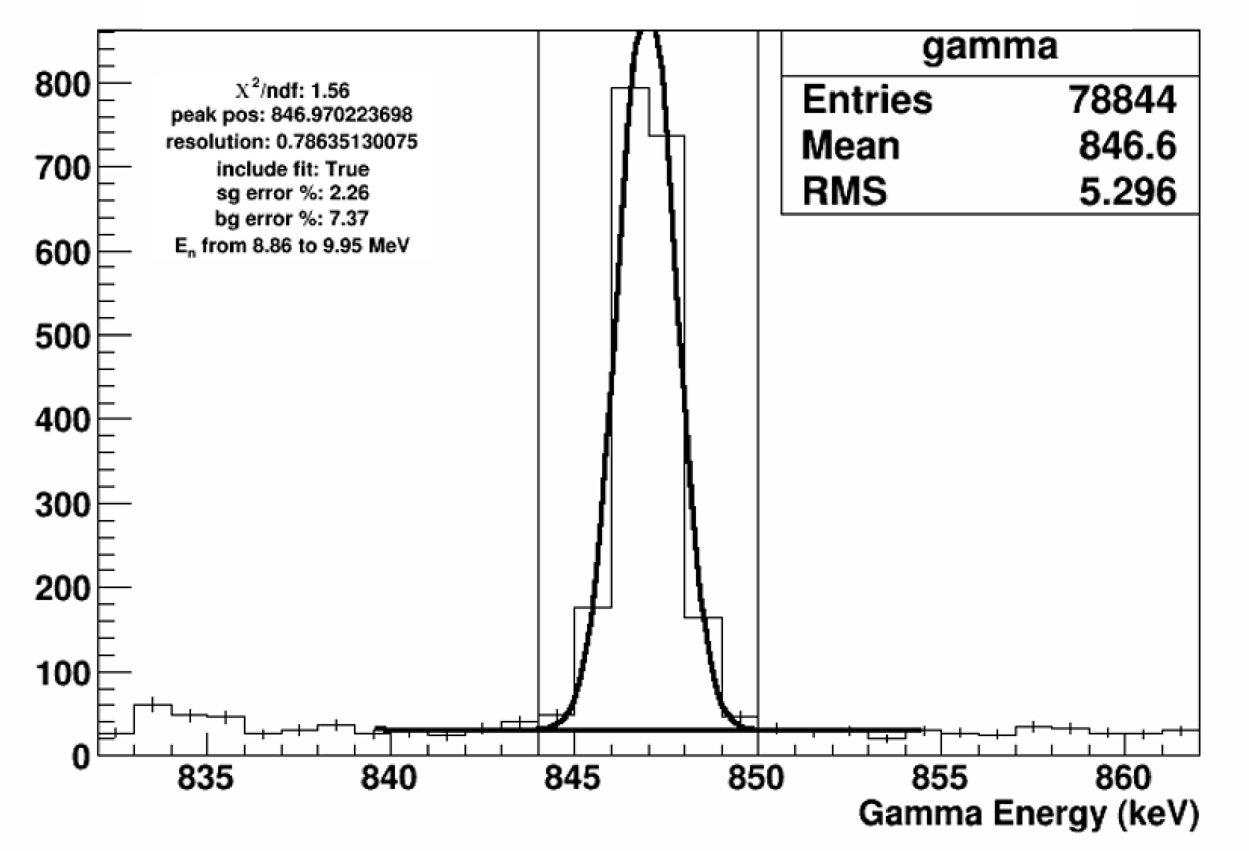

Figure 4.18: Example gamma yield fit for one neutron energy bin using the iron data. The photopeak was modeled with a Gaussian for the peak plus a line for the background. The gamma yield is the data counts in the energy window minus the linear fit to the background. The thin lines surrounding the gaussian fit are the integration range for the peak.

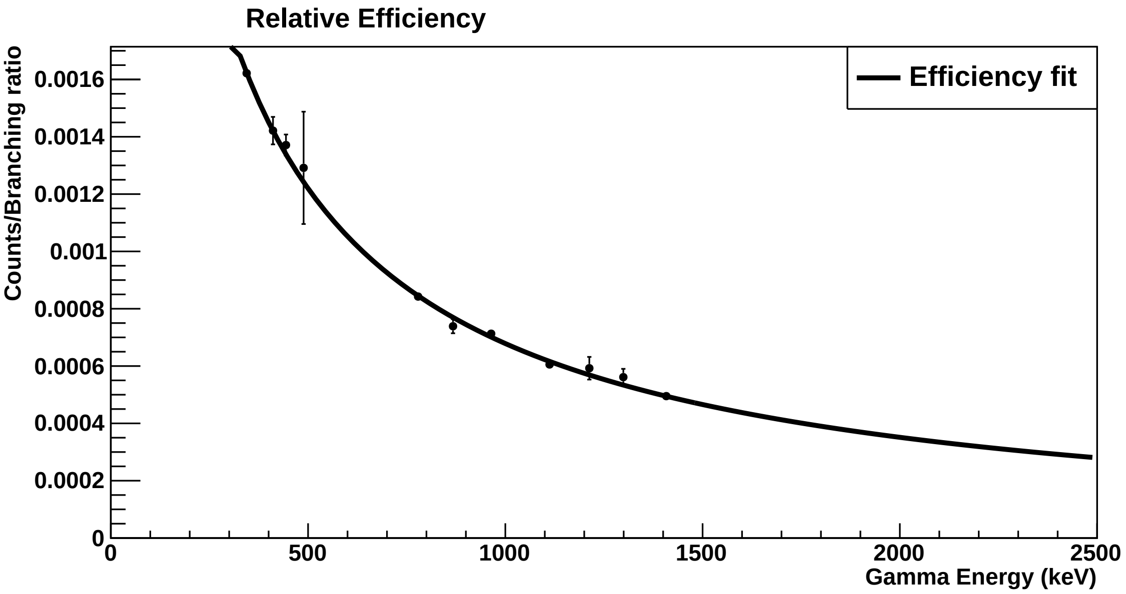

Figure 4.19: Absolute efficiency curve for detector G.

The uncertainty on the efficiency above 2 MeV increases significantly, as there were no sources available with lines above 1.4 MeV during data taking. This will be discussed later in Sec. 4.6.8. The efficiency is determined by

$$\epsilon_\gamma = \frac{N_{peak}}{BR \times \text{activity} \times \text{runtime}}, \tag{4.3}$$

where ϵ_γ is the γ efficiency, N_{peak} is the number of γ-rays measured in the peak, BR is the branching ratio of that particular line, activity is the activity of the source, and runtime is the time that the detectors were taking data.

4.6.6 Angular Anisotropy

In general, neutron-induced nuclear γ-ray emission is not an isotropic process. These angular corrections have been shown to be small, around 5%, for ^{238}U [47]. However, it is not clear whether these results are directly applicable to this ^{136}Xe measurement. The angular distribution $W(\theta)$, and subsequent correction, C_γ, can be represented by:

$$W(\theta) = \sum_{k=even} A_k P_k(cos(\theta)) \tag{4.4}$$

and

$$C_{\gamma,i}(E_n) = \frac{1}{W(\theta_i, E_n)} \tag{4.5}$$

where P_k are Legendre polynomials and A_k are coefficients related to the angular anisotropy. See [53] for more details.

Instead of relying on past analyses for this correction, a method was developed to minimize this angular effect for this measurement. Assuming a small correction and three unique detector angles, the angular corrections reduce down to a system of linear equations where the second-order Legendre polynomial is canceled out. The three unique detector angles used were detectors D at 157.9°, F at 102.0°, G at 102.5°, P at -51.0°, and Q at -76.9°. $W(\theta)$ is symmetric about both $\theta = 0$ and $\theta = 90°$, so F, G, and Q were averaged to an angle of 102.5°. By weighting the results of these detectors based on their angle, the angular effects were minimized.

This method could only be used to measure cross sections up to 2 MeV, as detector D was run in a configuration with a maximum measured γ energy of 2 MeV. Without a third unique detector angle, the system of equations will have no solution which cancels out the angular effects. Relying on differences between detectors at very similar angles to each other for cancelation would amplify errors considerably. See Sec. 4.6.8 for more details on the uncertainties related to this method.

4.6.7 Iron Normalization

In order to measure absolute cross sections for the ^{136}Xe γ lines analyzed here, a normalization was applied based on a known cross section from the most prominent transition in ^{56}Fe at 847 keV. Data were taken with two thin iron foils fixed to either side of the target cylinder. This normalization is applied in Eq. 4.2 as N_i. A normalization factor is applied for each detector based on the measured iron cross section for that detector.

The known cross section used is taken from [54] at 6.2 MeV neutron energy with a cross section of 1.5±0.1 b. The normalization was made at 6.2 MeV because the cross section is flat in that region, minimizing any binning effects from this method.

The normalization factor is calculated as:

$$N_i = \frac{\sigma_{\gamma,\text{known,Fe}} C_{\text{known}}}{\sigma_{\gamma,i,\text{meas.,Fe}}} \tag{4.6}$$

where $\sigma_{\gamma,\text{known,Fe}}$ is the 1.5 b cross section discussed above, C_{known} is an angular correction to this published result, and $\sigma_{\gamma,i,\text{meas.,Fe}}$ is the cross section measured with this analysis before any normalization is applied. The measurement of the ^{56}Fe cross section here is a slightly modified version of Eq. 4.2:

$$\sigma_{\gamma,i,\text{meas.,Fe}} = \frac{I_{\gamma,i}(E_n)}{I_\Phi(E_n)} \frac{T_\Phi}{T_{\gamma,i}} \frac{C_{\gamma,i}}{t_{\text{Fe}} \epsilon_{\gamma,i,\text{Fe}} A_i} \tag{4.7}$$

Since a normalization factor is calculated for each detector, i, this result is not summed over all detectors. Also, the angular effect minimization factor β_i is not applied. Instead, these data are directly corrected for their angular effects with $C_{\gamma,i}$, discussed below. The areal density of the iron, t_{Fe} is used in place of the ^{136}Xe areal density. Finally, the efficiency of iron, $\epsilon_{\gamma,i,\text{Fe}}$, is not exactly the same as the efficiency used for ^{136}Xe measurements, also described in more detail below.

An extra angular correction factor, C_{known}, is applied here because the cross section result used for normalization is not corrected for anisotropy, though angular effects are discussed in the paper [54]. Results were taken from [55] which directly measured the first and second order angular coefficients, A_k from Eq. 4.4. A_2 and A_4 were taken at the same normalization point of 6.2 MeV using the HPGe dataset. These data can be used to calculate $W(\theta)$ for this particular transition at any detector angle. The normalization cross section from

Beyer was measured at 125° with respect to the beam. This angle is chosen to minimize the angular effects of anisotropy on the cross section result. However, the A_4 term is not canceled out by choosing this angle, so a very small correction of 0.995, C_{known}, was applied to the normalization cross section from the Beyer paper.

The A_2 and A_4 from [55] were also used to correct each detector's result for the 847 keV ^{56}Fe transition. Since the GEANIE detectors used are not at 125°, the correction is larger than C_{known}. This correction, $C_{\gamma,i}$, was calculated with Eq. 4.5. The largest correction applied was 0.91 to detector D, with the other corrections being smaller.

The efficiency for γ's originating in the iron, $\epsilon_{\gamma,i,\mathrm{Fe}}$, is not exactly the same as the efficiency for γ's originating in the xenon, $\epsilon_{\gamma,i,\mathrm{Xe}}$. The iron foils were fixed to both ends of the xenon target, which are slightly closer to some of the detectors than the xenon at the center of the array. A purely geometric simulation was run to test the difference between these two efficiencies. It was found that this correction ranged from 1 to 11% for the 5 detectors used in this analysis.

After applying these corrections along with the normalization factor, the iron cross section results agree quite well for all detectors in Fig. 4.20. All detectors agree within errors, though detector G is noticeably high between 10 and 15 MeV.

4.6.8 Experimental Uncertainties

The uncertainties in this experiment can be separated into uncertainties due to the iron normalization and those due to measuring the xenon cross section. For the most part, the iron normalization dominates the systematic error in the experiment. Uncertainties on the absolute flux and absolute efficiency are removed by this iron normalization.

The iron normalization data point, $\sigma_{\gamma,\mathrm{known}} = 1.5 \pm 0.1$ b at 6.2 MeV, adds a 6.7% error. Despite the correction being small, C_{known} has an uncertainty assigned to it of 0.037, for a relative uncertainty of 3.7%. This was determined using the difference between the HPGe and $\mathrm{LaBr_3}$ datasets at 6.2 MeV from [55]. Once again, using the maximum difference between the

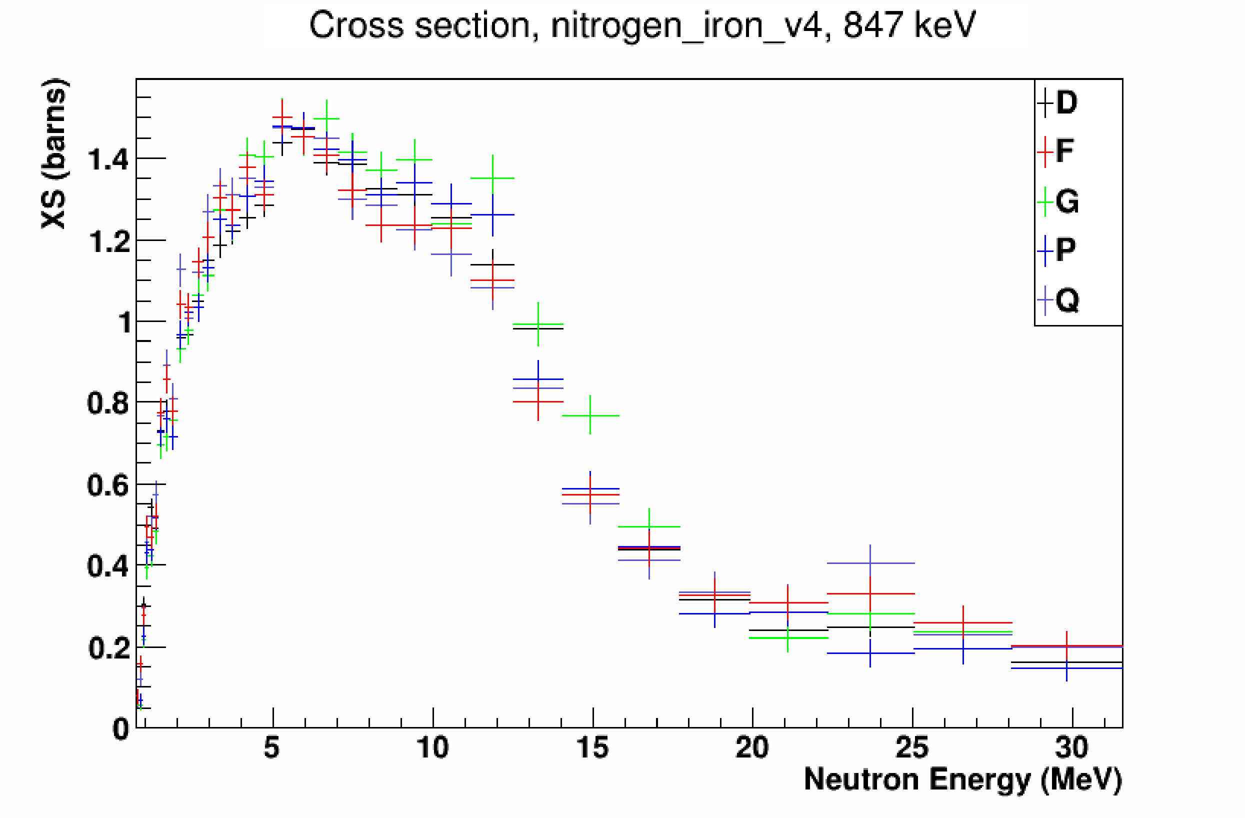

Figure 4.20: Comparison between the cross section results for the ^{56}Fe 847 keV transition for all detectors. The normalization point at 6.2 MeV neutron energy is clear, as all detectors are set to agree at that point. The uncertainties on this plot are due to statistical errors and the uncertainty from the Beyer normalization point. No systematic errors were considered here.

HPGe and $\mathrm{LaBr_3}$ datasets, a 7% uncertainty was assigned to the angular correction to each detector, $C_{\gamma,i}$. The uncertainty in the thickness of the iron is 2%. Finally, an uncertainty of 4% was assigned due to the correction for the difference between efficiencies related to xenon and iron.

Systematic uncertainties due to ^{136}Xe cross section measurements are smaller, but have been determined. The attenuation factor, A_i, has a max correction of about 3%, and an uncertainty of 3% has been assigned as well. Livetimes for the data acquisition system have negligible error. The efficiency uncertainty was determined by the error on the fit to to the efficiency curve, shown in Fig. 4.21. For most of the measured ^{136}Xe transitions, the uncertainty due to the efficiency is very small, up to about 2% at the 1313 keV line. However, the efficiency uncertainty grows to about 6% near the 2290 and 2415 keV transitions.

An uncertainty of 3% has been assigned to the areal density of ^{136}Xe in the target during the run. Uncertainties due to, β_i, the angular effect minimization factors, are split into two regions. The minimization can only be applied below 2 MeV neutron energy because detector D only measures up to that energy. Maximum angular corrections for the iron data are being used as an uncertainty for xenon angular effects. As a consequence of the angular minimization method, the uncertainty goes as the square of the correction. Due to this, a 3% uncertainty is being applied overall for the angular effect minimization method below 2 MeV. Above 2 MeV neutron energy, the angular effect minimization method is not used. Instead, the uncertainty due to a lack of angular correction is estimated by taking the maximum correction applied to the iron data. An error of 18% error is applied above 2 MeV. This could be significantly improved with a measurement of the angular distributions of the relevant transitions or a measurement at another unique detector angle.

The remaining uncertainties are statistical accounting for the number of counts in the Ge detectors and fission chambers. The fission uncertainty across the whole spectrum is approximately 2% per neutron energy bin. The statistical uncertainties due to counts in the Ge detectors vary significantly depending on the neutron energy bin and transition in

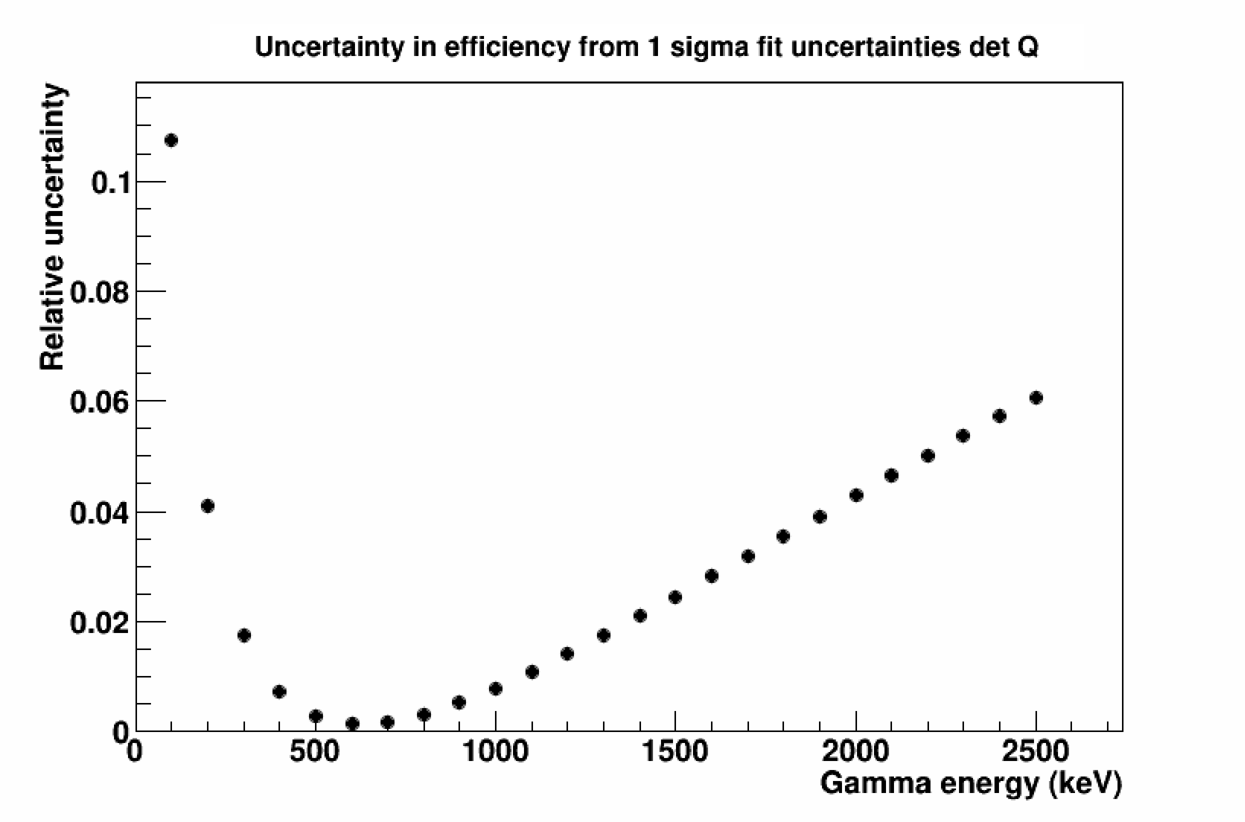

Figure 4.21: An efficiency uncertainty curve was determined using the errors on the fit parameters. The efficiency was evaluated at 1σ, and the difference divided by the original efficiency was plotted as the error shown here.

Systematic uncertainties due to iron normalization

$\sigma_{\gamma,\text{known}}$	6.7%
C_{known}	3.7%
$C_{\gamma,i}$	7%
t_{Fe}	2%
ϵ_{Fe}	4%

Table 4.1: Uncertainties due to the iron normalization are dominant on all lines below E_n = 2 MeV.

Systematic uncertainties due to ^{136}Xe measurement

A_i	3%
ϵ_{Xe}	0.5 to 6%
t_{Xe}	3%
β_i, $E_\gamma < 2$ MeV	3%
β_i, $E_\gamma > 2$ MeV	18%

Table 4.2: Uncertainties are small relative to iron normalization and statistical uncertainty, except $E_n > 2$ MeV.

question.

4.7 ^{136}Xe **Cross Section Analysis**

Ten transitions from neutron inelastic scattering on ^{136}Xe were measured. These transitions are listed in Table 4.3. Most of the transitions measured are due to the ^{136}Xe (n,nγ)^{136}Xe interaction. One transition is measured that is a ^{136}Xe (n,3nγ)^{134}Xe interactions, and this transition appears at a much higher neutron energy. One transition at 772 keV is due to ^{136}Xe (n,5nγ)^{132}Xe. These transitions also appears at a much higher neutron energy than the usual ^{136}Xe (n,nγ)^{136}Xe interactions.

The strongest transition in the data is from the first excited state in ^{136}Xe at 1313 keV. Two lines of interest, 2290 and 2415 keV, are close to the $0\nu\beta\beta$ region of interest for ^{136}Xe. Other lines, likely due to neutron interactions on ^{136}Xe, were seen in the data, but could not

Measured ^{136}Xe transitions

E_γ (keV)	Interaction	Transition
370	^{136}Xe (n,nγ)^{136}Xe	$6^+ \rightarrow 6^+$
381	^{136}Xe (n,nγ)^{136}Xe	$4^+ \rightarrow 2^+$
750	^{136}Xe (n,nγ)^{136}Xe	$5 \rightarrow 4^+$
771	^{136}Xe (n,nγ)^{136}Xe	$4^+ \rightarrow 4^+$
773	^{136}Xe (n,5nγ)^{132}Xe	$4^+ \rightarrow 2^+$
813	^{136}Xe (n,nγ)^{136}Xe	either 3^+ or $4^+ \rightarrow 2^+$
884	^{136}Xe (n,3nγ)^{134}Xe	$4^+ \rightarrow 2^+$
1313	^{136}Xe (n,nγ)^{136}Xe	$2^+ \rightarrow 0^+$
2290	^{136}Xe (n,nγ)^{136}Xe	$2^+ \rightarrow 0^+$
2415	^{136}Xe (n,nγ)^{136}Xe	$2^+ \rightarrow 0^+$

Table 4.3: Measured transitions from ^{136}Xe (n,nγ)^{136}Xe, ^{136}Xe (n,3nγ)^{134}Xe, and ^{136}Xe (n,5nγ)^{132}Xe.

be measured due to low statistics or interfering background lines.

4.7.1 ^{136}Xe neutron inelastic scattering metastable state

One difficulty in analyzing this data is that ^{136}Xe has a metastable 1891 keV level with a 2.95 μs half-life [56]. The half-life of this state spans the duration of a micropulse from the neutron beam. ^{136}Xe nuclei that are excited to this state will decay to the 1694 keV state and emit 197 keV γ-rays throughout the pulsing of the beam. From the 1694 keV state, the nucleus will promptly decay to 1313 keV and then to the ground state, emitting a 381 and 1313 keV γ-ray. The 197 keV γ-rays emitted by this metastable state lead to delayed emissions of 381 and 1313 keV γ's and do not have a neutron energy that can be accurately reconstructed. This effect is shown in Fig. 4.22.

The background due to the 197 keV line must be removed for an accurate measurement of the subsequent transitions. In order to remove the background, the shape of the 197 keV transition is taken, scaled up to the first few bins of either the 381 or 1313 keV cross section, and subtracted. A scaling factor must be applied for this subtraction because the efficiency of the 197 keV is different from the two lines from which it will be subtracted. The shape of

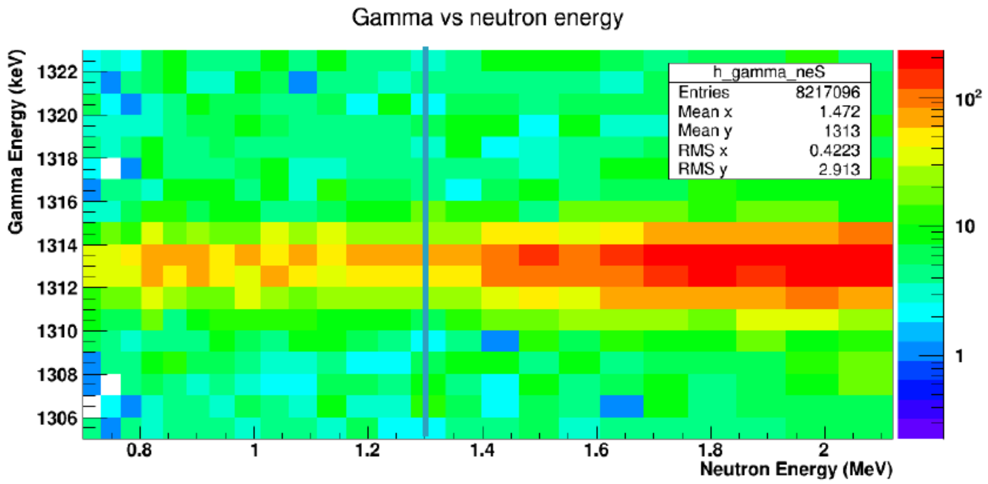

Figure 4.22: ^{136}Xe 1313 keV line. Despite being below the neutron inelastic scattering threshold of 1.3 MeV, there are many events in the spectrum. This is due to a metastable 1891 keV level with a 2.95 μs half-life. Gammas emitted after the nucleus has been in the metastable state will not have a proper time of flight reconstruction of neutron energy.

the 197 keV line matches up quite well with the background in the 381 and 1313 keV cross sections, shown in Fig. 4.23 and Fig. 4.24. In bins where a fit has failed due to the gamma yield method, the subtraction is not completed and the resultant bin is left empty. This is evident in Fig. 4.25 from 25 MeV to 32 MeV.

4.7.2 Partial γ-ray cross sections for ^{136}Xe

Partial γ-ray cross sections were measured for eight transitions via the ^{136}Xe (n,nγ)^{136}Xe interaction, two transitions via the ^{136}Xe (n,3nγ)^{134}Xe interaction, and two transitions via the ^{136}Xe (n,5nγ)^{132}Xe interaction. The two transitions that required the metastable background subtraction are shown in Fig. 4.25 and Fig. 4.26. All other measured cross sections are shown in figures 4.27 through 4.34.

The largest cross section measured with this data was for the 1313 keV line, with a maximum cross section of 2.1 b at 4 MeV neutron energy.

Despite being very close in γ-ray energy, the lines at 771 keV and 773 keV were resolvable

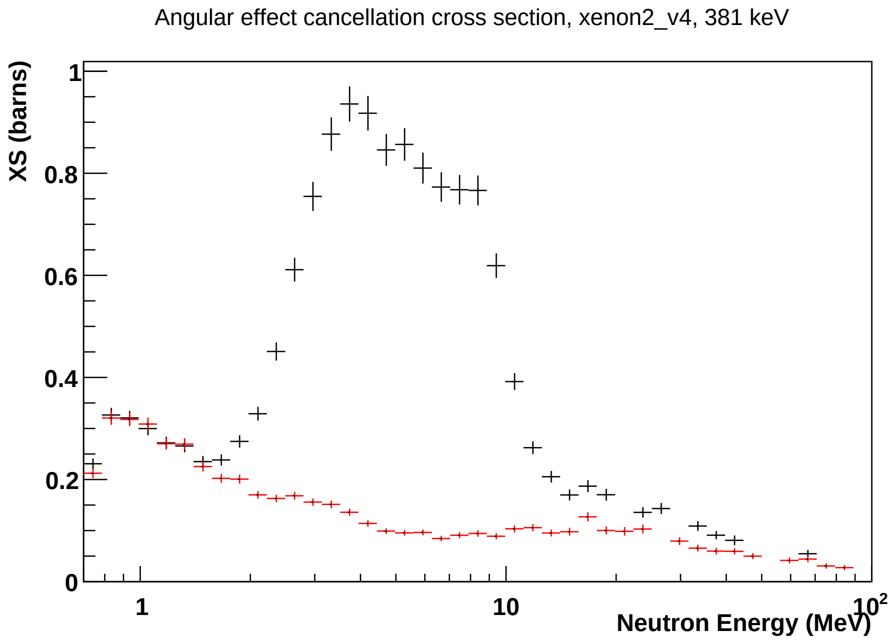

Figure 4.23: 381 keV line with scaled 197 keV line

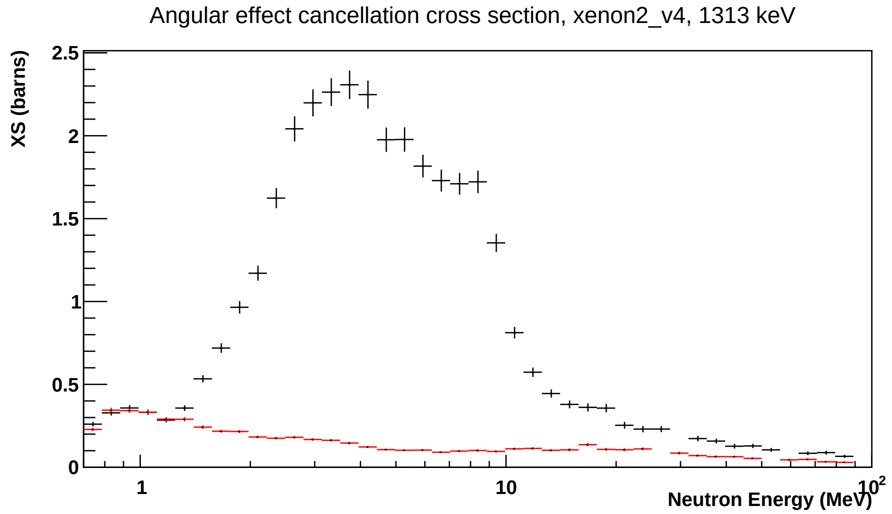

Figure 4.24: 1313 keV line with scaled 197 keV line

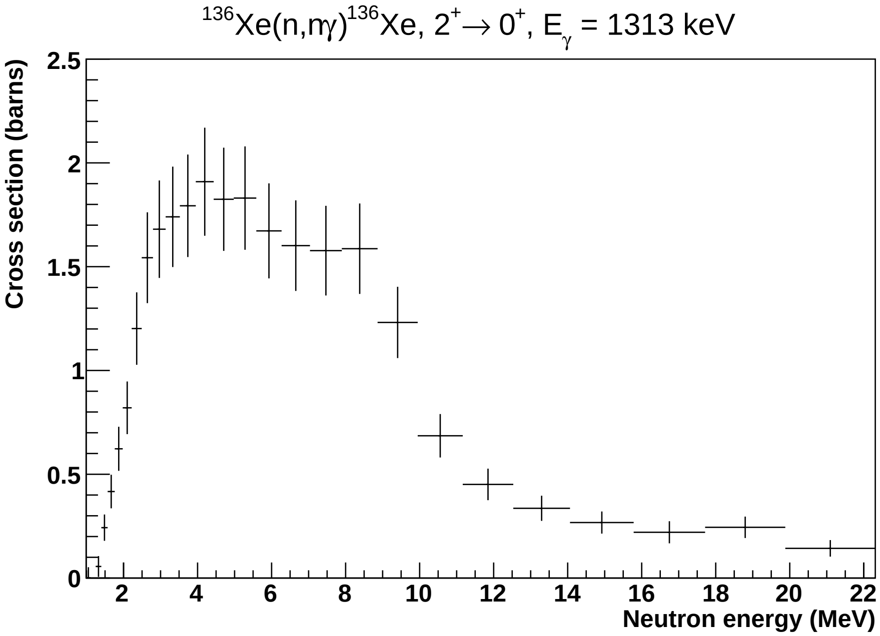

Figure 4.25: Partial γ-ray cross sections for ^{136}Xe (n,nγ)^{136}Xe 1313 keV transition.

by their separation in neutron energy. The 771 keV line tapers off by around 12 MeV, as shown in Fig. 4.29, whereas the 773 keV line becomes measureable above 30 MeV, as shown in Fig. 4.30.

4.8 ^{136}Xe $(n, xn\gamma)$ Cross Section Limits in the EXO-200 Region of Interest

In order to help quantify backgrounds for $0\nu\beta\beta$ experiments using ^{136}Xe as a source, limits on partial γ-ray cross sections have been calculated in the EXO-200 region of interest (ROI). These partial γ-ray cross section limits have been evaluated in three neutron energy bins, 1 - 5 MeV, 5 - 10 MeV, and 10 - 50 MeV. The γ energy range of the ROI was 2350 to 2550 keV.

There is a peak due to ^{136}Xe in the ROI at 2415 keV. For this cross section limit analysis, the 2415 keV peak was ignored, as the cross section of that line was directly measured. Around 2490 keV, there are hints of a peak, as seen in Fig. 4.35, but the source of the γ is unknown.

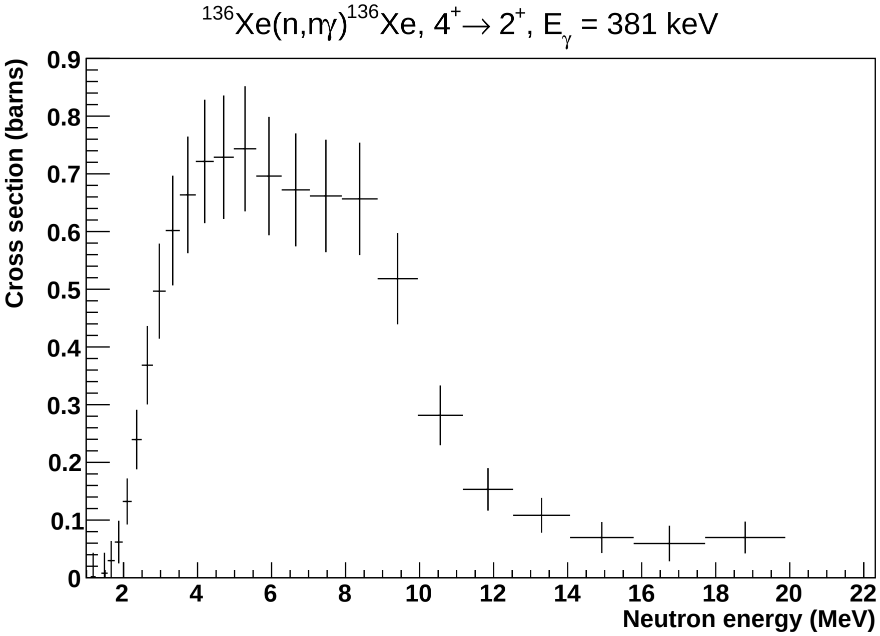

Figure 4.26: Partial γ-ray cross sections for ^{136}Xe (n,nγ)^{136}Xe 381 keV transition.

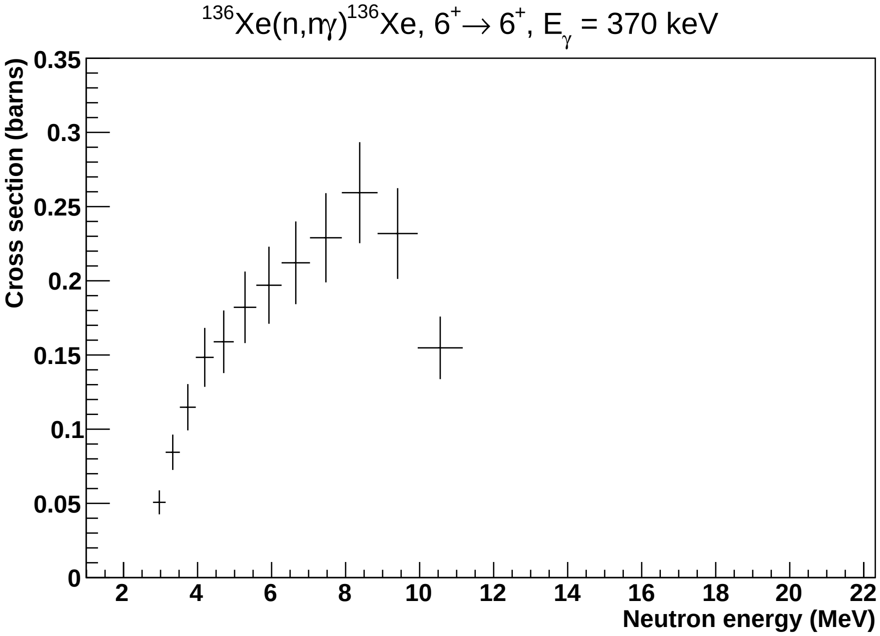

Figure 4.27: Partial γ-ray cross sections for ^{136}Xe (n,nγ)^{136}Xe 370 keV transition.

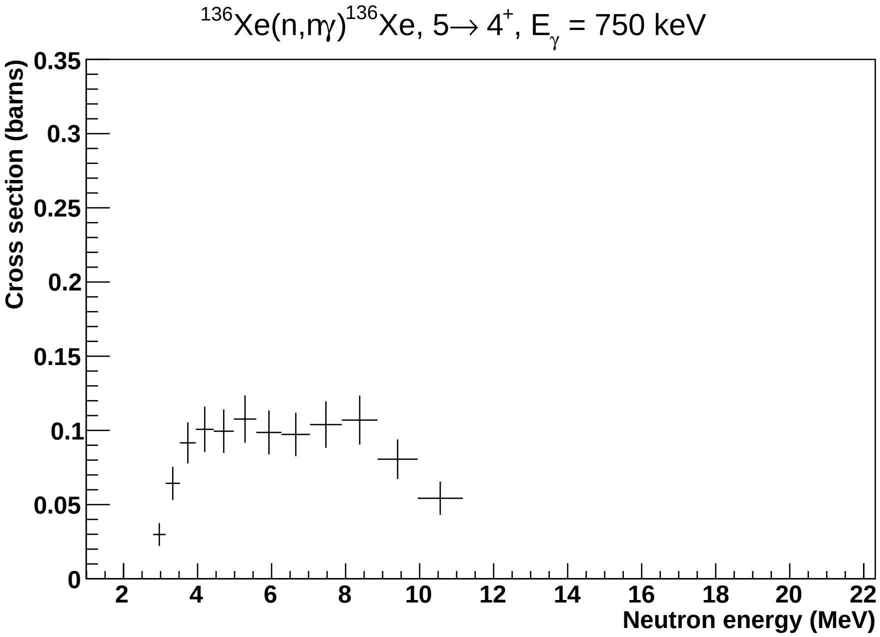

Figure 4.28: Partial γ-ray cross sections for ^{136}Xe (n,nγ)^{136}Xe 750 keV transition.

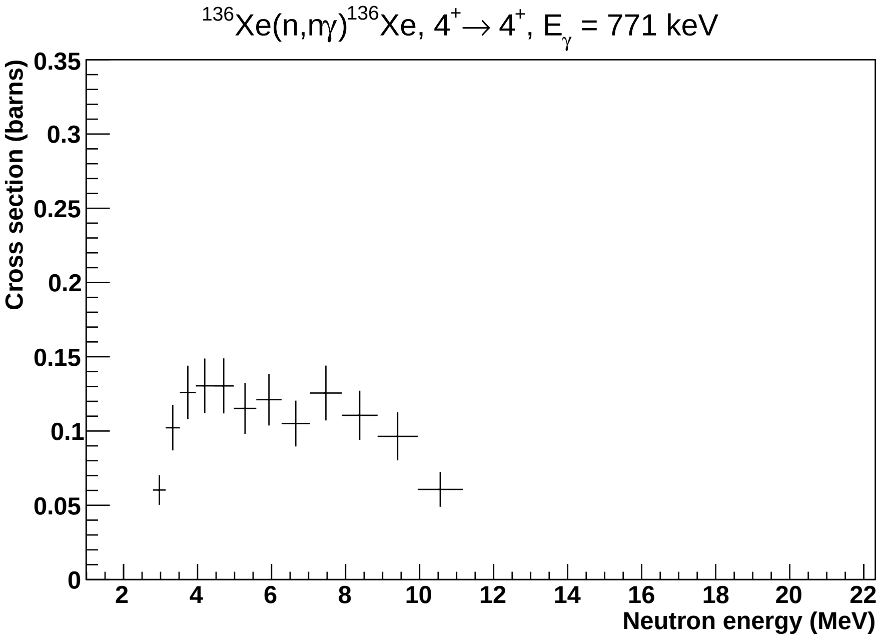

Figure 4.29: Partial γ-ray cross sections for ^{136}Xe (n,nγ)^{136}Xe 771 keV transition.

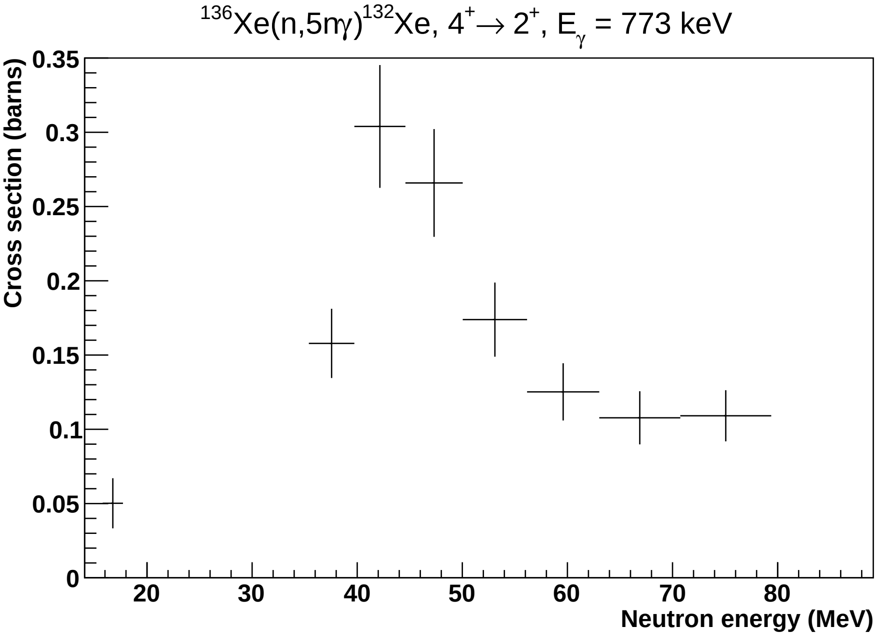

Figure 4.30: Partial γ-ray cross sections for ^{136}Xe (n,5nγ)^{132}Xe 773 keV transition.

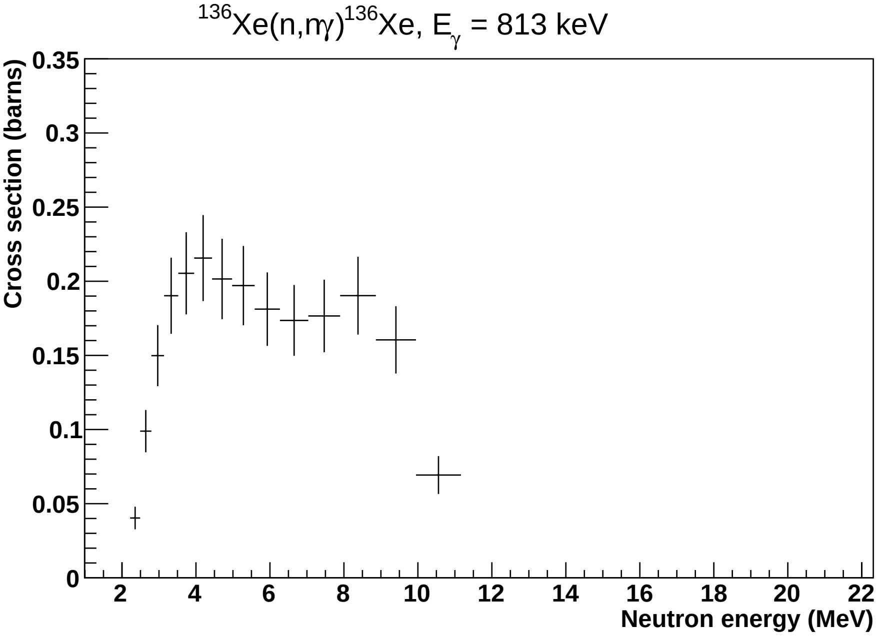

Figure 4.31: Partial γ-ray cross sections for ^{136}Xe (n,nγ)^{136}Xe 813 keV transition. The spin states for this transition are unknown.

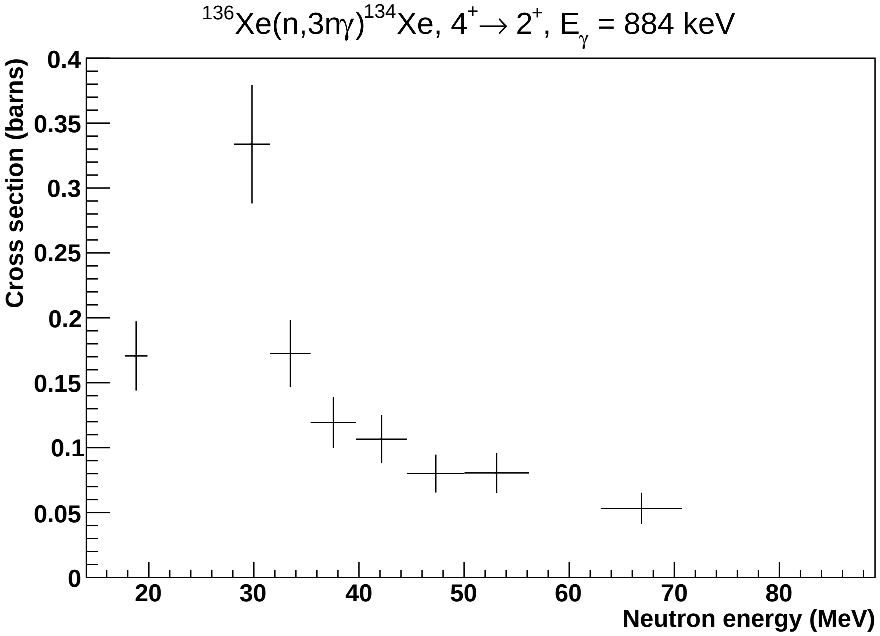

Figure 4.32: Partial γ-ray cross sections for ^{136}Xe (n,3nγ)^{134}Xe 884 keV transition.

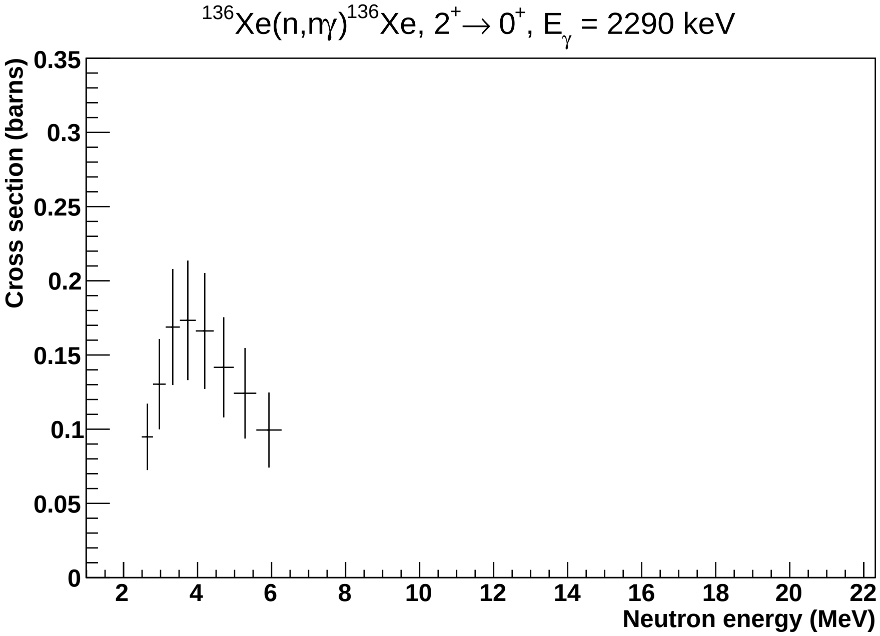

Figure 4.33: Partial γ-ray cross sections for ^{136}Xe (n,nγ)^{136}Xe 2290 keV transition.

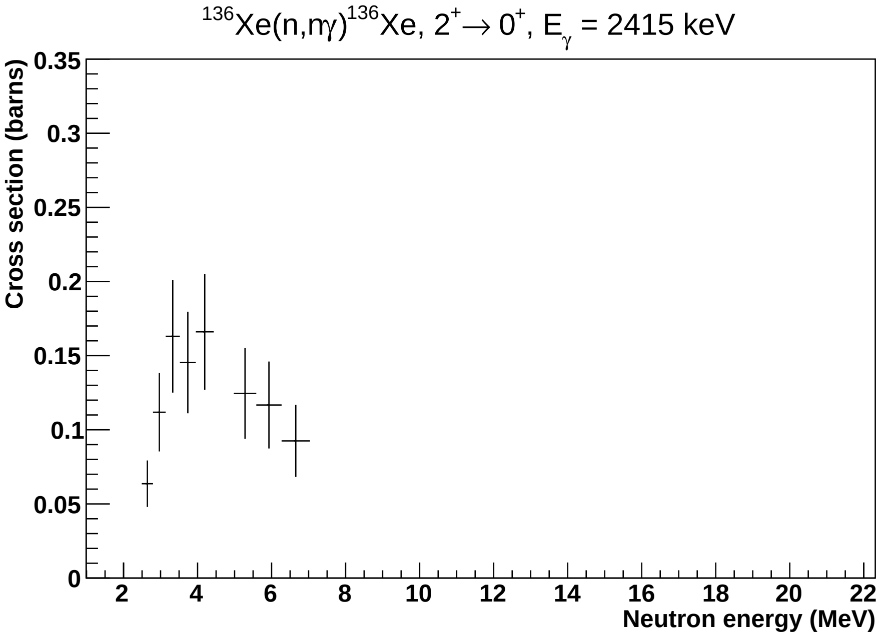

Figure 4.34: Partial γ-ray cross sections for ^{136}Xe (n,nγ)^{136}Xe 2415 keV transition.

A single detector, P, was used in this limit analysis. Detector P was chosen as the angular effects due to anisotropy are expected to be the smallest at that angle, according to results from the iron angular corrections.

The ROI was profiled over with a 9 keV γ energy window. A range larger than the resolution of the detector, 9 keV, was chosen in order to contain any γ line that could show up in this region. Counts within this 9 keV window were compared with a fit to the background and a 90% confidence level limit to the cross section was determined. Fig. 4.36 shows the result of one of these scans over the ROI. The 2415 keV and 2490 keV peaks are apparent in the scan. The largest bin, except for bins near the 2415 keV peak, was chosen as the most conservative estimate for the limit for that neutron energy window. Using upper limit counts from the profile, a cross section was determined with the usual factors as described before.

The upper 90% C.L. results of this cross section limit method is shown in Fig. 4.37. The limits determined were 1.6 mb in the 1 to 5 MeV window, 9.3 mb in the 5 to 10 MeV window, and 2.2 mb in the 10 to 100 MeV window

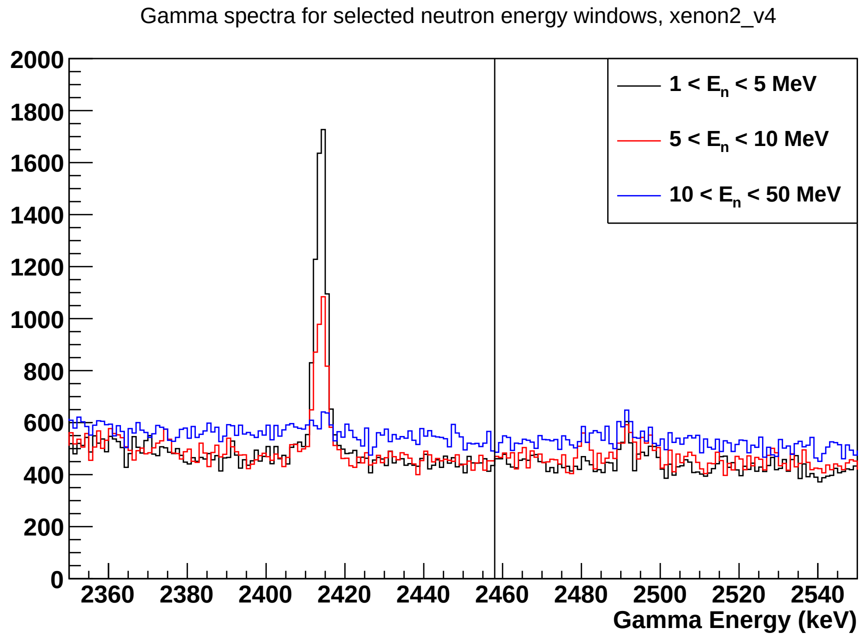

Figure 4.35: The EXO-200 ROI is 2350 to 2550 keV, around the ^{136}Xe $0\nu\beta\beta$ end point of 2458 keV. γ counts are shown from the GEANIE Ge detectors.

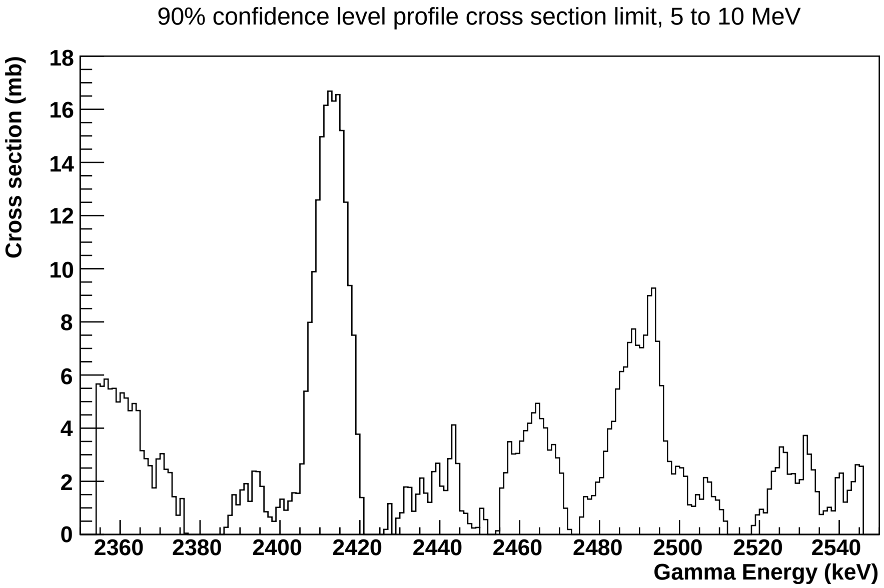

Figure 4.36: Limit scan across EXO-200 ROI

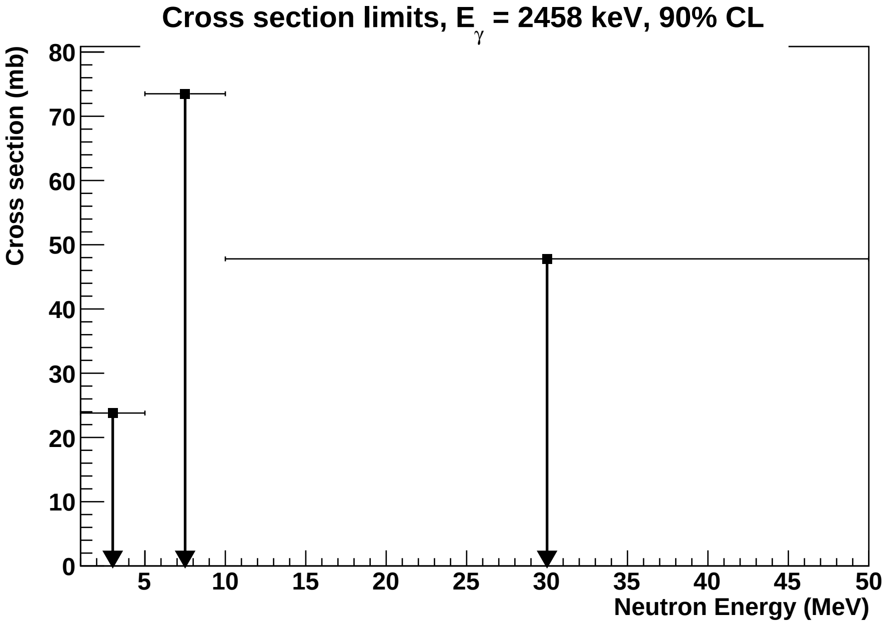

Figure 4.37: Cross section limit

Chapter 5

Impact and Conclusions

5.1 ^{137}Xe veto in EXO-200

^{137}Xe is produced in the xenon volume by cosmogenic production of fast neutrons capturing on ^{136}Xe. After the capture happens, prompt γ rays are emitted from the ^{137}Xe nucleus, and then it decays with a half-life of 3.8 minutes. The signature of this interaction can be used to remove the background from the detector due to ^{137}Xe decay.

In EXO-200, these events were identified and removed in order to reduce backgrounds from this interaction by vetoing potential ^{137}Xe decay events [57]. Neutron capture events on ^{136}Xe were identified by a coincidence between a signal in the muon veto system and summed event energy signal from the detector from the prompt capture γs. An example of a muon track through the experiment is shown in Fig. 5.1. After identifying a possible neutron capture event, a cut was placed on subsequent events which was optimized in order to minimize backgrounds due to ^{137}Xe β decay while maximizing exposure and livetime of the detector. The optimized time cut was chosen to veto events following ^{137}Xe signature for 19.1 minutes, five ^{137}Xe half-lives. Events were only vetoed in the half of the TPC that the signature was detected. This cut was estimated to reduce the number of ^{137}Xe events by 23 ± 8%, with a decreased exposure of 2.8% in Phase II.

The neutron capture on ^{136}Xe result from DANCE discussed in Chapter 3 provides updated capture cascades for improved simulation and veto efficiency in future versions of this analysis.

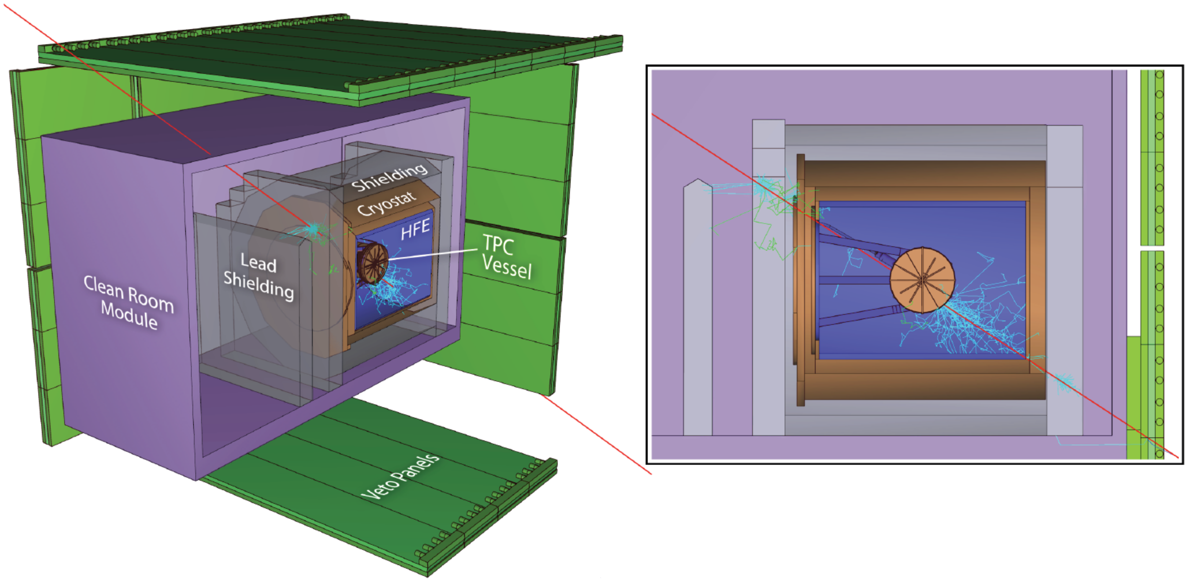

Figure 5.1: Muon track simulation in EXO-200. The muon veto panels are shown in green. The muon track (red) is shown, along with resultant photons (cyan) and neutrons (green). Figure from [21].

5.2 Future of $0\nu\beta\beta$

No current double beta decay experiment has found convincing evidence of $0\nu\beta\beta$. However, this does not mean that the $0\nu\beta\beta$ process does not exist. The $0\nu\beta\beta$ decay process is much rarer than the $2\nu\beta\beta$ Standard Model process. The sensitivity to the $0\nu\beta\beta$ half-life must be improved in order to further set limits on this process, shown in Fig. 5.2, or possibly discover some beyond the standard model physics.

In order to do this, the next generation xenon experiment, nEXO [58], is moving toward a 5 ton monolithic detector. These larger detectors offer many advantages for $0\nu\beta\beta$ searches.

First of all, these detectors can hold a larger mass of decay isotope. The sensitivity of the experiment is proportional to the square root of the total mass of the decay isotope [14]:

$$S^{0\nu}_{1/2} \propto \epsilon \frac{a}{A} \sqrt{\frac{MT}{B\Gamma}} \tag{5.1}$$

where ϵ is the efficiency of detection of the decay, a is the isotopic abundance, A is the isotopic mass, M is the source mass, T is the experimental run time, B is the background, and Γ is the detector energy resolution.

A larger, monolithic detector also has the advantage of more self-shielding. In EXO-200, the xenon near the edges of the detector acts both as an active shield, reducing background from γs originating outside the detector and from the walls of the detector, as well as an extra volume to measure backgrounds from outside the detector. The nEXO detector will be many times the size of EXO-200 and therefore will have many fewer external γs making it to the center of the detector.

Efforts are also underway to improve background identification and reduction. The neutron capture and neutron inelastic scattering measurements on ^{136}Xe discussed in Chapter 4 are examples of that effort. Due to the low rate of neutrons at the proposed nEXO site, SNOLAB, the background due to inelastic scattering is expected to be small. Also, the large water shield will thermalize most of the neutrons before making it to the detector.

The expected sensitivity of nEXO has been determined [58], and it was predicted that nEXO will reach a 3σ discovery potential for the ^{136}Xe $0\nu\beta\beta$ half-life of 5.7×10^{27} years. The 90% CL exclusion sensitivity is expected to reach 9.2×10^{27} years, with the potential to reach well beyond 10^{28} years. Limits on the ^{136}Xe $0\nu\beta\beta$ half-life can be converted into an effective Majorana neutrino mass, shown in Fig. 5.2.

5.3 Neutron Calibration of Detectors

One difficulty that arises with the ever-increasing size of detectors designed to measure $0\nu\beta\beta$ is accurate calibration of the detector. While large detectors offer more self-shielding, that same shielding reduces the penetration of γs that could be used to calibrate the detector.

A light map must be created for the entire detector which characterizes the light response of the photo detectors to particle interactions with a position and energy map. This light map is measured with γs from a calibration source. In EXO-200, this light map was determined

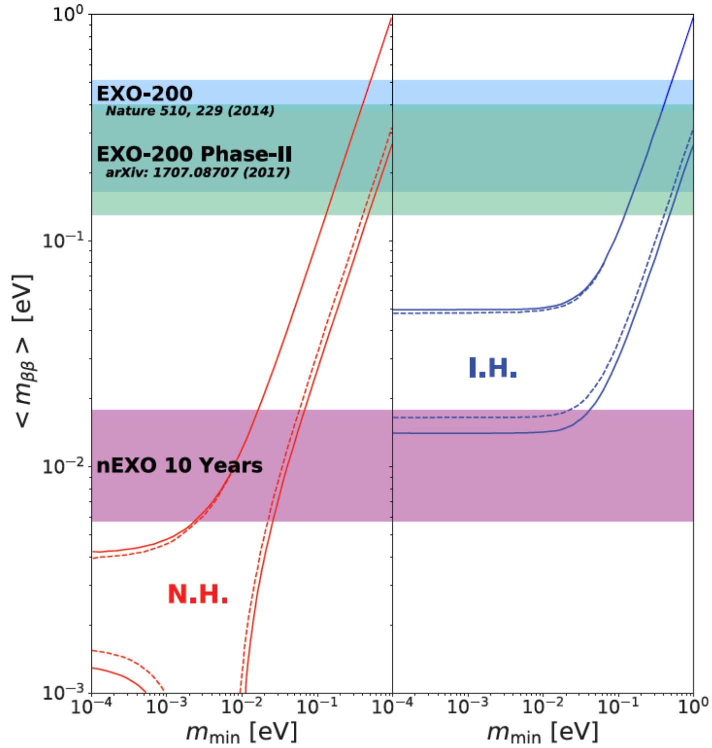

Figure 5.2: Projected majorana neutrino mass sensitivities for the normal (left) and inverted (right) hierarchies with nEXO. The width of the horizontal bands stems from uncertainty in the nuclear matrix elements. The dashed lines result from uknown Majorana phases.

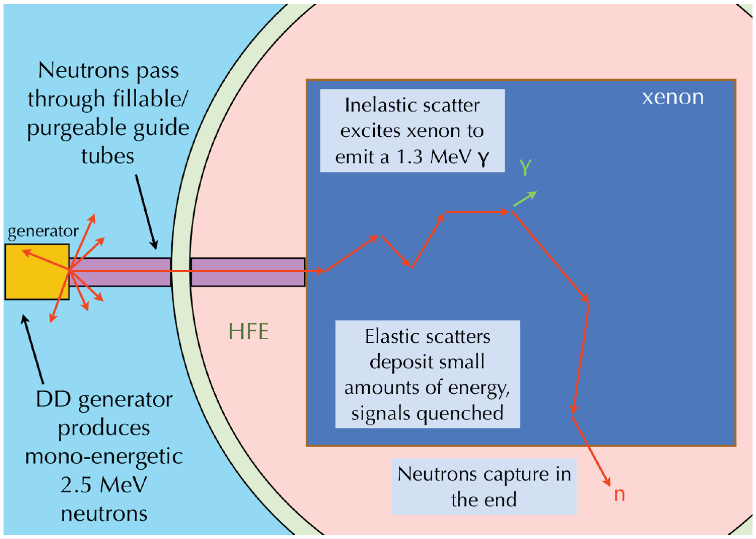

Figure 5.3: Neutron calibration idea for nEXO. Neutrons produced at the DD generator on the left pass through a tube toward the main nEXO TPC.

using 2615 keV γs from an external ^{232}Th source. The scattering length of a 2.5 MeV γ in xenon is 8.5 cm, or 7.6 scattering lengths to the center of the current design for nEXO. This means that external γs from a radioactive source will not have a uniform distribution in nEXO. Using a more penetrating source of gammas or a source that is disperesed in the xenon itself would produce a more uniform distribution of calibration γs.

An idea for the calibration of nEXO is using neutron inelastic scattering gammas produced via neutron source outside detector. Fig. 5.3 shows a schematic of this calibration idea. The scattering length of a 2.5 MeV neutron in xenon is 13.0 cm, or 5.0 scattering lengths to the center of nEXO. This design would use a DD generator to produce mono-energetic, 2.5 MeV neutrons that would excite ^{136}Xe to the first excited state at 1313 keV through neutron inelastic scattering. The 1313 keV γs produced could then be used to produce a light map for nEXO. Fig. 5.4 shows a simulation of interaction points within nEXO. In this case, the source is placed outside of the detector, causing the region of high counts nearest to the source on the edge of the detector.

Alternatively, a more traditional use of radionuclide γ production can be used to produce the light map. This could either be a very high flux of γs from a radioactive source placed

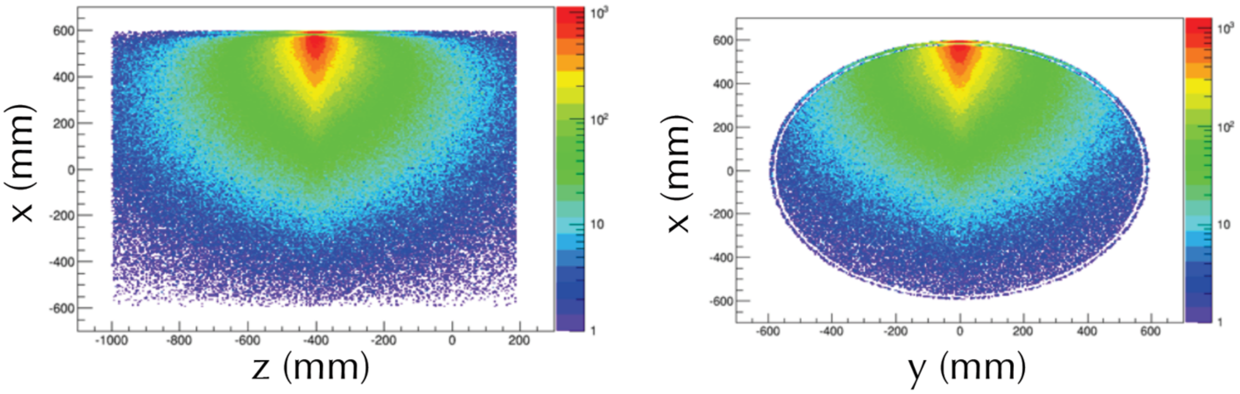

Figure 5.4: Simulated distribution of 1.3 MeV γs from neutron calibration in nEXO

outside of the detector, or a source of γs from a dissolvable radionuclide within the xenon itself. The former would be the same method as EXO-200 used, while the latter has been implemented in XENON100 with dissolved ^{220}Ra [59].

5.4 Conclusions

Future measurements of $0\nu\beta\beta$ will rely on background reduction and identification techniques.

One of these backgrounds, neutron capture on ^{136}Xe and subsequent decay of the ^{137}Xe nucleus, has been measured at DANCE and reported here. This measurement provides an update to the thermal neutron capture cross section and also provides neutron capture cascades which can be used in future simulations.

Neutron inelastic scattering on ^{136}Xe was measured at GEANIE and reported here. It is expected that neutron inelastic scattering will not cause a significant background for nEXO due to the depth of the proposed location at SNOLAB, but a calibration method has been proposed which relies on neutron inelastic scattering in ^{136}Xe.

The future of $0\nu\beta\beta$ searches is bright. Measurement of beyond the Standard Model physics is within our reach.

Bibliography

[1] C. Patrignani and P. D. Group, Chinese Physics C **40**, 100001 (2016).

[2] N. Ackerman *et al.* (EXO Collaboration), Phys. Rev. Lett. **107**, 212501 (2011).

[3] A. Gando *et al.* (KamLAND-Zen Collaboration), Phys. Rev. Lett. **117**, 082503 (2016).

[4] T. G. Collaboration, Nature **544**, 47 (2017).

[5] T. M. Collaboration, Advances in High Energy Physics **2014** (2014), 10.1155/2014/365432.

[6] C. Alduino *et al.*, The European Physical Journal C **77**, 13 (2017).

[7] Proceedings of the Royal Society of London A: Mathematical, Physical and Engineering Sciences **175**, 71 (1940), http://rspa.royalsocietypublishing.org/content/175/960/71.full.pdf .

[8] C. L. Cowan, Jr., F. Reines, F. B. Harrison, H. W. Kruse, and A. D. McGuire, Science **124**, 103 (1956).

[9] E. Majorana, Il Nuovo Cimento (1924-1942) **14**, 171 (2008).

[10] S. F. King and C. Luhn, Reports on Progress in Physics **76**, 056201 (2013).

[11] F. T. Avignone, S. R. Elliott, and J. Engel, Rev. Mod. Phys. **80**, 481 (2008).

[12] J. B. Albert *et al.* (EXO-200), Nature **510**, 229 (2014).

[13] T. G. Collaboration, Nature **544** (2017), 10.1038/nature21717.

[14] S. R. Elliott and P. Vogel, Annual Review of Nuclear and Particle Science **52**, 115 (2002), https://doi.org/10.1146/annurev.nucl.52.050102.090641 .

[15] D. Leonard *et al.*, Nuclear Instruments and Methods in Physics Research Section A: Accelerators, Spectrometers, Detectors and Associated Equipment **591**, 490 (2008).

[16] S. Wong, *Introductory Nuclear Physics*, 2nd ed. (John Wiley and Sons Inc., 1998).

[17] M. Redshaw, E. Wingfield, J. McDaniel, and E. G. Myers, Phys. Rev. Lett. **98**, 053003 (2007).

[18] R. Neilson *et al.*, *Proceedings, 1st Symposium on Prospects in the Physics of Discrete Symmetries (DISCRETE 2008): Valencia, Spain, December 11-16, 2008*, Nucl. Instrum. Meth. **A608**, 68 (2009), arXiv:0906.2499 [physics.ins-det] .

[19] J. B. Albert *et al.* (EXO-200 Collaboration), Phys. Rev. C **95**, 025502 (2017).

[20] M. Auger *et al.* (EXO), Phys. Rev. Lett. **109**, 032505 (2012).

[21] J. B. Albert *et al.* (EXO-200), JCAP **1604**, 029 (2016).

[22] G. C. Carlson, W. C. Schick Jr., W. L. Talbert Jr., and F. K. Wohn, Nuclear Physics A **125**, 267 (1969).

[23] J. B. Albert, S. J. Daugherty, T. N. Johnson, T. O'Conner, L. Kaufman, A. Couture, J. L. Ullmann, and M. Krtika, Phys. Rev. **C94**, 034617 (2016), arXiv:1605.05794 [nucl-ex] .

[24] J. L. Ullmann *et al.*, Phys. Rev. C **89**, 034603 (2014).

[25] R. Reifarth *et al.*, Nucl. Inst. Methods Phys. Res., Sect. A **531**, 530 (2004).

[26] G. M. Hale and P. G. Young, "ENDF/B-VI MAT 325," (1991).

[27] J. Allison *et al.*, IEEE Trans. Nucl. Sci. **53**, 270 (2006).

[28] S. Agostinelli *et al.* (GEANT4), Nucl. Inst. Methods Phys. Res., Sect. A **506**, 250 (2003).

[29] M. Jandel *et al.*, Nucl. Inst. Methods Phys. Res., Sect. B **261**, 1117 (2007).

[30] F. Bečvář, Nucl. Inst. Methods Phys. Res., Sect. A **417**, 434 (1998).

[31] G. Rusev, M. Jandel, M. Krtička, C. W. Arnold, T. A. Bredeweg, A. Couture, W. A. Moody, S. M. Mosby, and J. L. Ullmann, Phys. Rev. C **88**, 057602 (2013).

[32] E. Browne and J. K. Tuli, Nuclear Data Sheets **108**, 2173 (2007), Data extracted from the ENSDF database, version February 12, 2015, `http://www.nndc.bnl.gov/`.

[33] S. G. Prussin, R. G. Lanier, G. L. Struble, L. G. Mann, and S. M. Schoenung, Phys. Rev. C **16**, 1001 (1977).

[34] S. F. Mughabghab, *Atlas of Neutron Resonances: Resonance Parameters and Thermal Cross Sections. Z=1-100* (Elsevier Science, 2006).

[35] Q. B. Shen and S. F. Mughabghab, "ENDF/B-VII.1 MAT 5461," (2006).

[36] R. L. Macklin, *Search for* ^{136}Xe *Resonance Neutron Capture*, Tech. Rep. ORNL/TM-10766 (1988) EXFOR database: http://www-nds.iaea.org/EXFOR/13159.002.

[37] M. Bresesti, F. Cappellani, A. M. Del Turco, H. Neumann, and E. Orvini, J. Inorg. Nucl. Chem. **27**, 1175 (1965).

[38] E. Kondaiah, N. Ranakumar, and R. W. Fink, Nuclear Physics A **120**, 329 (1968).

[39] B. Pritychenko and S. F. Mughabghab, Nucl. Data Sheets **113**, 3120 (2012).

[40] K. Shibata *et al.*, Journal of Nuclear Science and Technology **48**, 1 (2011).

[41] J. Macnamara and H. G. Thode, Phys. Rev. **80**, 296 (1950).

[42] T. Eastwood and F. Brown, Prog. Rep.: Canadian report to EANDC **16**, 6 (1963), EXFOR database: `http://www-nds.iaea.org/EXFOR/11849.014`.

[43] A. Koning and D. Rochman, Nuclear Data Sheets **113**, 2841 (2012).

[44] A. Koning *et al.*, "TENDL-2014: TALYS-based evaluated nuclear data library," `http://www.talys.eu/tendl-2014.html`.

[45] OECD/NEA Data Bank, "The JEFF-3.2 Nuclear Data Library," `http://www.oecd-nea.org/dbforms/data/eva/evatapes/jeff_32/` (2014).

[46] K. Way and G. Haines, *Tables of Neutron Cross Sections* (1947) AECD 2274.

[47] N. Fotiades, G. D. Johns, R. O. Nelson, M. B. Chadwick, M. Devlin, M. S. Wilburn, P. G. Young, J. A. Becker, D. E. Archer, L. A. Bernstein, P. E. Garrett, C. A. McGrath, D. P. McNabb, and W. Younes, Phys. Rev. C **69**, 024601 (2004).

[48] J. A. Becker and R. O. Nelson, Nuclear Physics News **7**, 11 (1997), https://doi.org/10.1080/10506899709410550 .

[49] S. MacMullin, *Elastic and Inelastic Scattering of Neutrons from Neon and Argon: Impact on Neutrinoless Double-Beta Decay and Dark Matter Experimental Programs*, Ph.D. thesis, University of North Carolina at Chapel Hill (2013).

[50] S. A. Wender, S. Balestrini, A. Brown, R. C. Haight, C. M. Laymon, T. M. Lee, P. W. Lisowski, W. McCorkle, R. O. Nelson, W. Parker, and N. W. Hill, Nuclear Instruments and Methods in Physics Research A **336**, 226 (1993).

[51] "A general monte carlo n-particle (mcnp) transport code," .

[52] D. Radford, "Notes on the use of the program gf3," (2000).

[53] H. Morinaga and T. Yamazaki, *In-Beam Gamma-Ray Spectroscopy* (North-Holland Publishing Company, 1976).

[54] R. Beyer, R. Schwengner, R. Hannaske, A. Junghans, R. Massarczyk, M. Anders, D. Bemmerer, A. Ferrari, A. Hartmann, T. Kgler, M. Rder, K. Schmidt, and A. Wagner, Nuclear Physics A **927**, 41 (2014).

[55] Dietz, Mirco, Bemmerer, Daniel, Beyer, Roland, Gohl, Stefan, Junghans, Arnd R., Kgler, Toni, Massarczyk, Ralph, Mller, Stefan E., Schwengner, Ronald, Szcs, Tams, Takacs, Marcell P., Wagner, Andreas, and Wagner, Louis, EPJ Web Conf. **146**, 11040 (2017).

[56] A. Sonzogni, Nuclear Data Sheets **95**, 837 (2002).

[57] J. B. Albert *et al.* (EXO-200 Collaboration), Phys. Rev. Lett. **120**, 072701 (2018).

[58] J. B. Albert *et al.* (nEXO), (2017), arXiv:1710.05075 [nucl-ex] .

[59] E. Aprile *et al.* (XENON Collaboration), Phys. Rev. D **95**, 072008 (2017)

SEAN J. DAUGHERTY

seanjdaugherty@gmail.com

EDUCATION

Indiana University Bloomington 2011 - 2018

Physics M.S. & Ph.D.

Thesis topic: *Neutron interactions on* ^{136}*Xe and their impact on neutrinoless double beta decay*

University of Illinois at Urbana-Champaign 2007 - 2011

Bachelor of Science in Engineering Physics with honors

Minors in Computer Science and Mathematics

RESEARCH EXPERIENCE

Indiana University 2012 - 2018

Graduate Research Assistant *Research advisor: Lisa Kaufman*

- Enriched Xenon Observatory (EXO-200 Experiment)
  - Ran experimental shifts for the EXO-200 experiment at the Waste Isolation Pilot Plant to help maintain the experimental running
  - Measured the electron lifetime weekly and performed ionization energy calibration to correct for the electron lifetime in EXO-200
  - Developed and implemented electron lifetime analysis using Monte-Carlo-based ionization spectrum fitting
  - Performed data quality analysis weekly to determine low background data inclusion

- Neutron capture measurements on ^{136}Xe at the Detector for Advanced Neutron Capture Experiments (DANCE)
  - Designed and built a gas target testing system
  - Ran experiment on site at the Lujan Center at the Los Alamos Neutron Science Center for neutron beam data collection and initial analysis
  - Developed analysis for neutron capture cross section measurements
  - Modeled and simulated neutron capture cascades with Geant4 and DICEBOX
  - Validated and improved simulation results using radioactive source measurements

  - Measured the neutron capture cross section for the first resonance of ^{136}Xe for the first time
  - Calculated a new thermal capture cross section for ^{136}Xe

- Neutron inelastic scattering measurements on ^{136}Xe at GErmanium Array for Neutron Induced Excitations (GEANIE)
  - Ran experiment on site at the Lujan Center at the Los Alamos Neutron Science Center for neutron beam data collection and initial analysis
  - Developed and performed analysis for GEANIE neutron inelastic scattering data, including time-of-flight analysis, neutron flux measurement, gamma-ray event energy calibration, germanium detector efficiency calculation, and neutron inelastic cross-section calculation
  - Measured neutron inelastic scattering cross sections for individual gamma lines in ^{136}Xe

University of Illinois 2010 - 2011
Undergraduate Research Assistant *Research advisor: Alexey Bezryadin*

- Fabricated graphene and few-layer graphite nano-devices

University of Illinois 2009 - 2010
Undergraduate Research Assistant *Research advisor: Naomi Makins*

- Developed experimental software for SeaQuest/E906 Fermi Lab experiment

SELECTED PUBLICATIONS

Joshua B. Albert, Sean J. Daugherty, Tessa N. Johnson, Thomasina O'Conner, Lisa J. Kaufman, Aaron Couture, John L. Ullmann, and Milan Krtika. Measurement of neutron capture on ^{136}Xe. *Phys. Rev. C*, 94(3):034617, 2016.

EXO-200 Collaboration. Improved measurement of the $2\nu\beta\beta$ half-life of ^{136}Xe with the EXO-200 detector. *Phys. Rev. C*, 89:015502, 2014.

EXO-200 Collaboration. Search for Majorana neutrinos with the first two years of EXO-200 data. *Nature*, 510(7504):229–234, 2014.

EXO-200 Collaboration. Cosmogenic Backgrounds to $0\nu\beta\beta$ in EXO-200. *JCAP*, 1604(04):029, 2016.

TALKS & CONFERENCE PRESENTATIONS

Neutron Interactions on ^{136}Xe and Their Impact on Neutrinoless Double Beta Decay Searches, Invited talk, LANSCE Nuclear Data Seminar Series, November 2, 2017, Lujan Center, Los Alamos, New Mexico.

Measurement of neutron capture on ^{136}Xe., Poster presentation, The XXVII International Conference on Neutrino Physics and Astrophysics (Neutrino 2016), July 4 - 9, 2016, London, England. Abstract P4.077.

Neutron Capture Cross Section of ^{136}Xe, Contributed talk, APS April Meeting 2015, April 11 - 14, 2015, Baltimore, Maryland. Abstract R4.00009.

TECHNICAL SKILLS

Computer Languages	Python, ROOT, C, C++
Tools	Latex, LabVIEW
Databases	MySQL

TEACHING EXPERIENCES

P201 General Physics I., Indiana University, **Laboratory Section Instructor**, *Fall 2011, Spring 2012*

P309 Intermediate (Modern) Physics Laboratory, Indiana University, **Laboratory Section Instructor**, *Fall 2013*

MEMBERSHIP, SERVICE, AND OUTREACH

Member, American Physical Society (2010 - present)

Physics Van at University of Illinois Member, (2009 - 2011)

Yearly Engineering Open House Presenter at University of Illinois, (2008 - 2011)

Physics Society Engineering Open House Organizer at University of Illinois, (2011)

Yearly IU Science Fest Presenter at Indiana University, (2011 - 2014)

AWARDS

DNP Travel Award (2015)

ALL OTHER REFEREED PUBLICATIONS

J. B. Albert et al. Search for Majoron-emitting modes of double-beta decay of ^{136}Xe with EXO-200. *Phys. Rev.*, D90(9):092004, 2014.

K. Twelker et al. An apparatus to manipulate and identify individual Ba ions from bulk liquid Xe. *Rev. Sci. Instrum.*, 85:095114, 2014.

B. Mong et al. Spectroscopy of Ba and Ba^{+} deposits in solid xenon for barium tagging in nEXO. *Phys. Rev.*, A91(2):022505, 2015.

T. Brunner et al. An RF-only ion-funnel for extraction from high-pressure gases. *Int. J. Mass Spectrometry*, 379:110, 2015.

J. B. Albert et al. Measurements of the ion fraction and mobility of α- and β-decay products in liquid xenon using the EXO-200 detector. *Phys. Rev.*, C92(4):045504, 2015.

J. B. Albert et al. Investigation of radioactivity-induced backgrounds in exo-200. *Phys. Rev. C*, 92:015503, Jul 2015.

J. B. Albert et al. Search for $2\nu\beta\beta$ decay of ^{136}Xe to the 0_1^+ excited state of ^{136}Ba with EXO-200. *Phys. Rev.*, C93(3):035501, 2016.

J. B. Albert et al. First Search for Lorentz and CPT Violation in Double Beta Decay with EXO-200. *Phys. Rev.*, D93(7):072001, 2016.

C. G. Davis et al. An Optimal Energy Estimator to Reduce Correlated Noise for the EXO-200 Light Readout. *JINST*, 11(07):P07015, 2016.

J. B. Albert et al. Measurement of the Drift Velocity and Transverse Diffusion of Electrons in Liquid Xenon with the EXO-200 Detector. *Phys. Rev.*, C95(2):025502, 2017.

D. S. Leonard et al. Trace radioactive impurities in final construction materials for EXO-200. *Nucl. Instrum. Meth.*, A871:169–179, 2017.

J. B. Albert et al. Searches for double beta decay of ^{134}Xe with EXO-200. *Phys. Rev.*, D96(9):092001, 2017.

J. B. Albert et al. Search for Neutrinoless Double-Beta Decay with the Upgraded EXO-200 Detector. *Phys. Rev. Lett.*, 120(7):072701, 2018.

J. B. Albert et al. Search for nucleon decays with EXO-200. *Phys. Rev.*, D97(7):072007, 2018.

M. Jewell et al. Characterization of an Ionization Readout Tile for nEXO. *JINST*, 13(01):P01006, 2018.